Ultrafast dynamics and optical measurements of coherent optical phonons in epitaxial cubic $Ge_2Sb_2Te_5$ thin films grown on InAs(111) wafer

Submitted by Reem Alsaigh, to the University of Exeter as a thesis of the degree of Doctor of Philosophy in Physics, December 2015.

I certify that all material in this thesis which is not my own work has been identified and that no material has previously been submitted and approved for the award of a degree by this or any other University.

.....

Abstract

This dissertation is concerned with the excitation of coherent optical phonons by femtosecond laser pulses. Investigation of coherent optical phonons can provide valuable understanding of the structure and phase transitions of a material. Studies have been performed upon two epilayers of cubic crystalline $Ge_2Sb_2Te_5$(GST) grown on InAs(111), and also on the reference InAs(111) sample. Time resolved pump-probe measurements of transient reflectivity and ellipticity response have been performed to excite and observe coherent optical phonons. The phonon dynamics is induced by an intense optical pump pulse and detected by a weak probe pulse with duration as short as 45fs.

Measurements of coherent optical phonons in GST/InAs (111) and InAs (111) samples have been performed as the pump polarisation, the sample orientation and pump fluence are varied. The transient reflectivity and ellipticity signals reveal coherent optical phonons with frequencies of 6.5 THz and $\sim$3.4 THz in InAs(111) and the two epitaxial GST/InAs(111) samples respectively. Microscopic and macroscopic theories are presented, that consider the Raman tensor and phonon representation, and predict that both zinc blend and rock-salt structures possess a three dimensional T_2 optical phonon mode at the zone centre. This T_2 mode is Raman active in the zinc blend structure, while it is Raman inactive in rock-salt structure. A theory of transient stimulated Raman scattering (TSRS) is presented to explain how the amplitude of the coherent optical phonon depends upon the pump and probe polarisation when excitation occurs by a combination of impulsive stimulated Raman scattering (ISRS) and excitation of a surface space charge (SSC) distribution. Comparison of experiment with theory suggests that the 6.5 THz optical phonon observed in the ellipticity signal for InAs(111) has three dimensional T_2 character. A coherent optical phonon is observed between 2.9 and 3.4 THz in the ellipticity signal for both GST/InAs(111) samples, and in the reflectivity signal of one of the GST/InAs(111) samples, and is inferred to also possess three dimensional character. Cubic GST is believed to adopt a rock-salt like structure with approximately 20% vacancies of the Ge and Sb sites. The ordering of vacancies within GST, the displacement of ions from their positions in the rock salt structure, and a resulting lack of inversion symmetry results in the $\sim$3.4 THz coherent optical phonon

being Raman active with the underlying three dimensional T_2 –like character. Indeed the observation of the T_2 -like phonon mode confirms that the underlying crystallographic structure of GST is essentially cubic.

The TSRS theory predicts that, for a (111) surface of a cubic crystal, the amplitude of the oscillation generated by the phonon within the ellipticity signal should have a $\sin(2(\theta-\phi))$ dependence upon the orientation of the pump electric field, θ, and probe electric field, ϕ, within the plane of the sample. The pump beam is expected to excite a superposition of T_{2x}, T_{2y}, and T_{2z} phonons. For the (111) surface of the zincblend and rocksalt structures, the experiment observations revealed that the ellipticity signals have $\sin(2(\theta-\phi))$ dependence on pump and probe polarization that is characteristic of the specular optical Kerr effect (SOKE). Hence, impulsive stimulated Raman scattering mechanism (ISRS) and the SOKE are seen to provide equivalent descriptions of the same phenomenom.

The (TSRS) theory predicts that, for a (111) surface of a cubic system, the T_{2x}, T_{2y}, and T_{2z} modes can be observed in both the reflectivity and anisotropic reflectivity signals. However, the degeneracy of these three phonons may be lifted by structural distortion, so that dephasing of modes of similar phase but different frequency leads to a large apparent damping of the phonon oscillations.

The application of high pump fluence to the InAs(111) sample was found to lead to no change in the observed phonon frequency. However exposure of one of the GST/InAs(111) samples to high pump fluence led to the appearance of a new phonon mode, suggesting that a structural change had occurred.

Acknowledgments

First and formost, I thank Allah for the completion of my thesis, and whose many blessings have helped me get to where I am today. I would like to thank King Saud University for granting me this scholarship, which has paved the way for additional growth and development in my career. I would also like to thank my supervisors Robert J Hicken and Gyaneshwar Srivastava for their endless support and guidance during my five years of research. The time and effort they have dedicated to helping me on my journey towards my PhD has been invariably in the completion of my thesis. I am grateful for the priceless knowledge that Leigh Shelford has generously shared with me regarding optical alignment and helping me in understanding the data fitting by MatLab and Origin software. He has proved to be an embodiment of knowledge and high morals as he has been very patient and helpful in answering all my questions regarding my study. I have been blessed to gain a great variety of experience and knowledge, and this would not have been possible without his support and motivation. Uday Aljarah and Shalini have been extremely helpful in training me in optical alignment procedures. I would also like to thank Haidar Mohamad and Robert Valkass who were kind and supportive in answering my questions and offering assistance in the lab and Origin software. I thank Dr. Mohammed AlSalhi, my masters degree supervisor for his concern and inquiry about my research developments during the course of my study. I would like to thank my late mother and father - may their souls rest in peace - for their continued encouragement and love throughout their lives and beyond. I would not have had my vigour and dedication throughout my years of study if it weren't for them. I owe my family in law a great deal of gratitude for taking care of my children in their school holiday during my absence from home while completing my studies in the UK, especially my husband's mother (who passed away recently), father, sister and brothers. To my own sisters and brothers, nieces and nephews, I thank you all for your constant support. Thanks to all my friends and colleagues at King Saud University for their kind encouragement. And thanks to my husband and daughters who have been a great support system throughout.

Contents

List of Figures

List of Tables

Publications

R. Alsaigh, A. Shalinin, G.P. Srivastava, R. J. Hicken and R. Calarco, *Excitation and detection of coherent optical phonon modes in epitaxial cubic* $\mathrm{Ge_2Sb_2Te_5}$ *thin films of different crystallographic orientation*, Materials Research Society Symposium Proceedings, 1661, (2014).

Declaration

Chapters 2 and 3: Theoretical Sections

These chapters include all the theory used to understand and interpret the experimental results. All the theoretical calculations presented in these two chapters were performed by myself. Prof. G P Srivastava has contributed to both chapters. The transient stimulated Raman scattering (TSRS) theory was derived by Prof. R. J. Hicken.

Chapter 4: Phase Change Material

This chapter contains information about GST material such as structure, phonon spectra and properties. All the information in this chapter has been referenced.

Chapter 5: Experimental Technique

This chapter presents the time resolved pump-probe measurement technique. The alignment of the pump-probe apparatus was the combined effort of Leigh Shelford, Haidar Mohammad and myself.

Chapter 6 and 7: Results and Discussion

The samples studied in these two chapters were provided by Raffaella Calarco from the Paul Drude Institute. The time resolved measurements of these samples were performed by myself. The fitting of the transient reflectivity and ellipticity signals was also carried out by myself. The data analysis was executed collectively by Profs R. J Hicken, G. P Srivastava, and myself. The Raman spectra of these samples were measured with the help of Mrs Ellen Green.

Appendix

Contains information about symmetry operations and point group representation. All the information in this chapter has been referenced.

1. Introduction

The invention of the laser [1] has contributed to the development of research in many areas of science and engineering. A large variety of applications in physics, chemistry, biology and medicine have been created by laser technology. The temporal width of laser pulses was decreased to a few picoseconds with the development of pulsed laser sources in 1976 [2]. Currently the minimum achievable pulse duration is estimated to be a few attoseconds [3].

With the realisation of fs-laser pulses, a new scientific field called ultrafast phenomena was created. The availability of fs-laser pulses has armed the researcher with tools with high enough temporal resolution to investigate atomic motion, phase transitions and the formation and breaking of chemical bonds in the time domain. By probing with fs-laser pulses, it is possible to resolve and analyse ultrafast processes occurring on timescales ranging from a few femtoseconds to tens of nanoseconds.

A major topic of interest in the study of ultrafast phenomena is the excitation and detection of coherent lattice vibrations. Phonon properties such as frequency, amplitude and relaxation time provide information about the material's structure. One of the most studied materials is $\mathrm{Ge_2Sb_2Te_5}$ (GST) [4, 5]. GST is one of the most commonly used materials in phase change memory applications due to the fast and reversible phase transition between its amorphous and crystalline phases, as well as the clear differences in optical and electrical properties between these two phases.

In this thesis I present comprehensive time-resolved measurements investigating the behaviour of coherent optical phonons and the structure of GST. In these measurements, a femtosecond laser pulse pumps the material, inducing a transient birefringence, which is probed by another fs-laser pulse for various orientations of the pump and probe electric

field. The electron-and lattice- dynamics following this excitation of GST have been studied by measuring the transient changes in both the intensity and ellipticity of the reflected light with a temporal resolution down to 45 fs. The dependence of the coherent optical phonon signal upon the pump and probe polarizations, sample orientation, and increased pump fluence will be described. All the theoretical considerations required to explain the experimental results in this thesis are also presented.

The Raman spectrum of the crystal plays a major role in providing information about the crystal lattice vibration frequencies. The Raman Effect has been described as the interaction of incident light of frequency ω_i with the crystal so as to create or destroy a lattice vibration, which leads to a decrease or increase in the frequency of the scattered light. Lattice vibrations with certain types of symmetry can give rise to Raman scattering and these vibrations are known as "Raman active" [6]. In Raman scattering measurements, the intensity of the scattered light is calculated from the Raman tensor, which depends on the crystal symmetry. In this thesis, the Raman tensor and Raman selection rules will be discussed in order to determine which phonon modes are Raman active in both the zinc blende and rock salt structures.

Chapter 2 explains some concepts involving phonons and the phonon dispersion curve for the zinc blende and rock salt structures. The group theory and symmetry operations of these two structures are described with the aim of understanding the Raman active modes present at the Brillouin zone centre. Both macroscopic and microscopic Raman theories are explained so as to understand the role of the Raman tensor and the associated selection rules that can be used to explain the experimental results.

Chapter 3 reviews the transient stimulated Raman scattering (TSRS) theory [7] for the generation and detection of coherent optical phonons. The mechanisms of excitation of coherent optical phonons and the experimental techniques used to detect them are also presented in this chapter.

Chapter 4 presents general information about phase change materials. In addition, the structure of GST , its phonon spectrum, and its optical and electrical properties are discussed.

The experimental set up used for the investigation of coherent optical phonons in epitaxial

$Ge_2Sb_2Te_5$/InAs(111) and InAs (111) wafer is presented in chapter 5. The pump-probe technique, a widely applicable tool for the investigation of ultrafast phenomena, is introduced. The chapter begins with a general discussion of linear and non-linear phenomena and a brief explanation of the specular optical Kerr effect (SOKE) is given. Expressions for the reflection coefficients for light reflected from a uniaxial material and the asscoiated optical rotation and ellipticity are given.

Measurements of the transient reflectivity and ellipticity of optically excited InAs (111) and $Ge_2Sb_2Te_5$/InAs(111) are presented in chapters 6 and 7 respectively. The optical phonon has been excited by 45 fs optical pulses produced by an amplified Ti:sapphire mode-locked laser. The characteristics of the coherent optical phonons that can be observed within the optical measurements are presented as a function of pump polarisation, sample orientation, and high pump fluence. The results are analysed and discussed in light of the theoretical considerations presented previously. The theory of TSRS is applied to the zinc blende and rock salt structures and used to infer the presence of T_2 phonons in InAs and GST. The phonon amplitude observed in the transient ellipticity signals obtained from InAs and GST exhibits a $\sin(2(\theta-\phi))$ that is also a characteristic SOKE-like dependence on the orientation of the pump electric field θ and probe electric field ϕ within the plane of the sample. This is shown to be consistent with the excitation of a superposition of T_{2x}, T_{2y}, and T_{2z} phonons by means of impulsive stimulated Raman scattering (ISRS). The oscillations observed in the GST/InAs (111) samples are heavily damped and strongly chirped. It is suggested that the apparently large damping is in fact depahsing that occurs because the degeneracy of the T_{2x}, T_{2y}, and T_{2z} phonons is lifted due to structural distortion.

Finally, chapter 8 summarises the experiment results and their interpretation with some suggestions of future work.

2. Phonons and Raman Theory

2.1. Introduction

This chapter will provide a brief discussion of phonons and Raman theory in zinc-blende and rock salt structures. I will begin by presenting the structures of these two crystals. I will display the phonon concepts and phonon dispersion curves of these crystals. Information about their symmetry operations is presented to understand the Raman active mode. Finally, the macroscopic and microscopic Raman theories are discussed to understand the Raman tensors and the Raman selections rules and to investigate which phonons are Raman active modes.

2.2. Face-centred cubic (fcc) lattice

The primitive translation vectors $\mathbf{a}_1$, $\mathbf{a}_2$ and $\mathbf{a}_3$ of the fcc lattice are shown in figure 2.1 . Primitive cells by definition contain only one point, but the conventional fcc cell contains four lattice points.

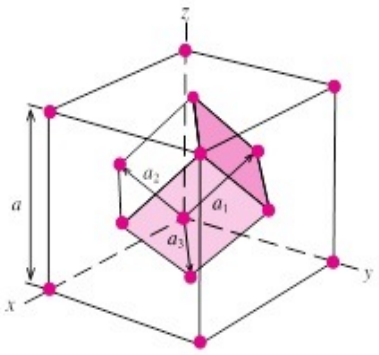

Figure 2.1.: The primitive translation vectors of the face centred cubic lattice [8].

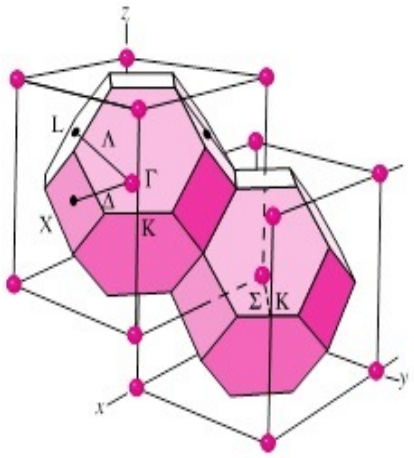

Figure 2.2.: First Brillouin zone of face centre cubic lattice [8]

The primitive translation vectors of the fcc lattice are:

$$\mathbf{a}_1 = \frac{\mathrm{a}}{2}(\hat{y} + \hat{z}); \;\; \mathbf{a}_2 = \frac{\mathrm{a}}{2}(\hat{x} + \hat{z}); \;\; \mathbf{a}_3 = \frac{\mathrm{a}}{2}(\hat{x} + \hat{y}), \tag{2.1}$$

where a is the cubic lattice constant.

The volume of the primitive cell is

$$|\mathbf{a}_1 \cdot \mathbf{a}_2 \times \mathbf{a}_3| = \frac{1}{4}\mathrm{a}^3. \tag{2.2}$$

The primitive translation vectors of the reciprocal lattice are:

$$\mathbf{b}_1 = \frac{2\pi}{\mathrm{a}}(-\hat{x},\hat{y},\hat{z}); \;\; \mathbf{b}_2 = \frac{2\pi}{\mathrm{a}}(\hat{x},-\hat{y},\hat{z}); \;\; \mathbf{b}_3 = \frac{2\pi}{\mathrm{a}}(\hat{x},\hat{y},-\hat{z}). \tag{2.3}$$

The volume of the primitive cell of the reciprocal lattice is

$$|\mathbf{b}_1 \cdot \mathbf{b}_2 \times \mathbf{b}_3| = 4(\frac{2\pi}{\mathrm{a}})^3. \tag{2.4}$$

The first Brillouin zone of the fcc lattice is formed by 8 hexagonal and 6 square faces which give truncated octahedron as in figure 2.2 [9, 10, 11] . Four high symmetry point of this Brillouin zone are $\Gamma = (0,0,0)$, $K = \frac{2\pi}{\mathrm{a}}(3/4, 3/4, 0)$, $X = \frac{2\pi}{\mathrm{a}}(1,0,0)$ and $L = \frac{2\pi}{\mathrm{a}}(1/2, 1/2, 1/2)$. The principal lines are $\Gamma - X$ (Δ), $\Gamma - L$ (Λ) and $\Gamma - K$ (Σ)[9].

2.2.1. Crystal structure with the fcc lattice

We will consider two structures with the fcc lattice within this thesis.

Sodium Chloride Structure (NaCl):

Each point in the fcc lattice has a basis of one unit of NaCl as in figure 2.3. The Na atom is at (0,0,0) and The Cl atom is at $(1/2, 1/2, 1/2)$. Each atom has six nearest neighbours of the opposite type.

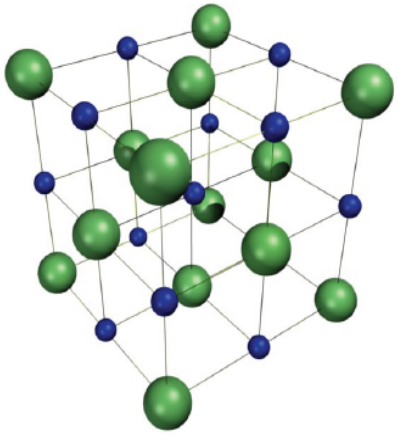

Figure 2.3.: The crystal structure of sodium chloride [12].

zinc-blend Structure:

The basis includes one atom at (0, 0, 0) and the other atom at $(1/4, 1/4, 1/4)$ as shown in figure 2.4. Each atom has four nearest neighbours located on the corners of a regular tetrahedron [10].

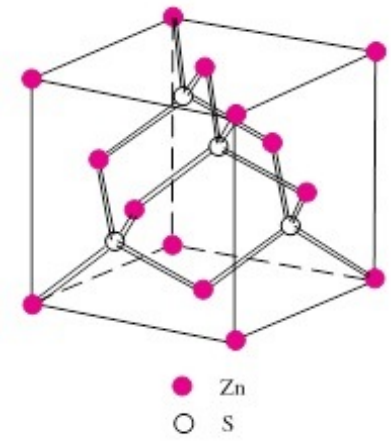

Figure 2.4.: The crystal structure of zinc-blende [8].

2.3. Symmetry operation of zinc-blende and rock salt structures

The zinc-blende point group has 24 elements identical to the elements of the point group of a tetrahedron which is denoted by $\mathrm{T_d}$. The translational symmetry operations of zinc-blende are defined in terms of the three primitive lattice vectors shown in Figure 2.1. The point group symmetry operations of the zinc-blende crystal are defined with respect to the three mutually perpendicular crystallographic axes with the origin placed at one of the two atoms in the primitive unit cell. With this choice of coordinates, the 24 operations are specified below:

E: identity;

Eight C_3 operations: clockwise and counterclockwise rotations of 120° about the $[111]$, $[\bar{1}11]$, $[1\bar{1}1]$, and $[11\bar{1}]$ axes, respectively;

Three C_2 operations: rotations of 180° about the [100], [010], and [001] axes, respectively;

Six S_4 operations: clockwise and counterclockwise improper rotations of 90° about the[100], [010], and [001] axes, respectively;

Six σ operations: reflections with respect to the (110), (1$\bar{1}$0), (101), (10$\bar{1}$), (011), and (01$\bar{1}$) planes, respectively.

The irreducible representations of the $\mathrm{T_d}$ point group are A_1 and A_2 (one dimensional representations), E (two dimensional representations) and T_1 and T_2 (three dimensional representation), see appendix 1 for more explanation.

The rock salt crystal structure has a centre of inversion symmetry. Therefore it has 48 symmetry operations consisting the symmetry operations of the $\mathrm{T_d}$ point group plus those of $\mathrm{T_d}$ followed by the inversion operation. The point group of this structure is denoted as O_h and its symmetry operations are:

E identity;

Three C_2: C_2 rotation about each of the three equivalent [100] axes;

Six S_4: two four-fold improper rotations about each of the three equivalent; [100] axes;

Six σ_d: reflection on each of the six equivalent (110) planes;

Eight C_3: two C_3 rotations about each of the four equivalent [111] axes;

i: inversion;

$3\sigma_h$: reflection on each of the three equivalent (100) planes;

$6C_4$: two C_4 rotations about each of the three equivalent [100] axes;

$6C_2^{'}$:C_2 rotation about each of the six equivalent [110] axes;

$8S_6$: two three-fold improper rotations about each of the four equivalent [111] axes.

If the point group of a crystal structure contains an inversion centre as one of its symmetry elements, then it is known as a centrosymmetric crystal (as NaCl). Crystals without an inversion centre are known as non-centrosymmetric crystal and display certain physical properties, such as the piezoelectric effect (as InAs and GaSb)[8, 13, 14, 15].

2.4. Phonons

The atoms of a crystal within the harmonic approximation are visualized as joined by harmonic spring and the crystal dynamics is analysed in terms of a linear combinations of 3N (N is the atom number) normal modes of vibrations. A normal mode of vibration behaves as a traveling wave and can be expressed as

$$A\exp[i(\mathbf{k}\cdot\mathbf{r}-\omega t)], \tag{2.5}$$

where k is the direction of wave propagation, A is the vibration amplitude and ω is the circular frequency of the wave. The normal mode energies are quantized, that means the kth mode has energy equal to

$$E_{\mathbf{k}} = (n_{\mathbf{k}} + 1/2)\hbar\omega(\mathbf{k}), \tag{2.6}$$

where $n_{\mathbf{k}}$ is the vibrational quantum number, equal to 0,1,2,... . The quantum of energy $\hbar\omega(\mathbf{k})$ is associated with an elementary excitation called a phonon. Thus the

phonon represents the quantum of crystal vibrational energy and has the concept similar to the photon of an electromagnetic wave. The phonon arises from the relative motion of atoms not from the motion of their centre of mass, therefore a phonon does not carry a momentum in the same way as the photon. For practical purposes we assign the momentum $\hbar\mathbf{k}$ to a phonon in the kth mode. Therefore the phonon is called a quasi-particle.

In thermal equilibrium the average number of phonons in the **k**th mode at temperature T is given by Bose-Einstein distribution function

$$\bar{n}_{\mathrm{k}} = \frac{1}{\exp(\hbar\omega(\mathbf{k})/k_B T) - 1}, \tag{2.7}$$

where k_B is Boltzmann's constant. This expression explains that at absolute zero there are no phonons in the crystal. If the temperature is low ($\hbar\omega \gg k_B T$) the average number of phonons is approximately equal to $\exp(-\hbar\omega/k_B T)$ and therefore there is an exponentially small probability for a phonon to be present. If the temperature is high ($k_B T \gg \hbar\omega$) the average number of phonons is approximately equal to $(k_B T/\hbar\omega)$ and therefore there is a linear increase in the number of phonons with temperature [9].

2.4.1. Acoustic and Optical, Transverse and Longitudinal Phonons, Diatomic linear chain

Consider a diatomic linear chain with N unit cells and each unit cell containing two atoms of different masses M_1 and M_2 as in figure 2.5. Consider the distance between two neighboring atoms as a.

Applying Newton's second law on the motion (longitudinal or transverse) of this structure gives its dispersion relation [10, 11, 16]:

$$\omega^2 = \Lambda(\frac{1}{M_1} + \frac{1}{M_2}) \pm \Lambda\sqrt{\left[(\frac{1}{M_1} + \frac{1}{M_2})^2 - 4\frac{(\sin(\mathrm{k}a))^2}{(M_1 M_2)}\right]}, \tag{2.8}$$

where Λ is the nearest neighbour's force constant. The $\pm$ signs give two dispersion relations and lead to two dispersion curves as in figure 2.6 . The first Brillouin zone goes

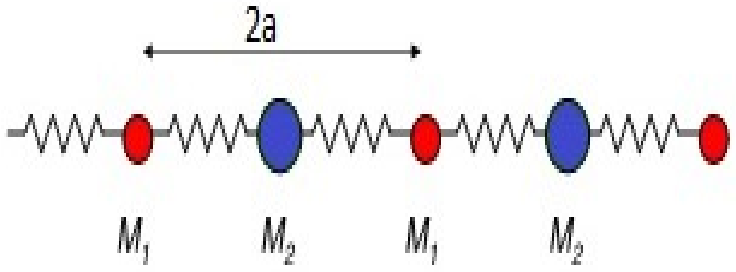

Figure 2.5.: Linear diatomic chain in one dimension.

from $-\frac{\pi}{2a} \leq \mathrm{k} \leq \frac{\pi}{2a}$. The lower curve is for acoustic modes corresponding to the minus sign. The top curve is for optical modes corresponding to the plus sign.

If $\mathrm{k} \approx 0$, ka is small, we obtain

for the optical branch

$$\omega = [2\Lambda(\frac{1}{M_1} + \frac{1}{M_2})]^{\frac{1}{2}}; \qquad \frac{A_1}{A_2} = -\frac{M_2}{M_1}, \tag{2.9}$$

for the acoustic branch

$$\omega = \left[\frac{\Lambda/2)}{M_1 + M_2}\right]^{\frac{1}{2}} \mathrm{k}a; \qquad \frac{A_1}{A_2} = 1, \tag{2.10}$$

where $A_1$and A_2 are the amplitudes of the atom displacement. In the acoustic branch when $\omega = 0$, A_1= A_2, the two atoms in unit cell have the same amplitude and move in phase. In the optical branch, $A_1M_1 + A_2M_2 = 0$, this means the two atoms move out of phase.

At the zone boundary, where $\mathrm{k} = \frac{\pi}{a}$, the solutions are

$$\omega = (\frac{2\Lambda}{M_1})^{\frac{1}{2}}; \qquad A_1/A_2 = \infty \Longrightarrow A_2 = 0 \tag{2.11}$$

$$\omega = (\frac{2\Lambda}{M_2})^{\frac{1}{2}}; \qquad A_1/A_2 = 0 \Longrightarrow A_1 = 0 \tag{2.12}$$

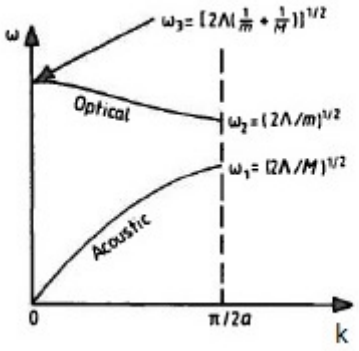

Figure 2.6.: The phonon dispersion spectrum of the diatomic linear chain [9].

In each case, one type of atom is stationary while the other vibrates. The mass of the vibrating atom determines the frequency of the mode [9, 10, 11, 16, 17, 18].

Three dimensional crystals

Consider a three-dimensional monatomic structure, where each unit cell has a single atom. The equation of displacement of each atom can be written as equation 2.5

$$\mathbf{u}_n = \boldsymbol{A} \exp[i(\mathbf{k} \cdot \mathbf{r} - \omega t)],$$

where the wave vector **k** defines the wavelength and the direction of the propagation. The vector ***A*** defines the amplitude and the direction of the atomic vibrations.

Substituting of equation 2.5 into the relevant equation of motion gives three equations including A_x, A_y and A_z which are the component of ***A***. These equations are equivalent to 3×3 matrix equation. The secular equation of this matrix gives a 3×3 determinantal equation which is cubic in ω^2. The roots of this equation gives three different dispersion relations or three dispersion curves as in figure 2.7. Since we have one atom per unit cell, all the three branches are acoustic and pass through the origin [16].

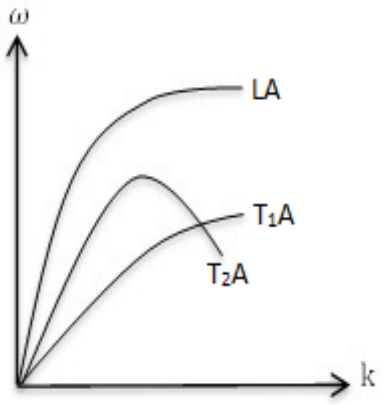

Figure 2.7.: The three acoustic branches in a three dimensional monatomic crystal.

In general, there are 3z branches for any k-direction, where z is the number of atoms per unit cell. Three of these branches are acoustic branches and 3z-3 optical branches.

Atomic vibrations corresponding to any of the branches, acoustic or optical, can be transverse ($\boldsymbol{A}\perp\mathbf{k}$) or longitudinal ($\boldsymbol{A}\parallel\mathbf{k}$) or a mixture of longitudinal and transverse. The acoustic and optical transverse are abbreviated as TA and TO respectively and the acoustic and optical longitudinal are abbreviated as LA and LO respectively. In cubic crystals the concept of pure longitudinal and transverse modes is only defined when k is along one of the symmetry directions [100], [110] and [111] [8, 9, 11].

2.4.2. Optical phonons in zinc-blende and rock salt structures

In a zinc-blend structure such as InAs and rock salt structure such as NaCl there are six phonon branches. These branches are three acoustic phonon branches (LA, $\mathrm{T_1A}$,$\mathrm{T_2A}$) and three optical phonon branches which split at the zone centre into one longitudinal (LO) mode and two doubly degenerate transverse ($\mathrm{T_1O}$,$\mathrm{T_2O}$) modes. The acoustic modes are generated with two basis atoms moving in phase with each other. The three acoustic branches at the zone center have the representation T_1 (Γ_{15}^{-}). The optic modes are generated with two basis atoms moving out of phase with each other. The three optical branches at the zone center have the representation T_2 (Γ_{25}^{+}) [19, 20]. The dispersion curves of the transverse acoustic phonons are relatively flat near the zone edge and their energies are lower than the longitudinal acoustic phonon as shown in

figure 2.8 [8, 21, 22].

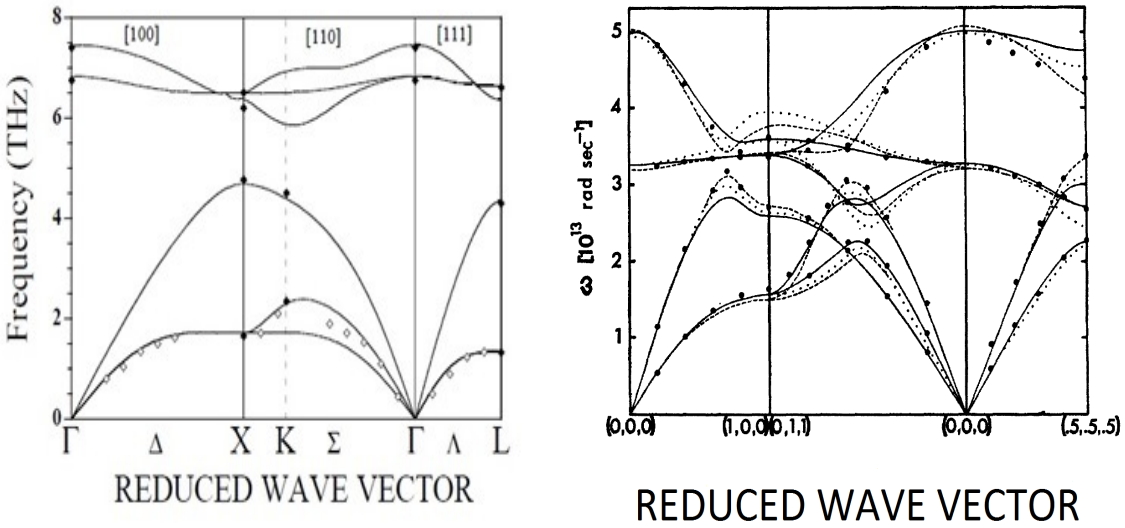

(a) InAs [9] (b) NaCl [23]

Figure 2.8.: Phonon dispersion curves for (a) InAs, (b) NaCl.

The splitting of the LO and TO branches for long-wavelength appears in almost all crystals which are heteropolar (partially ionic as InAs and GaAs) or ionic (as NaCl). This splitting is due to the electrostatic field generated by the long-wavelength modes of vibrations in such crystals [8].

As we mentioned above, for a long-wavelength optical phonon mode the two atoms in the unit cell vibrate against each other. In an ionic crystal, this optical phonon mode will create a finite polarisation density $\mathbf{P}$, which causes a macroscopic electric field $\mathbf{E}$ and an electric displacement $\mathbf{D}$.

$$\mathbf{D} = \epsilon\mathbf{E} = \mathbf{E} + 4\pi\mathbf{P}, \tag{2.13}$$

where ϵ is the dielectric constant of the medium. The quantities $\mathbf{D}$ and $\mathbf{E}$ satisfy the electrostatic equations

$$\nabla.\mathbf{D} = 0. \tag{2.14}$$

$$\nabla \times \mathbf{E} = 0. \tag{2.15}$$

In a cubic crystal **D||E||p** [24] and from equations 2.14 and 2.15 we have

For LO mode

$$\mathbf{D} = 0 \quad \mathbf{E} = -4\pi\mathbf{P}. \tag{2.16}$$

For TO mode

$$\mathbf{E} = 0. \tag{2.17}$$

This means that for a long-wavelength LO vibration there is a non-vanishing long-range electric field associated with it.

The long-wavelength vibration experiences an electrostatic restoring field in the presence of the polarisation density **P** and the electrostatic field **E** and this is given by the Lorentz relation in a cubic crystal

$$\mathbf{E}_{eff} = \mathbf{E} + 4\pi\mathbf{P}/3, \tag{2.18}$$

where $\mathbf{E}_{eff}$ is called the effective field. The equations 2.16, 2.17 and 2.18 give

For LO mode

$$\mathbf{E}_{eff} = -8\pi\mathbf{P}/3. \tag{2.19}$$

For TO mode

$$\mathbf{E}_{eff} = 4\pi\mathbf{P}/3. \tag{2.20}$$

In LO vibrations $\mathbf{E}_{eff}$ reduces the polarisation, while in TO vibrations it supports the polarisation. At the zone center the LO and TO frequencies are related by the *Lyddane-Sachs-teller* relation (LST) [25]

$$\omega_{\mathrm{LO}}^2 = (\frac{\epsilon_\circ}{\epsilon_\infty})\omega_{\mathrm{TO}}^2 \tag{2.21}$$

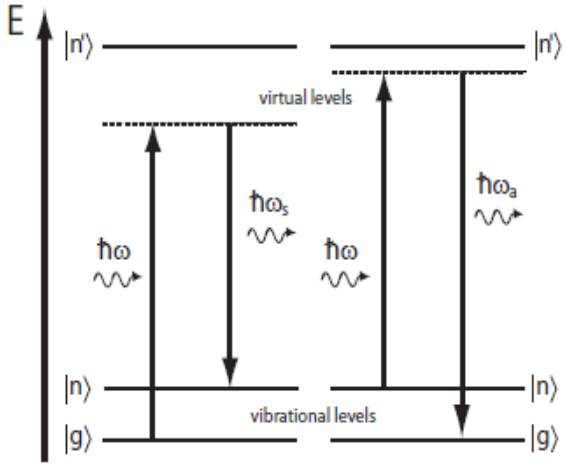

Figure 2.9.: Stokes and AntiStokes Raman scattering processes[26].

where in the crystal, $\epsilon_\circ$ and ϵ_∞ are the static and optical dielectric constants respectively. Therefore the long-wavelength LO and TO frequencies will be split by the finite amount $\omega_{\mathrm{LO}} - \omega_{\mathrm{TO}}$ in an ionic crystal [9].

2.5. Light Scattering: Rayleigh and Raman Scattering

When a material in the ground state g is illuminated by monochromatic radiation of frequency ω, it can undergo a transition to the final state n via a virtual excited state $n^\star$ by absorbing a photon with frequency ω and emitting a photon of frequency ω_s as in figure 2.9. The energy difference in this transition $\hbar\omega = (\omega - \omega_s)$ is carried away by a phonon of frequency ω_0. This process is referred to as the Stokes scattering. The material may also absorb a photon of frequency ω while undergoing a transition from n to g via a virtual level and emitting a photon of frequency ω_a. The energy difference is compensated by annihilation of a phonon of frequency $\omega_0 = (\omega_a - \omega)$. This process is referred to as the anti-Stokes scattering [26, 27, 28, 29, 30, 31].

2.6. The Raman Tensor – Macroscopic Theory

According to classical electrodynamics the emission and absorption of radiation appears in any motion of an atomic system that result in a change in the dipole moment. During the vibrational motion of a molecule the charge distribution undergoes a periodic change, and therefore in general the dipole moment changes periodically. A fundamental frequency appears as a shift in the Raman spectrum if the amplitude of the dipole moment induced by the incident radiation changes during the vibration. The magnitude of the polarisation **P** that represent the number of the dipole moment per unit volume is given by

$$|\mathbf{P}| = \chi|\mathbf{E}|, \tag{2.22}$$

where χ is the susceptibility of the medium and the electric field vector of the incident light **E** is expressed as

$$\mathbf{E}(\mathbf{r},t) = \mathbf{E}_i(\mathbf{k}_i,\omega_i)\cos(\mathbf{k}_i\cdot\mathbf{r}-\omega_i t), \tag{2.23}$$

which induces the polarisation of the material during the light- material interaction. The induced polarisation can also be expressed in the similar manner

$$\mathbf{P}(\mathbf{r},\mathbf{t}) = \mathbf{P}_i(\mathbf{k}_i,\omega_i)\cos(\mathbf{k}_i\cdot\mathbf{r}-\omega_i\mathrm{t}). \tag{2.24}$$

The frequency ω and the wave vector $\mathbf{k}$ of the polarisation are the same as the incident radiation, while the polarisation amplitude is given by

$$\mathbf{P}_i(\mathbf{k}_i,\omega_i) = \chi(\mathbf{k}_i,\omega_i)\mathbf{E}_i(\mathbf{k}_i,\omega_i). \tag{2.25}$$

The physical displacement $\mathbf{Q}(r,t)$ of atoms about their equilibrium positions due to the particular vibrational mode may be expressed by following equation 2.23 as

$$\mathbf{Q}(\mathbf{r},\mathrm{t}) = \mathbf{Q}(\mathbf{q},\omega_0)\cos(\mathbf{q}\cdot\mathbf{r}-\omega_0\mathrm{t}), \tag{2.26}$$

with wave vector **q** and frequency ω_0. For such small displacements, the susceptibility may be expanded by a Taylor series in **Q**(**r**,t), namely

$$\chi(\mathbf{k_i}, \omega_i, \mathbf{Q}) = \chi_0(\mathbf{k}_i, \omega_i) + (\partial\chi/(\partial\mathbf{Q})_0\mathbf{Q}(\mathbf{r}, \mathrm{t}) + \cdots, \tag{2.27}$$

where χ_0 denotes the electric susceptibility at the equilibrium position. The second term shows an oscillating susceptibility induced by the lattice wave. The polarisation can be expressed in the presence of the atomic vibrations by substituting 2.27 in 2.25 as

$$\mathbf{P}(\mathbf{r}, \mathrm{t}, \mathbf{Q}) = \mathbf{P}_0(\mathbf{r}, \mathrm{t}) + \mathbf{P_{ind}}\,(\mathbf{r}, \mathrm{t}, \mathbf{Q})\,, \tag{2.28}$$

where $\mathbf{P}_0(\mathbf{r}, \mathrm{t})$ is a polarisation vibrating in phase with the incident light and can be written as

$$\mathbf{P}_0(\mathbf{r}, \mathrm{t}) = \chi_0(\mathbf{k}_i, \omega_i)\mathbf{E}_i(\mathbf{k}_i, \omega_i)\cos(\mathbf{k}_i \cdot \mathbf{r} - \omega_i \mathrm{t}). \tag{2.29}$$

The $\mathbf{P_{ind}}(\mathbf{r}, \mathrm{t}, \mathbf{Q})$ is a polarisation wave induced by the phonon and can be written as

$$\mathbf{P_{ind}}(\mathbf{r}, \mathrm{t}, \mathbf{Q}) = (\partial\chi/\partial\mathbf{Q})_0\mathbf{Q}(\mathbf{r}, \mathrm{t})\mathbf{E}_i(\mathbf{k}_i, \omega_i)\cos(\mathbf{k}_i \cdot \mathbf{r} - \omega_i \mathrm{t}). \tag{2.30}$$

Using a trigonometric identity, the $\mathbf{P_{ind}}(\mathbf{r}, \mathrm{t}, \mathbf{Q})$ relation may be expanded as

$$\begin{aligned}\mathbf{P_{ind}}(\mathbf{r}, \mathrm{t}, \mathbf{Q}) = \quad & (1/2)(\partial\chi/\partial\mathbf{Q})_0\mathbf{Q}(\mathbf{q}, \omega_0)\mathbf{E}_i(\mathbf{k}_i, \omega_i, \mathrm{t}) \\ & \times \{\cos\left[(\mathbf{k}_i + \mathbf{q}) \cdot \mathbf{r} - (\omega_i + \omega_0)\mathrm{t}\right] + \cos\left[(\mathbf{k}_i + \mathbf{q}) \cdot \mathbf{r} - (\omega_i + \omega_0)\mathrm{t}\right]\}\,.\end{aligned} \tag{2.31}$$

By adding 2.29 and 2.31 the polarisation **P**(**r**,t,**Q**) can be written as

$$\begin{aligned}\mathbf{P}(\mathbf{r}, \mathrm{t}, \mathbf{Q}) = \quad & \chi_0(\mathbf{k}_i, \omega_i)\mathbf{E}_i(\mathbf{k}_i, \omega_i)\cos(\mathbf{k}_i \cdot \mathbf{r} - \omega_i \mathrm{t}) + (1/2)(\partial\chi/\partial\mathbf{Q})_0\mathbf{Q}(\mathbf{q}, \omega_0)\mathbf{E}_i(\mathbf{k}_i, \omega_i, \mathrm{t}) \\ & \times \{\cos\left[(\mathbf{k}_i + \mathbf{q}) \cdot \mathbf{r} - (\omega_i + \omega_0)\mathrm{t}\right] + \cos\left[(\mathbf{k}_i - \mathbf{q}) \cdot \mathbf{r} - (\omega_i - \omega_0)\mathrm{t}\right]\}\,.\end{aligned} \tag{2.32}$$

The above equation reveals that induced dipole moments are created at three distinct frequencies, namely $\omega_i, (\omega_i - \omega_0)$, and $(\omega_i + \omega_0)$, which results in scattered radiation at these same three frequencies. The first scattered frequency corresponds to the incident frequency, hence is elastic scattering known as Rayleigh scattered. The second frequency represent the Stokes shifted wave with wave vector $\mathbf{k}_s = (\mathbf{k}_i - \mathbf{q})$ and frequency $\omega_s = (\omega_i - \omega_0)$. The third frequency represent an anti-stokes shifted wave with wave vector $\mathbf{k}_{As} = (\mathbf{k}_i + \mathbf{q})$ and frequency $\omega_{As} = (\omega_i + \omega_0)$. The scattered light in the latter two cases is referred to as Raman scattering [8, 30].

Equation 2.32 reveals that the Stokes and the anti-stokes lines have the same frequency separation from Rayleigh line which results in them having the same energy separation from the incoming laser light. The intensity of the scattered radiation I_s (Raman scattering intensity) can be calculated from the polarisation of the incident and scattered radiation intensities e_i and e_s respectively as

$$I_s \propto |\mathbf{e}_i.(\partial\chi/\partial\mathrm{Q})_0\mathrm{Q}(\omega_0).\mathbf{e}_s|^2. \tag{2.33}$$

The atom displacement $\mathbf{Q}$ is a vector so that $(\partial\chi/\partial\mathrm{Q})$ is a third rank tensor. The Raman intensity is proportional to the atomic displacement (vibrational amplitude) squared. By introducing a unit vector $\hat{\mathrm{Q}} = \mathrm{Q}/|\mathrm{Q}|$ parallel to the atomic displacement and by taking the derivative of the susceptibility with respect to the atomic displacement we can define the Raman tensor R, which is a complex second rank tensor, as

$$R = (\partial\chi/\partial\mathrm{Q})_0\,\hat{\mathbf{Q}}(\mathbf{r}, t). \tag{2.34}$$

Therefore the Raman intensity is propositional to

$$I_s \propto |\mathbf{e}_i.R.\mathbf{e}_s|^2. \tag{2.35}$$

Equation 2.35 shows that the dependence of the intensity of the scattered light on the polarisations of the incident and scattered light plays an important role in determining the symmetry of the Raman tensor and the symmetry of the corresponding Raman

active phonons. The intensity of the scattered light vanishes for certain choices of $\mathbf{e}_i$ and $\mathbf{e}_s$ and scattering geometries as a result of the symmetries of the medium and the vibrational modes involved in the scattering. These are called Raman selection rules and are very useful for determining the symmetry of the Raman active phonons. Therefore the frequency and the symmetry of a zone centre phonon can be determined by Raman scattering, which means it is a powerful tool for studying the optical vibrational modes in a medium [8, 32].

2.6.1. Raman active and inactive modes in zinc-blende and sodium chloride structures

In equation 2.34 the quantity $(\partial\chi/\partial\mathrm{Q})$ shows the full point group symmetry of the crystal and $\mathbf{Q}$ shows the representation or symmetry of the phonon (atomic displacement). If the representation of $\mathbf{Q}$ is contained in the representation of $(\partial\chi/\partial\mathrm{Q})$ then the phonon mode can be Raman active. The phonon displacement vector $\mathbf{Q}$ can have even or odd parity under inversion symmetry. It can have even parity if the basis atoms in the crystal have the same amplitude and phase for optical vibration and can have odd parity if not. Centrosymmetric crystals such as diamond and rock salt remain invariant under inversion symmetry, therefore under the same operation $(\partial\chi/\partial\mathrm{Q})$ will not change. In the diamond structure there are two identical basis atoms, thus the optical phonon displacement vector $\mathbf{Q}$ has even parity. Therefore, the optical phonon mode is Raman active in diamond structure. In the rock salt structure there are two different basis atoms, thus the phonon displacement vector $\mathbf{Q}$ has odd parity, therefore the optical phonon mode is Raman inactive [8, 33].

The Raman selection rules shall be considered for another important structure in this study, namely zinc-blende which is adopted by GaAs, InAs and GaSb. The zincblend structure has two non-identical basis atoms, therefore it lacks inversion symmetry and $(\partial\chi/\partial\mathrm{Q})$ changes sign under the symmetry operation. The displacement pattern in this structure exhibits odd parity. Therefore, the phonon mode is Raman active in zinc-blend structure.

In zinc-blend structure the third rank tensor $(\partial\chi/\partial \mathrm{Q})$ has only one linearly independent and nonzero component, denoted by d [8]. The nonzero components of the corresponding Raman tensor are dependent on the phonon displacement vector. Consider the polarisation of the optical phonon along the x axis, its Raman tensor R(X) will have two nonzero components:

$$R_{yz}(X) = R_{zy}(X) = d.$$

The Raman tensor $R(X)$ can be represented by 3×3 matrix as:

$$R(X) = \begin{bmatrix} 0 & 0 & 0 \\ 0 & 0 & d \\ 0 & d & 0 \end{bmatrix}. \tag{2.36}$$

In the same way, the Raman tensor of the optical phonons polarized along Y and Z axes can be represented as

$$R(Y) = \begin{bmatrix} 0 & 0 & d \\ 0 & 0 & 0 \\ d & 0 & 0 \end{bmatrix}; R(Z) = \begin{bmatrix} 0 & d & 0 \\ d & 0 & 0 \\ 0 & 0 & 0 \end{bmatrix}. \tag{2.37}$$

The zone centre optical phonon in zinc-blende is split into a doubly degenerate transverse optical mode (TO) and longitudinal optical mode (LO) for $\mathrm{q} \neq 0$. The Raman tensor elements for these optical phonons are different, and therefore, to distinguish between them we can use d_{TO} and d_{LO} as the nonzero component for the transverse and longitudinal optical phonons respectively. The selection rules for Raman scattering in the zinc-blende structure can be derived by using equations 2.36 and 2.37. The advantage of using these Raman tensors is that they are able to predict the relative intensities of the scattering photon for different scattering geometries. The simplest scattering geometry is when the incident and scattered photon are antiparallel to each other. This called the backscattering geometry. The selection rules are dependent on the scattering geometrics which can be specified by four vectors expressed as $\mathbf{k}_i(\mathbf{e}_i, \mathbf{e}_s)\mathbf{k}_s$, where $\mathbf{k}_i$

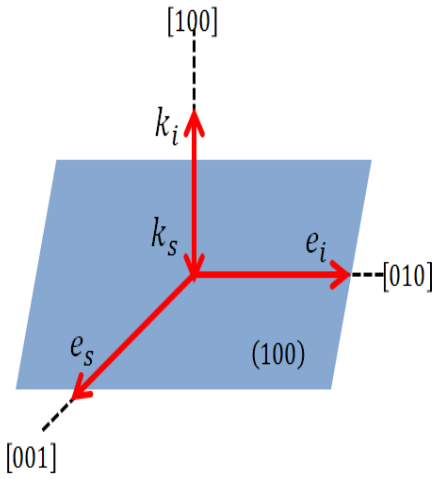

Figure 2.10.: backscattering geometry from the (100) surface for zinc-blend structure

and $\mathbf{k}_s$ are the direction of the incident and scattered photons respectively and $\mathbf{e}_i$ and $\mathbf{e}_s$ are the polarisations of the incident and scattered photons respectively [8, 34, 33]. As an example, I will consider backscattering from the (100) and (111) surfaces of the zinc-blend structure, and discuss whether the detection of TO and LO phonons is allowed or forbidden.

In the following, the Raman selection rules are derived for backscattering from the (100) surface. In this case the directions of the incident $\mathbf{k}_i$ and scattered $\mathbf{k}_s$ photons are along the x-axis [100] and the negative x-axis [$\bar{1}$00] respectively as in figure 2.10. To conserve wavevector k the phonons involved in the scattering must propagate along the x-axis.

The polarisation of the LO phonons (atom displacement $\mathbf{Q}$) must be parallel to the k direction or to the x-axis [100]. In order that $\mathbf{e}_i.R.\mathbf{e}_s$ be nonzero, one possibility of the polarisation for the incident $\mathbf{e}_i$ and the scattered photon $\mathbf{e}_s$ is that the incident photon is polarised along the y-axis [010] and the scattered photon is polarised along the z-axis [001] as in figure (2.10). For general backscattering geometry consideration, contribution from $R(X)$, $R(Y)$ and $R(Z)$ have to be included that is i.e

$$R = aR(X) + bR(Y) + cR(Z). \tag{2.38}$$

which subject to

$$a^2 + b^2 + c^2 = 1 \tag{2.39}$$

The only Raman tensor with nonzero yz elements in equation 2.36 is R(X). In this case the Raman tensor is equal to

$$R = aR(X). \tag{2.40}$$

$$R(X) = \begin{bmatrix} 0 & 0 & 0 \\ 0 & 0 & ad_{\mathrm{LO}} \\ 0 & ad_{\mathrm{LO}} & 0 \end{bmatrix}. \tag{2.41}$$

Then the Raman selection rules for LO phonons can be determined by using equation 2.35 as follows

$$R.e_s = \begin{bmatrix} 0 & 0 & 0 \\ 0 & 0 & ad_{\mathrm{LO}} \\ 0 & ad_{\mathrm{LO}} & 0 \end{bmatrix} \begin{bmatrix} 0 \\ 0 \\ \eta \end{bmatrix} = d_{\mathrm{LO}} \begin{bmatrix} 0 \\ a\eta \\ 0 \end{bmatrix}. \tag{2.42}$$

$$e_i.R.e_s = d_{\mathrm{LO}} \begin{bmatrix} 0 & \eta & 0 \end{bmatrix} \begin{bmatrix} 0 \\ a\eta \\ 0 \end{bmatrix} = a\eta^2 d_{\mathrm{LO}}. \tag{2.43}$$

We can calculate η as follows

$$e_s.e_s = 1. \tag{2.44}$$

$$\begin{bmatrix} 0 & 0 & \eta \end{bmatrix} \begin{bmatrix} 0 \\ 0 \\ \eta \end{bmatrix} = 1. \tag{2.45}$$

Thus

$$\eta = 1. \tag{2.46}$$

In the linear combination $a^2+b^2+c^2=1$ and for LO phonons the atomic displacement $\mathbf{Q}$ is parallel to $[100]$, therefore

$$a=1, b=c=0. \tag{2.47}$$

Thus the corresponding scattered intensity I_s is proportional to

$$I_s \propto |e_i.R.e_s|^2 = |d_{\mathrm{LO}}|^2. \tag{2.48}$$

In the same backscattering geometry above which can written as $x(y,z)\bar{x}$, the polarisation of the TO phonons must be perpendicular to the **k** direction or to the x-axis [100]. In this case the Raman tensor is a linear combination of R(Y) and R(Z).

$$R = aR(Y) + bR(Z). \tag{2.49}$$

$$R = a\begin{bmatrix} 0 & 0 & d_{\mathrm{TO}} \\ 0 & 0 & 0 \\ d_{\mathrm{TO}} & 0 & 0 \end{bmatrix} + b\begin{bmatrix} 0 & d_{\mathrm{TO}} & 0 \\ d_{\mathrm{TO}} & 0 & 0 \\ 0 & 0 & 0 \end{bmatrix}, \tag{2.50}$$

$$R = \begin{bmatrix} 0 & ad_{\mathrm{TO}} & bd_{\mathrm{TO}} \\ ad_{\mathrm{TO}} & 0 & 0 \\ bd_{\mathrm{TO}} & 0 & 0 \end{bmatrix}. \tag{2.51}$$

Then the Raman selection rules for TO phonons can be determined by using equation 2.35 as follows

$$R.e_s = \begin{bmatrix} 0 & ad_{\mathrm{TO}} & bd_{\mathrm{TO}} \\ ad_{\mathrm{TO}} & 0 & 0 \\ bd_{\mathrm{TO}} & 0 & 0 \end{bmatrix}\begin{bmatrix} 0 \\ 0 \\ \eta \end{bmatrix} = d_{\mathrm{TO}}\begin{bmatrix} a\eta \\ 0 \\ 0 \end{bmatrix}, \tag{2.52}$$

And

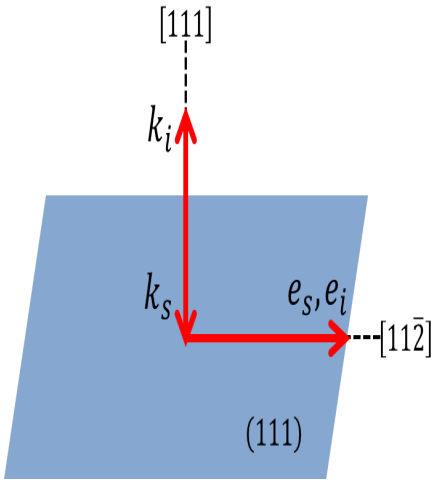

Figure 2.11.: backscattering geometry from the (111) surface for zinc-blend structure

$$e_i.R.e_s = d_{\mathrm{TO}} \begin{bmatrix} 0 & \eta & 0 \end{bmatrix} \begin{bmatrix} a\eta \\ 0 \\ 0 \end{bmatrix} = 0, \tag{2.53}$$

$$|e_i.R.e_s|^2 = 0. \tag{2.54}$$

Thus the corresponding scattered intensity I_s is equal to 0.

As a consequence in this backscattering geometry $x(y,z)\bar{x}$ or also $x(z,y)\bar{x}$ from (100) surface for zinc-blend structure, only the LO phonon participates in the light scattering and the TO phonon is forbidden or Raman inactive [35, 36, 37, 38, 39]. On the other hand, in different backscattering geometries for the same (100) surface such as $x(y,y)\bar{x}$, $x(z,z)\bar{x}$ and $x(y',z')\bar{x}$ the LO phonons is forbidden, but allowed in $x(z',y')\bar{x}$ where y' and z' denote the [011] and [0$\bar{1}$1] axes respectively.

Turning now to the backscattering geometry for the (111) surface of the zinc-blend structure, I will now differentiate the Raman selections rules for the $x"(z",z")\bar{x}"$ geometry as in figure 2.11. The $x"$, $y"$ and $z"$ denote the [111] , [1$\bar{1}$0] and [11$\bar{2}$] axes respectively. In this geometry $x"(z",z")\bar{x}"$ the directions of the incident ($\mathbf{k}_i$) and scattered ($\mathbf{k}_s$) photons are along the [111] and [$\bar{1}\bar{1}\bar{1}$] axes respectively and the polarisation of the incident ($\mathbf{e}_i$) and the scattered photon ($\mathbf{e}_s$) are along the [11$\bar{2}$]. The wavevector k must be along the [111] axis.

The polarisation of the LO phonons (atom displacement) must be parallel to the [111] axis also. In this case the Raman tensor will be

$$R = aR(X) + bR(Y) + cR(Z),$$

$$R.e_s = \left(a \begin{bmatrix} 0 & 0 & 0 \\ 0 & 0 & d_{\mathrm{LO}} \\ 0 & d_{\mathrm{LO}} & 0 \end{bmatrix} + b \begin{bmatrix} 0 & 0 & d_{\mathrm{LO}} \\ 0 & 0 & 0 \\ d_{\mathrm{LO}} & 0 & 0 \end{bmatrix} + c \begin{bmatrix} 0 & d_{\mathrm{LO}} & 0 \\ d_{\mathrm{LO}} & 0 & 0 \\ 0 & 0 & 0 \end{bmatrix} \right) \begin{bmatrix} \eta \\ \eta \\ -2\eta \end{bmatrix}, \tag{2.55}$$

$$= \eta d_{\mathrm{LO}} \begin{bmatrix} c - 2b \\ c - 2a \\ a + b \end{bmatrix}, \tag{2.56}$$

$$e_i.R.e_s = \eta d_{\mathrm{LO}} \begin{bmatrix} \eta & \eta & -2\eta \end{bmatrix}, \tag{2.57}$$

$$= 2\eta^2 d_{\mathrm{LO}}(c - 2a - 2b). \tag{2.58}$$

We can calculate η as follows

$$e_s.e_s = 1,$$

$$\begin{bmatrix} \eta & \eta & -2\eta \end{bmatrix} \begin{bmatrix} \eta \\ \eta \\ -2\eta \end{bmatrix} = 1, \tag{2.59}$$

$$6\eta^2 = 1,$$

$$\eta = 1/\sqrt{6}, \tag{2.60}$$

In the linear combination $a^2 + b^2 + c^2 = 1$ and for LO phonons the atomic displacement $\mathbf{Q}$ is parallel to $[111]$, therefore

$$a = b = c, \tag{2.61}$$

$$a^2 + a^2 + a^2 = 1 \implies a = b = c = \frac{1}{\sqrt{3}}. \tag{2.62}$$

With this then

$$e_i.R.e_s = 1/3 d_{\mathrm{LO}}(-\frac{3}{\sqrt{3}}). \tag{2.63}$$

The corresponding scattered intensity $\mathrm{I_s}$ is proportional to

$$|e_i.R.e_s|^2 = 1/3|d_{\mathrm{LO}}|^2. \tag{2.64}$$

In the case of TO phonons the polarisations of the phonons (atom displacement) must be perpendicular to the [111] axis. Therefore it is possible to be parallel to any axis perpendicular to the [111] axis. If it is parallel to the $[11\bar{2}]$ axis then the Raman tensor will be

$$R = aR(X) + bR(Y) - 2cR(Z), \tag{2.65}$$

$$R = a\begin{bmatrix} 0 & 0 & 0 \\ 0 & 0 & d_{\mathrm{TO}} \\ 0 & d_{\mathrm{TO}} & 0 \end{bmatrix} + b\begin{bmatrix} 0 & 0 & d_{\mathrm{TO}} \\ 0 & 0 & 0 \\ d_{\mathrm{TO}} & 0 & 0 \end{bmatrix} - 2c\begin{bmatrix} 0 & d_{\mathrm{TO}} & 0 \\ d_{\mathrm{TO}} & 0 & 0 \\ 0 & 0 & 0 \end{bmatrix}, \tag{2.66}$$

$$e_i.R.e_s = \begin{pmatrix} \eta & \eta & -2\eta \end{pmatrix} \left(a \begin{bmatrix} 0 & 0 & 0 \\ 0 & 0 & d_{\mathrm{TO}} \\ 0 & d_{\mathrm{TO}} & 0 \end{bmatrix} + b \begin{bmatrix} 0 & 0 & d_{\mathrm{TO}} \\ 0 & 0 & 0 \\ d_{\mathrm{TO}} & 0 & 0 \end{bmatrix} - 2c \begin{bmatrix} 0 & d_{\mathrm{TO}} & 0 \\ d_{\mathrm{TO}} & 0 & 0 \\ 0 & 0 & 0 \end{bmatrix} \right) \begin{bmatrix} \eta \\ \eta \\ -2\eta \end{bmatrix}. \tag{2.67}$$

In the linear combination $a^2 + b^2 + c^2 = 1$ and for TO phonons the atomic displacement $\mathbf{Q}$ is parallel to $[11\bar{2}]$ therefore

$$a = b,\ c = -2a, \tag{2.68}$$

Thus

$$a = \frac{1}{\sqrt{6}}, \tag{2.69}$$

and

$$\eta = 1/\sqrt{6}. \tag{2.70}$$

The corresponding scattered intensity I_s is proportional to

$$|e.R.e_s = 2/3|d_{\mathrm{TO}}|^2. \tag{2.71}$$

As a result in the backscattering geometry $x"(z", z")\bar{x}"$ for the (111) surface for the zinc-blend structure both the LO and TO phonons participate in the light scattering and both are Raman active [35, 36].

Table 2.1 summaries the relative Raman selection rules for different backscattering geometries from the zinc-blende structure [8].

Table 2.1.: The Raman selection rules for different backscattering geometries for the zinc-blende structure

Scattering geometry	Selection rule	
	TO phonon	LO phonon
$x(y,y)\bar{x}$; $x(z,z)\bar{x}$	0	0
$x(y,z)\bar{x}$; $x(z,y)\bar{x}$	0	$\lvert d_{\mathrm{LO}}\rvert^2$
$x(y^{'},z^{'})\bar{x}$;$x(z^{'},y^{'})\bar{x}$	0	0
$x(y^{'},y^{'})\bar{x}$; $x(z^{'},z^{'})\bar{x}$	0	$d_{\mathrm{LO}}\rvert^2$
$y(x,x)\bar{y}^{'}$	0	0
$y(z^{'},x)\bar{y}^{'}$	$\lvert d_{\mathrm{TO}}\rvert^2$	0
$y(z^{'},z^{'})\bar{y}^{'}$	$\lvert d_{\mathrm{TO}}\rvert^2$	0
$x^{"}(z^{"},z^{"})\bar{x}^{"}$	$\frac{2}{3}\lvert d_{\mathrm{TO}}\rvert^2$	$\frac{1}{3}d_{\mathrm{LO}}\rvert^2$
$x^{"}(z^{"},y^{"})\bar{x}^{"}$	$\frac{2}{3}\lvert d_{\mathrm{TO}}\rvert^2$	0

From the previous discussion, it can be seen that in the backscattering geometry for the (100) surface of the zinc-blend structure only the LO is the Raman active, while for the (111) surface both the LO and TO phonons are Raman active. This is in agreement with our result of Raman spectra of GaSb (001) and InAs (111) samples as will presented in chapter 4.

2.7. Atomic displacement pattern for zinc-blende and rock-salt structures

The vibrations of atoms in each material have different atomic displacement patterns depending on the crystal structure. An applied ultashort laser pulse generates coherent optical phonons in a crystal by exciting and forcing the atoms to vibrate in certain directions with a certain atomic displacement pattern. The allowed atomic vibrations in the zinc-blende structure have an atomic displacement pattern given by [21]:

$$\overrightarrow{d_1} = (0,0,z_1);(0,0,z_2) \text{ with the displacement along } [001]\,,$$

$$\overrightarrow{d_2} = (x_1,-y_1,0);(-x_2,y_2,0) \text{ with the displacement along } [\bar{1}10] \text{ or } [1\bar{1}0]\,,$$

$$\overrightarrow{d_3} = (x_1,y_1,0);(-x_2,-y_2,0) \text{ with the displacement along } [110] \text{or } [\bar{1}\bar{1}0]\,,$$

where $\overrightarrow{d_i}$ represents the allowed displacement mode and 1,2 represent the basis atoms. The atomic displacement pattern in the rock-salt structure is given by

$$\overrightarrow{d_1} = (x_1, -y_1, -z_1); (-x_2, y_2, z_2) \text{ with the displacement along} [1\bar{1}\bar{1}],$$

$$\overrightarrow{d_2} = (-x_1, -y_1, z_1); (x_2, y_2, -z_1) \text{ with the displacement along } [\bar{1}\bar{1}0],$$

$$\overrightarrow{d_3} = (-x_1, y_1, -z_1); (x_2, -y_2, z_2) \text{ with the displacement along } [\bar{1}1\bar{1}].$$

The allowed atomic displacement modes in zinc-blende and rock-salt are in three dimensions which implies that these displacement modes have the three dimensional T_2 representation [21].

2.8. Microscopic Raman Theory

The intensity of scattered light depends on the induced dipole moment **p**, which is represented by the matrix formed from the following integrals,

$$\int \psi_{\mathrm{n}}^{\star} \mathbf{p} \psi_g d\tau \tag{2.72}$$

where ψ_{g} and ψ_n are the time-dependent eigen functions (atomic displacement functions) of the system for two states g and n as shown in figure 2.9 and the dipole moment whose components are given by

$$\begin{aligned} \mathrm{p}_x = &\quad \alpha_{xx}\mathrm{E}_x + \alpha_{xy}\mathrm{E}_y + \alpha_{xz}\mathrm{E}_z \\ \mathrm{p}_y = &\quad \alpha_{yx}\mathrm{E}_x + \alpha_{yy}\mathrm{E}_y + \alpha_{yz}\mathrm{E}_z \\ \mathrm{p}_z = &\quad \alpha_{zx}\mathrm{E}_x + \alpha_{zy}\mathrm{E}_y + \alpha_{zz}\mathrm{E}_z \end{aligned} \tag{2.73}$$

Here x, y, z are the axes of the coordinate system fixed in the crystal. The $\alpha_{xx}, \alpha_{xy}, \ldots\ldots$ are the components of the polarizability tensor $\boldsymbol{\alpha}$, which are constants independent of

the directions of $\mathbf{E}$ and $\mathbf{p}$. They have the property that $\alpha_{kj} = \alpha_{jk}$ so that there are in fact only six independent functions $\alpha_{11}, \alpha_{22}, \alpha_{33}, \alpha_{12}, \alpha_{23}, \alpha_{13}$ [40, 41] to be considered, which are transformed by the symmetry operations of the point group of the crystal in exactly the same way as the functions $x^2, y^2, z^2, xy, yz, xz$ which can be formed from the coordinates (x,y,z) of a general point. The time-independent part in equation 2.72 is

$$[\mathbf{p}^\circ]^{gn} = \int \psi_n^\star \mathbf{p}^\circ \psi_g d\tau, \tag{2.74}$$

where $\mathbf{p}^\circ$ is the amplitude of $\mathbf{p}$. Substituting $\mathbf{p}$ in equations 2.72 into equation 2.73gives the components of $[\mathbf{p}^\circ]^{gn}$:

$$\begin{aligned}
[\mathrm{p}_x^\circ]^{gn} &= \mathrm{E}_x^\circ \int \alpha_{xx}\psi_n^\star\psi_g d\tau + \mathrm{E}_y^\circ \int \alpha_{xy}\psi_n^\star\psi_g d\tau + \mathrm{E}_z^\circ \int \alpha_{xz}\psi_n^\star\psi_g d\tau \\
[\mathrm{p}_x^\circ]^{gn} &= \mathrm{E}_x^\circ \int \alpha_{xy}\psi_n^\star\psi_g d\tau + \mathrm{E}_y^\circ \int \alpha_{yy}\psi_n^\star\psi_g d\tau + \mathrm{E}_z^\circ \int \alpha_{yz}\psi_n^\star\psi_g d\tau \\
[\mathrm{p}_z^\circ]^{gn} &= \mathrm{E}_x^\circ \int \alpha_{xz}\psi_n^\star\psi_g d\tau + \mathrm{E}_y^\circ \int \alpha_{yz}\psi_n^\star\psi_g d\tau + \mathrm{E}_z^\circ \int \alpha_{zz}\psi_n^\star\psi_g d\tau
\end{aligned} \tag{2.75}$$

where E_x°, E_y°, E_z° are the components of the amplitude of the incident light wave, and the integrals $[\alpha_{xx}^\circ]^{gn} = \int \alpha_{xx}\psi_n^\star\psi_g d\tau$, $[\alpha_{xy}^\circ]^{gn} = \int \alpha_{xy}\psi_n^\star\psi_g d\tau$, ...are the matrix elements of the six components of the polarizability tensor. The diagonal matrix elements (g=n) of $\boldsymbol{\alpha}$ or p° are attributed to the Rayleigh scattering and the off diagonal matrix elements are attributed to the Raman scattering. The Raman transition g→n is allowed if at least one of the six quantities$[\alpha_{xx}]^{gn}$, $[\alpha_{xy}]^{gn}$,.... does not equal zero. In other words a Raman transition between two vibrational levels is allowed if the product $\psi_n\psi_g$has the same representation as at least one of the six components α_{xx},α_{xy}, ... of the polarizability tensor [42].

If we consider the origin state ψ_g as constant, then the final state $\psi_n$will be equal to the difference between the displacement vectors $\bar{u}_{1x} - \bar{u}_{2x}$, so that $\psi_n\psi_g = \bar{u}_{1x} - \bar{u}_{2x}$, which is the relative displacement of the two basis atoms.

If we consider $\psi_n\psi_g$ to be equal a function $f(x)$ and α_{ij} equal to a function $g(x)$, then the intensity of the scattered light will given as

$$I_s = \int g(x)f(x)d\tau. \tag{2.76}$$

If the product of $g(x)f(x)$ is odd then $I_s = 0$ and if the product of $g(x)f(x)$ is even then $I_s \neq 0$.

In the diamond structure there are two identical basis atoms, therefore after applying the light the atomic displacement of the two basis atom will be the same and result in $f(x)$ being even. Also the two basis atoms remain invariant under inversion symmetry which leads to that $g(x)$ being even. As a result the intensity of scattered light $I_s \neq 0$ and the vibrational transition ψ_g to ψ_n can give rise to a line in the Raman spectrum.

In the rock salt structure the non-identical basis atoms have different atomic displacement and remain invariant under inversion symmetry, which means that $f(x)$ is odd and $g(x)$ is even. As a consequence the intensity of scattered light $I_s = 0$ and the vibrational transition ψ_g to ψ_n can not give rise to a line in the Raman spectrum.

In the zinc-blende structure the two non-identical atoms have different atomic displacement and lack the inversion symmetry, which means that $f(x)$ is odd and $g(x)$ is odd. As a result the intensity of scattered light $I_s \neq 0$ and the vibrational transition ψ_g to ψ_g can give rise to a line in the Raman spectrum.

In conclusion, in diamond and zinc-blende structures the phonon modes are Raman active and in rock salt structure they are Raman inactive.

2.9. Summary

In this chapter I have described the concept of phonons, symmetry operations and Raman theory. The irreducible representations of the zinc-blend point group $\mathrm{T_d}$ and the rock salt point group O_h are A_1, A_2, E, T_1, and T_2. The zone-centre optical phonon mode for the zinc-blend and rock salt structures has the representation T_2 . While the phonon mode is Raman active in the zinc-blend structure, it is Raman inactive in the rock salt structure. The macroscopic and microscopic Raman theories show that an optical phonon that modifies the polarisability can be Raman active in first order Raman scattering, and that

this requires the phonon displacement representation to be contained within the set of point group representations.

3. Coherent optical phonons

3.1. Introduction

The development of the ultrafast laser brought new possibilities for the time resolved detection of transient phenomena on picosecond and subpicosecond time scales. For the first time, it enabled observations on time scales shorter than period of lattice to be studied. It therefore allows material and molecules to be observed at various stages of vibrational distortion. Pump probe measurements with different photon energy, light intensity and polarisation have been performed with ultrafast laser sources, allowing impulsive stimulated processes to be studied in condensed material. One of the distinctive applications of these measurements is the investigation of coherent phonons of different materials. Among these materials is GST225 that is used in phase change memory applications. In the early work using picodecond pulses, interest focused on the excitation of lattice oscillations by a process referred to as transient stimulated Raman scattering (TSRS). A theory of TSRS will now be used to determine the expected dependence of the signal due to the coherent optical phonons (COPs) upon the pump and probe polarisation. The theory is applied in two stages, firstly to determine the excitation of the COPs by the pump, and secondly to describe the scattering of the probe beam by the COPs (the phonons modulate the polarizability of the medium). The aim of this chapter is to explain the mechanisms of excitation of coherent optical phonons and the experiment that is used to detect them.

3.2. Generation of coherent optical phonons

Laser pulses with duration sufficiently shorter than the oscillation period of fundamental lattice vibrations allow us to excite lattice modes coherently. A coherent excitation means excitation of a large number of phonons in one mode with a constant phase relation [43]. The advantages of using ultrashort laser pulses to excite coherent optical phonons are: first to measure the transient phonon dynamics not just as a time average mean displacement of atoms but also in real time; secondly it is possible to investigate the phonon relaxation time of the system [26].

The equation of motion of coherent optical phonons displacement amplitude Q can be expressed as driven harmonic oscillator [43, 44, 45].

$$m(\frac{d^2\mathrm{Q}(t)}{dt^2} + 2\gamma_{phonon}\frac{d\mathrm{Q}(t)}{dt} + \omega^2_{phonon}\mathrm{Q}(t)) = F^{\mathrm{Q}(t)}, \tag{3.1}$$

where m is the mass of the atom, γ is the damping constant, ω is the frequency of the phonons and $F^{\mathrm{Q}(t)}$ is the driving force. The Raman driving force is given by the interaction between the electromagnetic field and the susceptibility χ of the material and can be expressed as [43]

$$F^{\mathrm{Q}(t)} = \frac{1}{2}(\frac{d\chi}{d\mathrm{Q}})E_k E_l. \tag{3.2}$$

Several mechanisms have been discussed in the literature [43, 46, 7, 47, 48, 49, 50, 51, 52, 53] to solve equation (3.1). The effect of the driving force has been discussed in terms of the impulsive stimulated Raman scattering (ISRS) and displacive excitation of coherent phonons (DECP). The ISRS mechanism can occur at either a nonresonant or resonant excitation wavelength. The DECP mechanism is an impulsive absorption which can occur on resonance [46].

Figure 3.1 represents the ISRS and DECP (impulsive absorption) mechanisms. Figure 3.1 (a) represents the ISRS where the excitation wavelength is different from any electronic absorption resonance. Here, the ultrashort excitation pulse applies a sudden ("impulsive") driving force to generate coherent vibrational motion in the molecular ground electronic

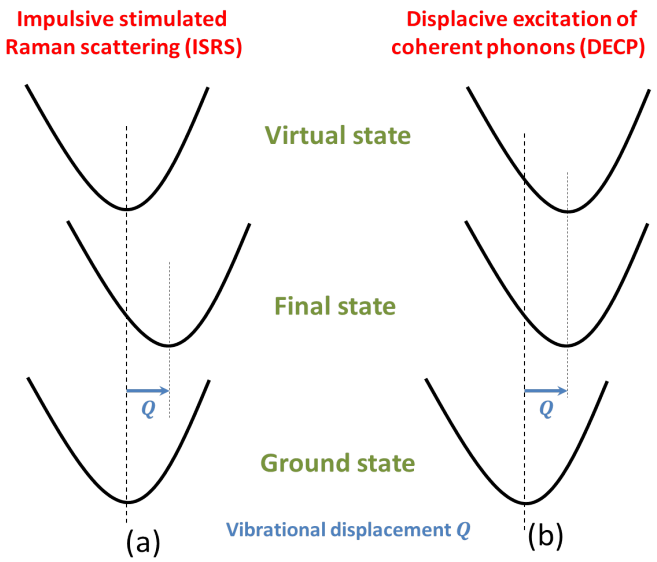

Figure 3.1.: Mechanisms (a) of impulsive stimulated Raman scattering and (b) displacive excitation coherent phonons

state. In ISRS the pulse duration of the excitation is required to be short compared with the vibrational oscillation period.

Generally, stimulated Raman scattering requires two frequencies, ω_1 and ω_2 where their difference matches the frequency of a light-scattering-active vibrational mode. The square of the superposed electric fields generates an oscillatory driving force at the difference frequency which is equal to that of the vibrational mode. This causes a phonon mode to experience forced oscillations which may continue after the effected pulses are removed. In impulsive stimulated scattering the excitation pulse is applied only for a fraction of the vibrational oscillation period, and an impulsive force on the vibrational mode is delivered instead of an oscillatory force and the generated coherent oscillations continue after the effected pulse is removed. Within the spectral bandwidth of the pulse, many frequency components are available to play the roles of ω_1 and ω_2[46]. In ISRS the time period of atomic vibration τ_o is larger than the duration of applied pulse $(\omega_2 - \omega_1)^{-1}$ [7, 54]. The system is excited from the ground state to the virtual state without appreciable change in the vibrational state (atoms do not change their positions), which means that the pulse provides kinetic energy to the system in moving to the virtual state, but when the electrons move from the virtual state to the final state, the atoms will change their positions. As a result, between the ground state and the final state there is a change in the atomic coordinates.

Figure 3.1 (b) illustrate the DECP (impulsive absorption) mechanism where the excitation wavelength is near to an electronic absorption wavelength (resonance), so absorption may occur and coherent vibrational motion may be generated in the excited electronic state in addition to the electronic ground state. Absorption of the excitation pulse creates an excited electronic state with the same geometry as the electronic ground state but with atomic position shifted from equilibrium. In this case an oscillation about the new local equilibrium position starts [46]. In DECP the time period of atomic vibration $\tau_\circ$ is shorter than the duration of applied pulse $(\omega_2 - \omega_1)^{-1}$ [7, 54]. The state of the system goes from ground state to the virtual state with atom displaced from its original position. In this case the pulse provides a potential energy change to the system while promoting it to the virtual state. There is no further change in the equilibrium atoms position as the electrons relax from the virtual state to the final state.

For both the ISRS and DECP mechanisms, there is a finite atomic displacement between the ground state and the final state. Whether this difference is the same in both mechanisms is unclear and can not be clarified easily. Later studies conclude that DECP is a spacial case of ISRS [26, 46, 54]. Therefore, we will use the language of ISRS exclusively in our further discussion.

If the pulse is Gaussian and of short duration then ISRS is more appropriate and the solution to equation (3.1) can be expressed as [7]

$$\mathrm{Q}(u) = \frac{\pi^{\frac{1}{2}}\tau_0}{4\omega} |E_\circ|^2 \, e^{-\omega^2 \frac{\tau_\circ^2}{4}} \left(\sum \frac{d\chi_{kl}}{d\mathrm{Q}} cos(\alpha_k) cos(\alpha_l) \right) e^{-\frac{\Gamma u}{2}} \sin(\omega u) \tag{3.3}$$

where $\cos(\alpha_m)$ and $\cos(\alpha_p)$ are the direction cosines of the pump electric field and $\frac{(\partial \chi_{mp})}{\partial \mathrm{Q}}$ is the Raman tensor.

3.3. Detection of optical coherent phonons

There are different methods to detect coherent optical phonons in the time domain. In this study we observe changes in the optical properties of the material that are induced by the coherent lattice displacement. We will focus on time resolves reflectivity

measurements as the method of detection.

The changes in the reflectivity of the material induced by the phonons are assumed to be small with respect to unperturbed reflectivity. The change in reflectivity $\triangle R$ can be described using the first order Raman tensor $\frac{d\chi}{d\mathrm{Q}}$ as [43]

$$\triangle R = \frac{dR}{dn}\triangle n \sim \frac{dR}{d\chi}\frac{d\chi}{d\mathrm{Q}}\mathrm{Q}, \tag{3.4}$$

where n is the refractive index. Equation (3.4) can be written in terms of real ζ_{re} and imaginary ζ_{im} parts of the refractive index as[26]

$$\triangle R = \left(\frac{dR}{d\zeta_{re}}\right)_0 .\triangle\zeta_{re} + \left(\frac{dR}{d\zeta_{im}}\right)_0 .\triangle\zeta_{im}. \tag{3.5}$$

As mentioned in the previous section, since $\frac{d\chi}{d\mathrm{Q}}$ in equation (3.3) is a tensor, so various modes can be probed selectively by polarisation analysis of the probe beam while choosing different angles for the initial polarisation of the pump and probe beams. For fully symmetric phonons the Raman tensor contains diagonal contributions of equal magnitude only. In this case the reflectivity changes will be isotropic irrespective of the polarisation of the probe pulse relative to crystallographic axes. For phonon modes with non diagonal terms in the Raman tensor, $(d\chi)\,(d\mathrm{Q})_{jk} \neq 0$ for $j \neq k$, the reflectivity changes will depend on the crystal orientation and the optical polarisation [43].

3.4. Evaluation of signals

As mentioned above the pump beam can excite COPs by impulsive stimulated Raman scattering (ISRS), and as presented in equation (3.3) for ISRS, the equation of motion of the displacement of the coherent phonon Q is similar to that of a driven harmonic oscillator and has solution of the form

$$Q \propto \sum\nolimits_{mp} \frac{(\partial\chi_{mp})}{\partial\mathrm{Q}} \cos(\alpha_m)\cos(\alpha_p). \tag{3.6}$$

Alternatively the pump beam can excite the COPs by generation of a surface space

charge (SSC) field where the electrons and holes become spatially separated due to drift in opposite directions under the influence of the built in electric field near an interface [12, 55, 56, 57]. Then it is the SSC field that appears on the right hand side of equation (3.1) and Q is independent of the pump beam polarisation.

Clearly the modulation of the polarizability caused by the COPs is then included in the wave equation for the probe beam. The solution in equation (3.3) yields the transient reflectance $\frac{\triangle R}{R}$ detected by the probe, which is found to be proportional to the phonon amplitude Q and an additional factor $\sum_{kl} \frac{(\partial \chi_{kl})}{\partial \mathrm{Q}} \cos(\beta_k) \cos(\beta_l)$, where $\cos(\beta_k)$ and $\cos(\beta_l)$ are the direction cosines of the probe electric field. If the phonon is excited by a combination of ISRS and SC field then

$$\frac{\triangle R}{R} \sim \left(C + \sum\nolimits_{mp} \frac{(\partial \chi_{mp})}{\partial \mathrm{Q}} \cos(\alpha_m) \cos(\alpha_p) \right) \left(\sum\nolimits_{kl} \frac{(\partial \chi_{kl})}{\partial \mathrm{Q}} \cos(\beta_k) \cos(\beta_l) \right), \tag{3.7}$$

where the constant C represents the contribution of the SSC field to the excitation of the COPs.

3.5. Consideration of geometrical alignment of pump and probe polarisation for the study of a cubic system.

It is necessary to consider the measurement geometry and the operation of the detector. Consider when the pump and probe electric fields lie within the (111) plane and describe angles θ and ϕ with the $[1\bar{1}0]$ axis as shown in figure 3.2. Writing the electric fields in the coordinate system defined by the orthogonal axes of the crystal,

$$\mathbf{E}_{\mathrm{pump}} = \mathrm{E}_{\mathrm{pump}}(\cos\theta \hat{u} + \sin\theta \hat{v}) \tag{3.8}$$

where $\hat{u}$ and $\hat{v}$ are the unit vectors

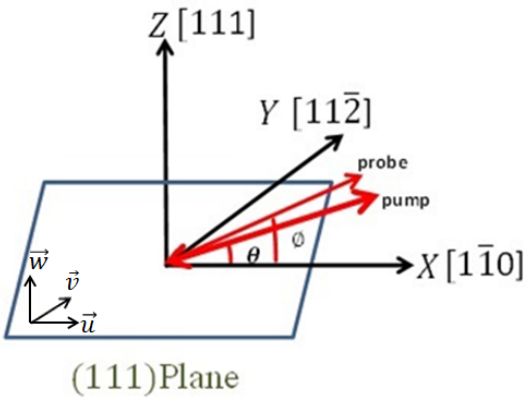

Figure 3.2.: Pump and probe measurement geometry for cubic (111) material

$$\hat{u} = \frac{1}{\sqrt{2}}(1, -1, 0) \tag{3.9}$$

$$\hat{v} = \frac{1}{\sqrt{6}}(1, 1, -2). \tag{3.10}$$

Therefore the applied electric field can be written as

$$\mathbf{E}_{\text{pump}} = E_{pump}\left(\cos\theta\left(\frac{1}{\sqrt{2}}(1, -1, 0)\right) + \sin\theta\left(\frac{1}{\sqrt{6}}(1, 1, -2)\right)\right) \tag{3.11}$$

$$\mathbf{E}_{\text{pump}} = \mathrm{E}_{\text{pump}}\left(\frac{1}{\sqrt{2}}\cos\theta + \frac{1}{\sqrt{6}}\sin\theta, -\frac{1}{\sqrt{2}}\cos\theta + \frac{1}{\sqrt{6}}\sin\theta, -\sqrt{\frac{2}{3}}\sin\theta\right) \tag{3.12}$$

The dependence of the phonon amplitude on pump electric field due to the ISRS mechanism then has the form

$$\mathrm{Q}_{\text{pump}} = \left(\frac{1}{\sqrt{2}}\cos\theta + \frac{1}{\sqrt{6}}\sin\theta, -\frac{1}{\sqrt{2}}\cos\theta + \frac{1}{\sqrt{6}}\sin\theta, -\sqrt{\frac{2}{3}}\sin\theta\right) M \begin{bmatrix} \frac{1}{\sqrt{2}}\cos\theta + \frac{1}{\sqrt{6}}\sin\theta \\ -\frac{1}{\sqrt{2}}\cos\theta + \frac{1}{\sqrt{6}}\sin\theta \\ -\sqrt{\frac{2}{3}}\sin\theta \end{bmatrix}, \tag{3.13}$$

where M is the matrix representing the Raman tensor for the particular phonon mode

within the coordinate system defined by the crystallographic axes of the sample. The probe electric field may be written as

$$\mathbf{E}_{\text{probe}} = \mathrm{E}_{\text{probe}} \left(\frac{1}{\sqrt{2}} \cos\phi + \frac{1}{\sqrt{6}} \sin\phi, -\frac{1}{\sqrt{2}} \cos\phi + \frac{1}{\sqrt{6}} \sin\phi, -\sqrt{\frac{2}{3}} \sin\phi \right). \quad (3.14)$$

The probe beam is passed into a bridge detector that consists of a polarising beam splitter and two photo diodes refered to as A and B. The polarising beam splitter is oriented so that the reflected probe beam is separated into two beams of orthogonal polarisation and equal intensity. Therefore the electric fields of these two beams are oriented at $\pm 45^0$relative to that of the probe beam and may be written as

$$\mathbf{E}_A = \mathrm{E}_{\text{probe}} \left(\frac{1}{\sqrt{2}} \cos(\phi + \frac{\pi}{4}) + \frac{1}{\sqrt{6}} \sin(\phi + \frac{\pi}{4}), -\frac{1}{\sqrt{2}} \cos(\phi + \frac{\pi}{4}) + \frac{1}{\sqrt{6}} \sin(\phi + \frac{\pi}{4}), -\sqrt{\frac{2}{3}} \sin(\phi + \frac{\pi}{4}) \right). \quad (3.15)$$

and

$$\mathbf{E}_B = \mathrm{E}_{\text{probe}} \left(\frac{1}{\sqrt{2}} \cos(\phi - \frac{\pi}{4}) + \frac{1}{\sqrt{6}} \sin(\phi - \frac{\pi}{4}), -\frac{1}{\sqrt{2}} \cos(\phi - \frac{\pi}{4}) + \frac{1}{\sqrt{6}} \sin(\phi - \frac{\pi}{4}), -\sqrt{\frac{2}{3}} \sin(\phi - \frac{\pi}{4}) \right). \quad (3.16)$$

The sum and difference of the two photodiode outputs yields the transient reflectance (R) and anisotropic reflectance (AR) response respectively.

The transient reflectance $(\frac{\triangle R}{R})$ recorded by photodiodes A and B may be written as

$$(\frac{\triangle R}{R})_A \propto (\mathrm{Q}_{\text{pump}})(\mathbf{E}_A^T M \mathbf{E}_A) \text{ and } (\frac{\triangle R}{R})_B \propto (\mathrm{Q}_{\text{pump}})(\mathbf{E}_B^T M \mathbf{E}_B). \quad (3.17)$$

The detector electronics outputs signals are then

$$S_R = (\frac{\triangle R}{R})_A + (\frac{\triangle R}{R})_B \text{ and } S_{AR} = (\frac{\triangle R}{R})_A - (\frac{\triangle R}{R})_B. \quad (3.18)$$

3.6. Crystal class consideration

Cubic crystals, such as the zinc-blend structure and rocksalt structure have respectively the $\mathrm{T_d}$ and O_h point groups which have 5 irreducible representations A, $2E$ and T_2 (T_{2x}, T_{2y}, T_{2z}). The matrix representations of the Raman tensor in each case are [6][8]

$$A\begin{bmatrix} a & 0 & 0 \\ 0 & a & 0 \\ 0 & 0 & a \end{bmatrix}, E\begin{bmatrix} b & 0 & 0 \\ 0 & b & 0 \\ 0 & 0 & b \end{bmatrix}, T_{2x}\begin{bmatrix} 0 & 0 & 0 \\ 0 & 0 & d \\ 0 & d & 0 \end{bmatrix}, T_{2y}\begin{bmatrix} 0 & 0 & d \\ 0 & 0 & 0 \\ d & 0 & 0 \end{bmatrix}, T_{2z}\begin{bmatrix} 0 & d & 0 \\ d & 0 & 0 \\ 0 & 0 & 0 \end{bmatrix}. \tag{3.19}$$

A phonon mode from one of the above representations can be detected in the R or AR signal when SR or SAR respectively in equation (3.14) are non-zero by applying equation (3.15) in equation (3.14). R or AR for cubic(111) material are given below

The dependence of the phonon amplitude on pump electric field for an A mode can be written as

$$\mathrm{Q}(A)_{\mathrm{pump}} = \left(\frac{1}{\sqrt{2}}\cos\theta + \frac{1}{\sqrt{6}}\sin\theta, -\frac{1}{\sqrt{2}}\cos\theta + \frac{1}{\sqrt{6}}\sin\theta, -\sqrt{\frac{2}{3}}\sin\theta\right)\begin{bmatrix} a & 0 & 0 \\ 0 & a & 0 \\ 0 & 0 & a \end{bmatrix}\begin{bmatrix} \frac{1}{\sqrt{2}}\cos\theta + \frac{1}{\sqrt{6}}\sin\theta \\ -\frac{1}{\sqrt{2}}\cos\theta + \frac{1}{\sqrt{6}}\sin\theta \\ -\sqrt{\frac{2}{3}}\sin\theta \end{bmatrix} \tag{3.20}$$

$$\mathrm{Q}(A)_{\mathrm{pump}} = a \tag{3.21}$$

The dependence of the reflectivity signal on probe electric field for the A mode can be written as

$$\begin{aligned} S_R(A) \quad = \quad & \mathrm{Q}(A)_{\mathrm{pump}}\left(\tfrac{1}{\sqrt{2}}\cos(\phi+\tfrac{\pi}{4}) + \tfrac{1}{\sqrt{6}}\sin(\phi+\tfrac{\pi}{4}), -\tfrac{1}{\sqrt{2}}\cos(\phi+\tfrac{\pi}{4}) + \tfrac{1}{\sqrt{6}}\sin(\phi+\tfrac{\pi}{4}), -\sqrt{\tfrac{2}{3}}\sin(\phi+\tfrac{\pi}{4})\right) \\ \times \quad & \left(\begin{bmatrix} a & 0 & 0 \\ 0 & a & 0 \\ 0 & 0 & a \end{bmatrix}\begin{bmatrix} \frac{1}{\sqrt{2}}\cos(\phi+\frac{\pi}{4}) + \frac{1}{\sqrt{6}}\sin(\phi+\frac{\pi}{4}) \\ -\frac{1}{\sqrt{2}}\cos(\phi+\frac{\pi}{4}) + \frac{1}{\sqrt{6}}\sin(\phi+\frac{\pi}{4}) \\ -\sqrt{\frac{2}{3}}\sin(\phi+\frac{\pi}{4}) \end{bmatrix}\right) \\ + \quad & \mathrm{Q}(A)_{\mathrm{pump}}\left(\tfrac{1}{\sqrt{2}}\cos(\phi-\tfrac{\pi}{4}) + \tfrac{1}{\sqrt{6}}\sin(\phi-\tfrac{\pi}{4}), -\tfrac{1}{\sqrt{2}}\cos(\phi-\tfrac{\pi}{4}) + \tfrac{1}{\sqrt{6}}\sin(\phi-\tfrac{\pi}{4}), -\sqrt{\tfrac{2}{3}}\sin(\phi-\tfrac{\pi}{4})\right) \\ \times \quad & \left(\begin{bmatrix} a & 0 & 0 \\ 0 & a & 0 \\ 0 & 0 & a \end{bmatrix}\begin{bmatrix} \frac{1}{\sqrt{2}}\cos(\phi-\frac{\pi}{4}) + \frac{1}{\sqrt{6}}\sin(\phi-\frac{\pi}{4}) \\ -\frac{1}{\sqrt{2}}\cos(\phi-\frac{\pi}{4}) + \frac{1}{\sqrt{6}}\sin(\phi-\frac{\pi}{4}) \\ -\sqrt{\frac{2}{3}}\sin(\phi-\frac{\pi}{4}) \end{bmatrix}\right) \end{aligned} \tag{3.22}$$

The reflectivity signal S_R for A mode can be written as

$$S_R(A) = a^2 \tag{3.23}$$

The dependence of the anisotropic reflectivity signal on probe electric field for the A mode can be written as

$$\begin{aligned} S_{AR}(A) &= \mathrm{Q}(A)_{\mathrm{pump}} \left(\tfrac{1}{\sqrt{2}}\cos(\phi+\tfrac{\pi}{4}) + \tfrac{1}{\sqrt{6}}\sin(\phi+\tfrac{\pi}{4}), -\tfrac{1}{\sqrt{2}}\cos(\phi+\tfrac{\pi}{4}) + \tfrac{1}{\sqrt{6}}\sin(\phi+\tfrac{\pi}{4}), -\sqrt{\tfrac{2}{3}}\sin(\phi+\tfrac{\pi}{4}) \right) \\ &\times \left(\begin{bmatrix} a & 0 & 0 \\ 0 & a & 0 \\ 0 & 0 & a \end{bmatrix} \begin{bmatrix} \frac{1}{\sqrt{2}}\cos(\phi+\frac{\pi}{4}) + \frac{1}{\sqrt{6}}\sin(\phi+\frac{\pi}{4}) \\ -\frac{1}{\sqrt{2}}\cos(\phi+\frac{\pi}{4}) + \frac{1}{\sqrt{6}}\sin(\phi+\frac{\pi}{4}) \\ -\sqrt{\frac{2}{3}}\sin(\phi+\frac{\pi}{4}) \end{bmatrix} \right) \\ &- \mathrm{Q}(A)_{\mathrm{pump}} \left(\tfrac{1}{\sqrt{2}}\cos(\phi-\tfrac{\pi}{4}) + \tfrac{1}{\sqrt{6}}\sin(\phi-\tfrac{\pi}{4}), -\tfrac{1}{\sqrt{2}}\cos(\phi-\tfrac{\pi}{4}) + \tfrac{1}{\sqrt{6}}\sin(\phi-\tfrac{\pi}{4}), -\sqrt{\tfrac{2}{3}}\sin(\phi-\tfrac{\pi}{4}) \right) \\ &\times \left(\begin{bmatrix} a & 0 & 0 \\ 0 & a & 0 \\ 0 & 0 & a \end{bmatrix} \begin{bmatrix} \frac{1}{\sqrt{2}}\cos(\phi-\frac{\pi}{4}) + \frac{1}{\sqrt{6}}\sin(\phi-\frac{\pi}{4}) \\ -\frac{1}{\sqrt{2}}\cos(\phi-\frac{\pi}{4}) + \frac{1}{\sqrt{6}}\sin(\phi-\frac{\pi}{4}) \\ -\sqrt{\frac{2}{3}}\sin(\phi-\frac{\pi}{4}) \end{bmatrix} \right) \end{aligned} \tag{3.24}$$

$$S_{AR}(A) = 0 \tag{3.25}$$

The calculations for the E mode are same as the calculations for the A mode because both have the same Raman tensor.

The dependence of the phonon amplitude on pump electric field for the T_{2x} mode can be written as

$$\mathrm{Q}(T_{2x})_{\mathrm{pump}} = \left(\frac{1}{\sqrt{2}}\cos\theta + \frac{1}{\sqrt{6}}\sin\theta, -\frac{1}{\sqrt{2}}\cos\theta + \frac{1}{\sqrt{6}}\sin\theta, -\sqrt{\frac{2}{3}}\sin\theta \right) \begin{bmatrix} 0 & 0 & 0 \\ 0 & 0 & d \\ 0 & d & 0 \end{bmatrix} \begin{bmatrix} \frac{1}{\sqrt{2}}\cos\theta + \frac{1}{\sqrt{6}}\sin\theta \\ -\frac{1}{\sqrt{2}}\cos\theta + \frac{1}{\sqrt{6}}\sin\theta \\ -\sqrt{\frac{2}{3}}\sin\theta \end{bmatrix} \tag{3.26}$$

$$\mathrm{Q}(T_{2x})_{\mathrm{pump}} = \frac{1}{\sqrt{3}} d \sin(2\theta) - \frac{2}{3} d \sin^2(\theta) \tag{3.27}$$

The dependence of the reflectivity signal on probe electric field for the T_{2x} mode can be written as

$$
\begin{aligned}
S_R(T_{2x}) &= \mathrm{Q}(T_{2x})_{\mathrm{pump}}\left(\tfrac{1}{\sqrt{2}}\cos(\phi+\tfrac{\pi}{4})+\tfrac{1}{\sqrt{6}}\sin(\phi+\tfrac{\pi}{4}),-\tfrac{1}{\sqrt{2}}\cos(\phi+\tfrac{\pi}{4})+\tfrac{1}{\sqrt{6}}\sin(\phi+\tfrac{\pi}{4}),-\sqrt{\tfrac{2}{3}}\sin(\phi+\tfrac{\pi}{4})\right)\\
&\times\left(\begin{bmatrix}0&0&0\\0&0&d\\0&d&0\end{bmatrix}\begin{bmatrix}\frac{1}{\sqrt{2}}\cos(\phi+\frac{\pi}{4})+\frac{1}{\sqrt{6}}\sin(\phi+\frac{\pi}{4})\\-\frac{1}{\sqrt{2}}\cos(\phi+\frac{\pi}{4})+\frac{1}{\sqrt{6}}\sin(\phi+\frac{\pi}{4})\\-\sqrt{\frac{2}{3}}\sin(\phi+\frac{\pi}{4})\end{bmatrix}\right)\\
&+ \mathrm{Q}(T_{2x})_{\mathrm{pump}}\left(\tfrac{1}{\sqrt{2}}\cos(\phi-\tfrac{\pi}{4})+\tfrac{1}{\sqrt{6}}\sin(\phi-\tfrac{\pi}{4}),-\tfrac{1}{\sqrt{2}}\cos(\phi-\tfrac{\pi}{4})+\tfrac{1}{\sqrt{6}}\sin(\phi-\tfrac{\pi}{4}),-\sqrt{\tfrac{2}{3}}\sin(\phi-\tfrac{\pi}{4})\right)\\
&\times\left(\begin{bmatrix}0&0&0\\0&0&d\\0&d&0\end{bmatrix}\begin{bmatrix}\frac{1}{\sqrt{2}}\cos(\phi-\frac{\pi}{4})+\frac{1}{\sqrt{6}}\sin(\phi-\frac{\pi}{4})\\-\frac{1}{\sqrt{2}}\cos(\phi-\frac{\pi}{4})+\frac{1}{\sqrt{6}}\sin(\phi-\frac{\pi}{4})\\-\sqrt{\frac{2}{3}}\sin(\phi-\frac{\pi}{4})\end{bmatrix}\right)
\end{aligned}
\tag{3.28}
$$

$$
S_R(T_{2x}) = \left(\frac{1}{\sqrt{3}}d\sin(2\theta)-\frac{2}{3}d\sin^2(\theta)\right)\left(-\frac{2}{3}d\right) \tag{3.29}
$$

The dependence of the anisotropic reflectivity signal on probe electric field for the T_{2x} mode can be written as

$$
\begin{aligned}
S_{AR}(T_{2x}) &= \mathrm{Q}(T_{2x})_{\mathrm{pump}}\left(\tfrac{1}{\sqrt{2}}\cos(\phi+\tfrac{\pi}{4})+\tfrac{1}{\sqrt{6}}\sin(\phi+\tfrac{\pi}{4}),-\tfrac{1}{\sqrt{2}}\cos(\phi+\tfrac{\pi}{4})+\tfrac{1}{\sqrt{6}}\sin(\phi+\tfrac{\pi}{4}),-\sqrt{\tfrac{2}{3}}\sin(\phi+\tfrac{\pi}{4})\right)\\
&\times\left(\begin{bmatrix}0&0&0\\0&0&d\\0&d&0\end{bmatrix}\begin{bmatrix}\frac{1}{\sqrt{2}}\cos(\phi+\frac{\pi}{4})+\frac{1}{\sqrt{6}}\sin(\phi+\frac{\pi}{4})\\-\frac{1}{\sqrt{2}}\cos(\phi+\frac{\pi}{4})+\frac{1}{\sqrt{6}}\sin(\phi+\frac{\pi}{4})\\-\sqrt{\frac{2}{3}}\sin(\phi+\frac{\pi}{4})\end{bmatrix}\right)\\
&- \mathrm{Q}(T_{2x})_{\mathrm{pump}}\left(\tfrac{1}{\sqrt{2}}\cos(\phi-\tfrac{\pi}{4})+\tfrac{1}{\sqrt{6}}\sin(\phi-\tfrac{\pi}{4}),-\tfrac{1}{\sqrt{2}}\cos(\phi-\tfrac{\pi}{4})+\tfrac{1}{\sqrt{6}}\sin(\phi-\tfrac{\pi}{4}),-\sqrt{\tfrac{2}{3}}\sin(\phi-\tfrac{\pi}{4})\right)\\
&\times\left(\begin{bmatrix}0&0&0\\0&0&d\\0&d&0\end{bmatrix}\begin{bmatrix}\frac{1}{\sqrt{2}}\cos(\phi-\frac{\pi}{4})+\frac{1}{\sqrt{6}}\sin(\phi-\frac{\pi}{4})\\-\frac{1}{\sqrt{2}}\cos(\phi-\frac{\pi}{4})+\frac{1}{\sqrt{6}}\sin(\phi-\frac{\pi}{4})\\-\sqrt{\frac{2}{3}}\sin(\phi-\frac{\pi}{4})\end{bmatrix}\right)
\end{aligned}
\tag{3.30}
$$

$$
S_{AR}(T_{2x}) = \left(\frac{1}{\sqrt{3}}d\sin(2\theta)-\frac{2}{3}d\sin^2(\theta)\right)\left(\frac{2}{\sqrt{3}}d\cos(2\phi)-\frac{2}{3}d\sin(2\phi)\right) \tag{3.31}
$$

The dependence of the phonon amplitude on pump electric field for the T_{2y} mode can be written as

$$
\mathrm{Q}(T_{2y})_{\mathrm{pump}} = \left(\frac{1}{\sqrt{2}}\cos\theta+\frac{1}{\sqrt{6}}\sin\theta,-\frac{1}{\sqrt{2}}\cos\theta+\frac{1}{\sqrt{6}}\sin\theta,-\sqrt{\frac{2}{3}}\sin\theta\right)\begin{bmatrix}0&0&d\\0&0&0\\d&0&0\end{bmatrix}\begin{bmatrix}\frac{1}{\sqrt{2}}\cos\theta+\frac{1}{\sqrt{6}}\sin\theta\\-\frac{1}{\sqrt{2}}\cos\theta+\frac{1}{\sqrt{6}}\sin\theta\\-\sqrt{\frac{2}{3}}\sin\theta\end{bmatrix} \tag{3.32}
$$

$$\mathrm{Q}(T_{2y})_{\mathrm{pump}} = -\frac{1}{\sqrt{3}} d \sin(2\theta) - \frac{2}{3} d \sin^2(\theta) \tag{3.33}$$

The dependence of the reflectivity signalon probe electric field for the T_{2y} mode can be written as

$$\begin{aligned}
S_R(T_{2y}) &= \mathrm{Q}(T_{2y})_{\mathrm{pump}} \left(\tfrac{1}{\sqrt{2}} \cos(\phi + \tfrac{\pi}{4}) + \tfrac{1}{\sqrt{6}} \sin(\phi + \tfrac{\pi}{4}), -\tfrac{1}{\sqrt{2}} \cos(\phi + \tfrac{\pi}{4}) + \tfrac{1}{\sqrt{6}} \sin(\phi + \tfrac{\pi}{4}), -\sqrt{\tfrac{2}{3}} \sin(\phi + \tfrac{\pi}{4}) \right) \\
&\times \left(\begin{bmatrix} 0 & 0 & d \\ 0 & 0 & 0 \\ d & 0 & 0 \end{bmatrix} \begin{bmatrix} \frac{1}{\sqrt{2}} \cos(\phi + \frac{\pi}{4}) + \frac{1}{\sqrt{6}} \sin(\phi + \frac{\pi}{4}) \\ -\frac{1}{\sqrt{2}} \cos(\phi + \frac{\pi}{4}) + \frac{1}{\sqrt{6}} \sin(\phi + \frac{\pi}{4}) \\ -\sqrt{\frac{2}{3}} \sin(\phi + \frac{\pi}{4}) \end{bmatrix} \right) \\
&+ \mathrm{Q}(T_{2y})_{\mathrm{pump}} \left(\tfrac{1}{\sqrt{2}} \cos(\phi - \tfrac{\pi}{4}) + \tfrac{1}{\sqrt{6}} \sin(\phi - \tfrac{\pi}{4}), -\tfrac{1}{\sqrt{2}} \cos(\phi - \tfrac{\pi}{4}) + \tfrac{1}{\sqrt{6}} \sin(\phi - \tfrac{\pi}{4}), -\sqrt{\tfrac{2}{3}} \sin(\phi - \tfrac{\pi}{4}) \right) \\
&\times \left(\begin{bmatrix} 0 & 0 & d \\ 0 & 0 & 0 \\ d & 0 & 0 \end{bmatrix} \begin{bmatrix} \frac{1}{\sqrt{2}} \cos(\phi - \frac{\pi}{4}) + \frac{1}{\sqrt{6}} \sin(\phi - \frac{\pi}{4}) \\ -\frac{1}{\sqrt{2}} \cos(\phi - \frac{\pi}{4}) + \frac{1}{\sqrt{6}} \sin(\phi - \frac{\pi}{4}) \\ -\sqrt{\frac{2}{3}} \sin(\phi - \frac{\pi}{4}) \end{bmatrix} \right)
\end{aligned} \tag{3.34}$$

$$S_R(T_{2y}) = \left(-\frac{1}{\sqrt{3}} d \sin(2\theta) - \frac{2}{3} d \sin^2(\theta) \right) \left(-\frac{2}{3} d \right) \tag{3.35}$$

The dependence of the anisotropic reflectivity signalon probe electric field for the T_{2y} mode can be written as

$$\begin{aligned}
S_{AR}(T_{2y}) &= \mathrm{Q}(T_{2y})_{\mathrm{pump}} \left(\tfrac{1}{\sqrt{2}} \cos(\phi + \tfrac{\pi}{4}) + \tfrac{1}{\sqrt{6}} \sin(\phi + \tfrac{\pi}{4}), -\tfrac{1}{\sqrt{2}} \cos(\phi + \tfrac{\pi}{4}) + \tfrac{1}{\sqrt{6}} \sin(\phi + \tfrac{\pi}{4}), -\sqrt{\tfrac{2}{3}} \sin(\phi + \tfrac{\pi}{4}) \right) \\
&\times \left(\begin{bmatrix} 0 & 0 & d \\ 0 & 0 & 0 \\ d & 0 & 0 \end{bmatrix} \begin{bmatrix} \frac{1}{\sqrt{2}} \cos(\phi + \frac{\pi}{4}) + \frac{1}{\sqrt{6}} \sin(\phi + \frac{\pi}{4}) \\ -\frac{1}{\sqrt{2}} \cos(\phi + \frac{\pi}{4}) + \frac{1}{\sqrt{6}} \sin(\phi + \frac{\pi}{4}) \\ -\sqrt{\frac{2}{3}} \sin(\phi + \frac{\pi}{4}) \end{bmatrix} \right) \\
&- \mathrm{Q}(T_{2y})_{\mathrm{pump}} \left(\tfrac{1}{\sqrt{2}} \cos(\phi - \tfrac{\pi}{4}) + \tfrac{1}{\sqrt{6}} \sin(\phi - \tfrac{\pi}{4}), -\tfrac{1}{\sqrt{2}} \cos(\phi - \tfrac{\pi}{4}) + \tfrac{1}{\sqrt{6}} \sin(\phi - \tfrac{\pi}{4}), -\sqrt{\tfrac{2}{3}} \sin(\phi - \tfrac{\pi}{4}) \right) \\
&\times \left(\begin{bmatrix} 0 & 0 & d \\ 0 & 0 & 0 \\ d & 0 & 0 \end{bmatrix} \begin{bmatrix} \frac{1}{\sqrt{2}} \cos(\phi - \frac{\pi}{4}) + \frac{1}{\sqrt{6}} \sin(\phi - \frac{\pi}{4}) \\ -\frac{1}{\sqrt{2}} \cos(\phi - \frac{\pi}{4}) + \frac{1}{\sqrt{6}} \sin(\phi - \frac{\pi}{4}) \\ -\sqrt{\frac{2}{3}} \sin(\phi - \frac{\pi}{4}) \end{bmatrix} \right)
\end{aligned} \tag{3.36}$$

$$S_{AR}(T_{2y}) = \left(-\frac{1}{\sqrt{3}} d \sin(2\theta) - \frac{2}{3} d \sin^2(\theta) \right) \left(-\frac{1}{\sqrt{3}} d \cos(2\phi) - \frac{1}{3} d \sin(2\phi) \right) \tag{3.37}$$

The dependence of the phonon amplitude on pump electric field for the T_{2z} mode can be written as

$$\mathrm{Q}(T_{2z})_{\mathrm{pump}} = \left(\frac{1}{\sqrt{2}}\cos\theta + \frac{1}{\sqrt{6}}\sin\theta, -\frac{1}{\sqrt{2}}\cos\theta + \frac{1}{\sqrt{6}}\sin\theta, -\sqrt{\frac{2}{3}}\sin\theta\right) \begin{bmatrix} 0 & d & 0 \\ d & 0 & 0 \\ 0 & 0 & 0 \end{bmatrix} \begin{bmatrix} \frac{1}{\sqrt{2}}\cos\theta + \frac{1}{\sqrt{6}}\sin\theta \\ -\frac{1}{\sqrt{2}}\cos\theta + \frac{1}{\sqrt{6}}\sin\theta \\ -\sqrt{\frac{2}{3}}\sin\theta \end{bmatrix} \tag{3.38}$$

$$\mathrm{Q}(T_{2z})_{\mathrm{pump}} = -d\cos^2(\theta) + \frac{1}{3}d\sin^2(\theta) \tag{3.39}$$

The dependence of the reflectivity signal on probe electric field for the T_{2z} mode can be written as

$$\begin{aligned} S_R(T_{2z}) &= \mathrm{Q}(T_{2z})_{\mathrm{pump}} \left(\tfrac{1}{\sqrt{2}}\cos(\phi+\tfrac{\pi}{4}) + \tfrac{1}{\sqrt{6}}\sin(\phi+\tfrac{\pi}{4}), -\tfrac{1}{\sqrt{2}}\cos(\phi+\tfrac{\pi}{4}) + \tfrac{1}{\sqrt{6}}\sin(\phi+\tfrac{\pi}{4}), -\sqrt{\tfrac{2}{3}}\sin(\phi+\tfrac{\pi}{4})\right) \\ &\times \left(\begin{bmatrix} 0 & d & 0 \\ d & 0 & 0 \\ 0 & 0 & 0 \end{bmatrix} \begin{bmatrix} \frac{1}{\sqrt{2}}\cos(\phi+\frac{\pi}{4}) + \frac{1}{\sqrt{6}}\sin(\phi+\frac{\pi}{4}) \\ -\frac{1}{\sqrt{2}}\cos(\phi+\frac{\pi}{4}) + \frac{1}{\sqrt{6}}\sin(\phi+\frac{\pi}{4}) \\ -\sqrt{\frac{2}{3}}\sin(\phi+\frac{\pi}{4}) \end{bmatrix}\right) \\ &+ \mathrm{Q}(T_{2z})_{\mathrm{pump}} \left(\tfrac{1}{\sqrt{2}}\cos(\phi-\tfrac{\pi}{4}) + \tfrac{1}{\sqrt{6}}\sin(\phi-\tfrac{\pi}{4}), -\tfrac{1}{\sqrt{2}}\cos(\phi-\tfrac{\pi}{4}) + \tfrac{1}{\sqrt{6}}\sin(\phi-\tfrac{\pi}{4}), -\sqrt{\tfrac{2}{3}}\sin(\phi-\tfrac{\pi}{4})\right) \\ &\times \left(\begin{bmatrix} 0 & d & 0 \\ d & 0 & 0 \\ 0 & 0 & 0 \end{bmatrix} \begin{bmatrix} \frac{1}{\sqrt{2}}\cos(\phi-\frac{\pi}{4}) + \frac{1}{\sqrt{6}}\sin(\phi-\frac{\pi}{4}) \\ -\frac{1}{\sqrt{2}}\cos(\phi-\frac{\pi}{4}) + \frac{1}{\sqrt{6}}\sin(\phi-\frac{\pi}{4}) \\ -\sqrt{\frac{2}{3}}\sin(\phi-\frac{\pi}{4}) \end{bmatrix}\right) \end{aligned} \tag{3.40}$$

$$S_R(T_{2z}) = \left(-d\cos^2(\theta) + \frac{1}{3}d\sin^2(\theta)\right)\left(\frac{2}{3}d\right) \tag{3.41}$$

The dependence of the anisotropic reflectivity signal on probe electric field for the T_{2z} mode can be written as

$$\begin{aligned} S_{AR}(T_{2z}) &= \mathrm{Q}(T_{2z})_{\mathrm{pump}} \left(\tfrac{1}{\sqrt{2}}\cos(\phi+\tfrac{\pi}{4}) + \tfrac{1}{\sqrt{6}}\sin(\phi+\tfrac{\pi}{4}), -\tfrac{1}{\sqrt{2}}\cos(\phi+\tfrac{\pi}{4}) + \tfrac{1}{\sqrt{6}}\sin(\phi+\tfrac{\pi}{4}), -\sqrt{\tfrac{2}{3}}\sin(\phi+\tfrac{\pi}{4})\right) \\ &\times \left(\begin{bmatrix} 0 & d & 0 \\ d & 0 & 0 \\ 0 & 0 & 0 \end{bmatrix} \begin{bmatrix} \frac{1}{\sqrt{2}}\cos(\phi+\frac{\pi}{4}) + \frac{1}{\sqrt{6}}\sin(\phi+\frac{\pi}{4}) \\ -\frac{1}{\sqrt{2}}\cos(\phi+\frac{\pi}{4}) + \frac{1}{\sqrt{6}}\sin(\phi+\frac{\pi}{4}) \\ -\sqrt{\frac{2}{3}}\sin(\phi+\frac{\pi}{4}) \end{bmatrix}\right) \\ &- \mathrm{Q}(T_{2z})_{\mathrm{pump}} \left(\tfrac{1}{\sqrt{2}}\cos(\phi-\tfrac{\pi}{4}) + \tfrac{1}{\sqrt{6}}\sin(\phi-\tfrac{\pi}{4}), -\tfrac{1}{\sqrt{2}}\cos(\phi-\tfrac{\pi}{4}) + \tfrac{1}{\sqrt{6}}\sin(\phi-\tfrac{\pi}{4}), -\sqrt{\tfrac{2}{3}}\sin(\phi-\tfrac{\pi}{4})\right) \\ &\times \left(\begin{bmatrix} 0 & d & 0 \\ d & 0 & 0 \\ 0 & 0 & 0 \end{bmatrix} \begin{bmatrix} \frac{1}{\sqrt{2}}\cos(\phi-\frac{\pi}{4}) + \frac{1}{\sqrt{6}}\sin(\phi-\frac{\pi}{4}) \\ -\frac{1}{\sqrt{2}}\cos(\phi-\frac{\pi}{4}) + \frac{1}{\sqrt{6}}\sin(\phi-\frac{\pi}{4}) \\ -\sqrt{\frac{2}{3}}\sin(\phi-\frac{\pi}{4}) \end{bmatrix}\right) \end{aligned} \tag{3.42}$$

$$S_{AR}(T_{2z}) = \left(-d\cos^2(\theta) + \frac{1}{3}d\sin^2(\theta)\right)\left(\frac{4}{3}d\sin(2\phi)\right) \qquad (3.43)$$

Table 1 summaries which kind of phonon can be generated and detected in the transient R and AR signals for cubic(111) and cubic(001) materials by displaying the form of the dependence upon the pump and probe polarisations. The A and E modes can only be detected in the R signal, while T_{2x}, T_{2y} and T_{2z} can be detected in both the R and the AR signals for the cubic (111), while T_{2z} can only be detected in the AR signal for cubic (001) material. While the optical phonons in the zincblende (GaSb and InAs substrate materials) are Raman active, the optical phonons in the ideal rocksalt structure are Raman inactive.

Table 3.1.: Observability of phonon modes (A, E, and T_2) for the (001) and (111) surfaces of crystals with O_h point group symmetry. In COPs measurements the angles θ and ϕ are defined relative to the [100] and $[111]$axes for the (001) and (111) surfaces.

Mode	Transient Reflectivity (S_R)		Transient anisotropic reflectivity (S_{AR})	
	cubic(001)	cubic(111)	cubic(001)	cubic111)
A	a^2	a^2	0	0
E	a^2	a^2	0	0
E	a^2	a^2	0	0
T_{2x}	0	$\left(\frac{1}{\sqrt{3}}d\sin(2\theta) - \frac{2}{3}d\sin^2(\theta)\right)$ $\left(-\frac{2}{3}d\right)$	0	$\left(\frac{1}{\sqrt{3}}d\sin(2\theta) - \frac{2}{3}d\sin^2(\theta)\right)$ $\left(\frac{2}{\sqrt{3}}d\cos(2\phi) - \frac{2}{3}d\sin(2\phi)\right)$
T_{2y}	0	$\left(-\frac{1}{\sqrt{3}}d\sin(2\theta) - \frac{2}{3}d\sin^2(\theta)\right)$ $\left(-\frac{2}{3}d\right)$	0	$\left(-\frac{1}{\sqrt{3}}d\sin(2\theta) - \frac{2}{3}d\sin^2(\theta)\right)$ $\left(-\frac{2}{\sqrt{3}}d\cos(2\phi) - \frac{2}{3}d\sin(2\phi)\right)$
T_{2z}	0	$\left(-d\cos^2(\theta) + \frac{1}{3}d\sin^2(\theta)\right)\left(-\frac{2}{3}d\right)$	$d^2\sin(2\theta)\cos(2\phi)$	$\left(-d\cos^2(\theta) + \frac{1}{3}d\sin^2(\theta)\right)$ $\left(\frac{4}{3}d\sin(2\phi)\right)$

3.7. Summary

A theory of transient stimulated Raman scattering TSRS has been used to determine the expected dependence of the coherent optical phonons (COP) signal upon the pump and probe polarisation. The theory shows firstly that the pump beam can excite COPs by either impulsive stimulated Raman scattering ISRS or by creation of a surface space charge SSC field. Secondly, if the phonon is generated by the ISRS mechanism then for the (111) plane of a cubic system A and E phonon modes can be detected only in the R

signal without any dependence on pump and probe polarisations. However T_2 phonons can be detected in both R and AR signals.

4. Phase change materials

4.1. Background

Phase change materials (PCM) are used in phase change random access memory (PCRM). This material changes between amorphous and crystalline phases rapidly when excited by laser light or electric current. The amorphous and crystalline phases of the same material exhibit different optical and electrical properties, in particular their reflectivity and resistivity. Heating the amorphous phase for a long enough time above the material crystallization temperature switches it to the crystalline phase; this process is called the SET operation. Melting and quenching quickly enough, the material switches to the amorphous phase; this process is called the RESET operation [58].

The difference in the optical and electrical properties enables these materials to store information, and this concept was recognized by Ovshinsky [59] and published in the 1960s [60]. Ovshinsky established that chalcogenide alloys of $\mathrm{Te_{48}As_{30}Si_{21}Ge_{10}}$ system can be switched repeatedly between a high and a low conductivity state [60]. Early attempts to develop this concept were obstructed by the fact that the first alloys studied needed long crystallization times, in the microsecond range, which required a large switching current.

The first use of a laser-induced phase change in $\mathrm{Te_{81}Ge_{15}Sb_2S_2}$ alloys was by Feinleib et al [61]. The difference in optical reflectivity between the amorphous and crystalline phases was used to store the information. The $\mathrm{Te_{81}Ge_{15}Sb_2S_2}$ alloys showed a long crystallization time of microseconds, too slow for a viable technology [62]. In 1987 phase change research and information storage technology developed when Yamada et al[63] discovered fast-switching materials. These materials are in the pseudobinary line

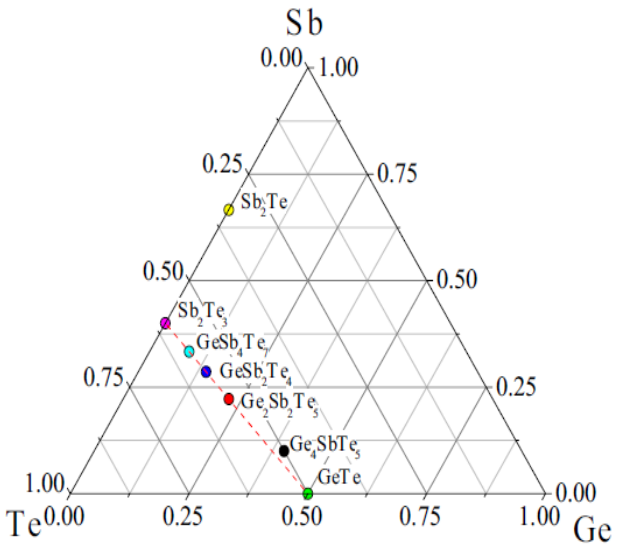

Figure 4.1.: Typical compositions of phase change materials [65]

between GeTe and Sb_2Te_3 . Figure 4.1 shows these materials and the alloys that have been used in optical storage products. The solid line shows the $GeTe - Sb_2Te_3$ tie line, on which many phase change alloys that have short crystallization time are located. The breakthrough discovery of these materials enabled the rewritable phase change optical storage technology to become successful today. A number of companies have projects to investigate phase change random access memory (PCRAM) with a view to developing a commercial product [64].

4.2. Properties of phase change materials

Phase change materials possess properties that make them useful for technological applications such as optical storage and PCRAM. The PCMs should have both crystalline and amorphous phases that are stable for many years at the operating temperature. The material needs to be able to switch repeatedly for many cycles: 10^5 times typically for optical storage, $10^6 - 10^8$ times to replace flash memory, 10^{12} times for embedded memory, and up to $10^{15} - 10^{17}$ times to replace standalone or embedded DRAM (dynamic RAM). Therefore the material must not change its chemical composition and must not react with its surroundings and contact materials. The crystallization time, which affects the data rate, should be short. The quenching process needs to be faster than the

crystallization process, therefore the melt-quenching operation must to be fast. Large optical and electrical contrasts are required in the PCMs [64].

4.3. Principles of the phase transition in phase change materials

The principle of the phase change process is illustrated in figure 4.2. The switching between the crystalline and amorphous phase is achieved by applying a precisely controlled amount of heat. Depending on the technological application, if it is optical or electronic data storage, either laser pulses or electrical pulses are used as the heat source. To switch from crystalline to amorphous phase, a short high intensity pulse (high current) is used to increase the temperature of the chosen region above the melting temperature $\mathrm{T_I}$. As the high temperature is only developed within a limited region, a large temperature difference is achieved between the liquid and the rest of the material, resulting in increased cooling levels of approximately $10^{10}\mathrm{K/s}$. If the temperature falls fast enough below the glass transition temperature $\mathrm{T_g}$ a melt-quenched amorphous bit will be formed. To switch back to the crystalline phase, a high temperature must be developed within the chosen region for an adequate amount of time with the atomic mobilities at a level for the crystallization to be achieved. Therefore the material has to be heated above the glass transition temperature [66, 67].

4.4. $\mathrm{Ge_2Sb_2Te_5}$(GST) structure

The most commonly used and most studied PCM is $\mathrm{Ge_2Sb_2Te_5}$ (GST). This material possesses three phases, the amorphous phase which crystallizes upon heating to $140°C$ to a metastable rock salt structure, and then at $310°C$ to a stable crystalline hexagonal structure.

X-ray diffraction (XRD) studies of thin GST layers have shown that the GST crystalizes into a metastable rock salt-like structure with Te atoms occupying the anion sites of the structure. The $\mathrm{Ge, Sb}$ and some vacancies occupy the cation sites [68, 69, 70,

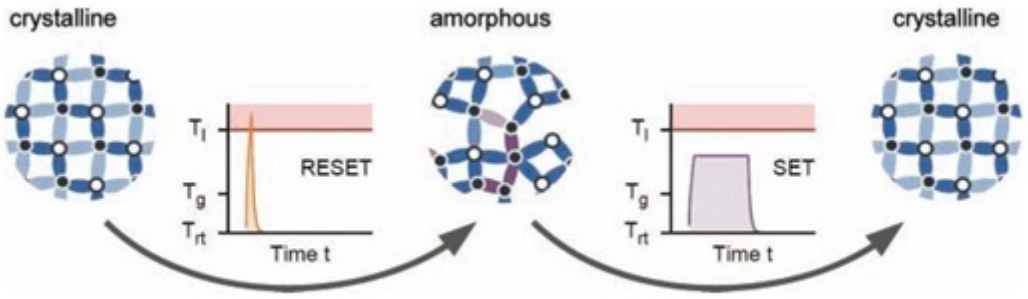

Figure 4.2.: The principle of the phase transition in phase change material. The variation of temperature with time is shown for the SET and RESET processes where $\mathrm{T_I}$ is the melting temperature and $\mathrm{T_g}$ is the glass or crystallization temperature [66].

63, 71]. This metastable phase has an octahedral-like coordination with short and long Te-Ge bonds [68, 66]. No $\mathrm{Sb-Ge}$ bonds are observed and a next-nearest-neighbour $\mathrm{Te-Te}$ peak is detected [69]. Another study by Wuttig and Steimer revealed that one characteristic feature of this rock salt structure is the presence of three short and three long $\mathrm{Ge-Te}$ bonds, where every Ge atom has 6 nearest neighbours [67].

Another X-ray diffraction study of laser-crystalized thin films of $\mathrm{Ge_2Sb_{2+x}Te_5}$ $(0{\leq}x{\leq}1)$ composition showed that the material consists of two phases: one is a rock salt-like structure and the other includes a small amount of an amorphous Sb phase where the 4(a) site is occupied by only Te atoms and the 4(b) site is occupied by Ge and Sb atoms and vacancies. That is, Sb atoms never occupy the vacancy sites. However Sb atoms can segregate into an amorphous phase at the grain boundaries [72].

The local atomic arrangement of the amorphous state is approximately similar to the crystalline state but with a lack of long-range order [73]. On melting, the longer $\mathrm{Te-Ge}$ (and $\mathrm{Te-Sb}$) bonds are broken, leaving shorter and stronger bonds, which means that the amorphous phase is locally more organized than the crystalline. Also the Te second-nearest-neighbour peak becomes weaker [68].

Extended X-ray absorption fine structure (EXAFS) measurements of the amorphous state reveal that the tetrahedral atomic arrangement of the Ge atoms in amorphouse state has an octahedral-like atomic arrangement in the crystalline state [68, 69, 66, 73]. Kolobov et al have described the transition between the amorphous and the crystalline states

as an umbrella flip. The homopolar $\mathrm{Te}-\mathrm{Te}$ and $\mathrm{Sb}-\mathrm{Sb}$ bonds were not observed, while $\mathrm{Ge}-\mathrm{Sb}$ and $\mathrm{Ge}-\mathrm{Ge}$ bonds were revealed. These latter bonds are called "wrong bonds" because they are not present in the idealised rock-salt structure. The coordination number of the amorphous state approximately satisfies the 8-N rule. The amorphous state consists of defective octahedral sites, where Ge atoms exist in both tetrahedral and octahedral arrangement. The tetrahedral arrangement contains one third of the Ge atoms in $\mathrm{Ge_2Sb_2Te_5}$ [66, 74, 75].

Wuttig and Yamada have reported that the amorphous structure has a spinel structure where the Ge atoms have tetrahedral coordination with four nearest Te neighbours, while the Te and Sb atoms positions are similar to those in the rock salt structure [73].

Huang and Robertson revealed that there is no medium range order (MRO) at the next-nearest-neighbor in the amorphous phase of phase change materials. Therefore, the transition from crystalline to amorphous has a change in MRO and it is not simply a change of coordination of individual atoms, for instance through an umbrella flip of Ge atoms [66, 76].

4.5. Phonon spectra of $\mathrm{Ge_2Sb_2Te_5}$

Theoretical and experimental studies of $\mathrm{Ge_2Sb_2Te_5}$ have investigated its long wavelength phonon modes. In the crystalline state, dominant degenerate E_g modes at 3.6 ± 0.1THz have been observed. This mode is associated with vibrations of atoms in planes normal to the c axis in $\mathrm{Sb_2Te_3}$ [77, 4, 78]. In contrast, this frequency corresponds to an A_1 mode in $\mathrm{GeTe_4}$ [79] or in octahedral $\mathrm{GeTe_6}$ [80]. Two A_{1g} modes appear at 2THz and at 4.9 ± 0.1 THz. These two modes are attributed to symmetrical vibrations of Sb and Te outer layers, where the mode at 2 THz is due to an in phase oscillation [77] while the mode at 4.9 ± 0.1 THz is due to an out of phase oscillation [77, 4].

For the amorphous phase, a dominant symmetrical A_1 mode at 3.7 ± 0.2 THz was observed and associated with $\mathrm{GeTe_4}$ tetrahedra [77, 4, 80]. Also a symmetric A_1 mode appears at 4.7 ± 0.1 THz and has been attributed to either disordered Te-Te chains [80] or the $\mathrm{Sb_2Te_3}$ sub-units [77]. Theoretical studies depends on the calculated Raman spectra

of GST material from ab initio phonon and empirical polarizability coefficients within the bond polarizability model (BPM) investigated by experimental Raman spectrum, two modes in crystalline GST one at 110cm^{-1} (3.29 THz) and a weaker mode at 160 cm^{-1} (4.79 THz). However, the same study revealed that in amorphous GST two modes at 129 cm^{-1} (3.86 THz) and 152 cm^{-1} (4.55 THz) and a much weaker mode at 100 cm^{-1} (2.99 THz). A calculation of the Raman spectrum of amorphous GST revealed one mode at 143 cm^{-1} (4.2 THz) and a shoulder at 160 cm^{-1} (4.79 THz), which were attributed to vibrations of defective octahedra [81].

4.6. Optical and electrical properties of GST

The phase change materials (PCMs) possess special optical and electrical properties that have led to their successful technological application. For optical data storage, knowledge of the efficiency of excitation and optical contrast at different laser wavelengths is necessary. Therefore the optical constants, the index of refraction n, the extinction coefficient k, and the absorption coefficient α are important. The optical constants depend on the film thickness as well as the wavelength λ [82, 83, 84, 85]. Figure 4.3 shows the optical constants of the amorphous, rocksalt and hexagonal phases of $\mathrm{Ge_2Sb_2Te_5}$. . The figure shows similar behaviour for the rock-salt and hexagonal phases [86], but a large difference between the amorphous and rock-salt phases. The complex index of refraction can be defined by the following equation

$$\tilde{n} = n + ik$$

Here, the real part of the refractive index n indicates the phase velocity, while the imaginary part k indicates the amount of absorption loss when the electromagnetic wave propagates through the material. For the phase change material the crystalline state has high reflectivity, while the amorphous state has low reflectivity. These differences are due to the differences in the structure between the two phases. In fact, the crystalline structure includes shorter and longer bonds. The longer bonds, which are weaker, lead to a smaller energy splitting between the bonding and antibonding states and smaller

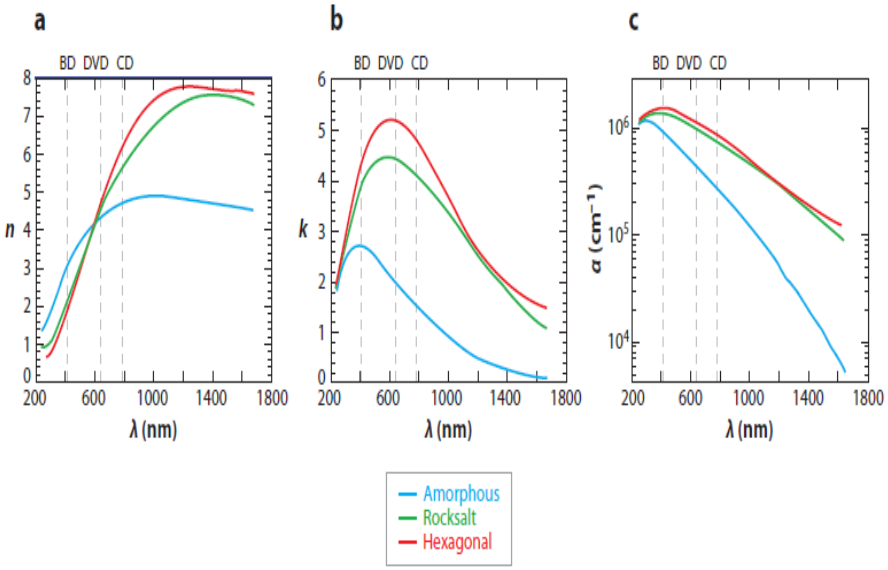

Figure 4.3.: Optical constants (a) n, (b) k, and (c) α of the amorphous, rocksalt and hexagonal phases of $Ge_2Sb_2Te_5$. CDs, DVDs and BD marks the laser wavelength used for rewritable CD, DVD and blue ray discs respectively[64].

band edges and the width of the band gap, which is smaller in this state, resulting in higher absorption and reflectivity. On the other hand, in the amorphous state, the weaker bonds break and disappear while the stronger bonds become shorter and stronger. As a consequence, the splitting between bonding and antibonding states increases, producing a larger band gap implying lower absorption and reflectivity [87]. For $Ge_2Sb_2Te_5$ the optical band gap of the amorphous phase is $\sim 0.7\mathrm{eV}$ and $\sim 0.5\mathrm{eV}$ for the rocksalt and hexagonal phases [84].

For electrical storage, the resistivity is an important electrical parameter. For the amorphous PCMs, for voltages that equate to a small applied electric field, the electric current shows a linear dependence on voltage, while for larger voltages an exponential increase is observed as shown in figure 4.4.

At the threshold voltage the resistivity drops suddenly by an order of magnitude, and this is known as threshold switching. This effect is useful because otherwise it would be impossible to deliver sufficient power, and hence to heat the sample sufficiently, in the amorphous phase using a reasonable voltage. Increasing the voltage above the threshold voltage leads to a sufficient decrease in the resistance that the material can be heated above its crystallization (glass) temperature $\mathrm{T_g}$. After the threshold switching, if the voltage is switched off for a short time, the resistivity will increase and the material will

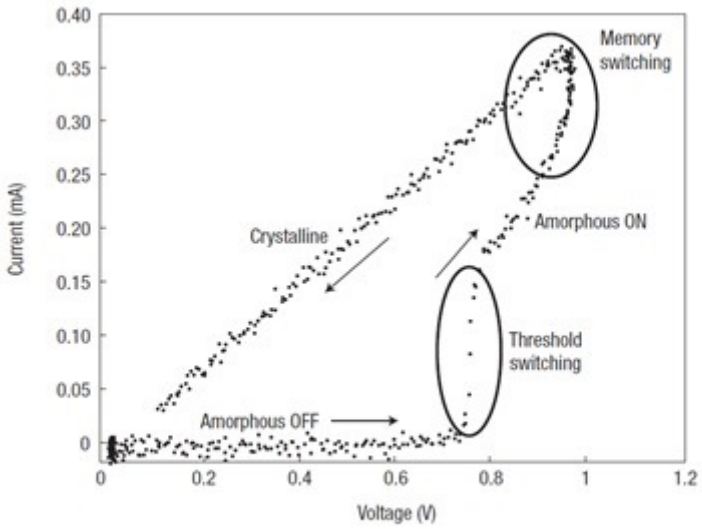

Figure 4.4.: Current-voltage curve of phase change material [73]

return to the amorphous phase. Only if the material is heated above $\mathrm{T_g}$ for a sufficiently long time will it crystalize into the more conducting crystalline phase [66, 88, 64].

$\mathrm{Ge_2Sb_2Te_5}$ has high crystallization speed as a result of the weak bonding which leads to a low viscous force among atoms and increased atomic mobility. On the other hand, crystallization from the amorphous to the crystalline structure occurs without phase separation into different compositions. Atoms travel only a short distance to transform the amorphous phase to the crystalline phase. This yields the fast crystallization from the amorphous to the crystalline phase [64, 85].

4.7. Summary

This chapter summaries that the $\mathrm{Ge_2Sb_2Te_5}$ (GST) material possesses three phases, the amorphous phase, crystalline phase and hexagonal phase. Theoretical and experimental studies of the structure of GST indicate that the cubic crystalline phase has a rock salt-like structure where Ge atoms have an octahedral-like atomic environment, while the Ge atoms in the amorphous state have a tetrahedral atomic environment. The transition between the amorphous and the crystalline states has been described as an umbrella flip. Furthermore existing theoretical and experimental studies of GST attributed different phonon modes to vibrations involving different bonds. A change in the structure between

the two phases leads to a change in optical and electrical properties and leads to GST being widely used and used for technological applications.

5. Experimental techniques

5.1. Introduction

In this chapter I will describe the tools and the experimental techniques that were used to perform the time resolved measurements of optical properties. In particular, a pump-probe technique has been used to perform time resolved reflectivity and ellipticity measurements of laser excited $Ge_2Sb_2Te_5$ and InAs crystals with femtosecond time resolution.

This chapter will begin with a brief review of linear and non-linear phenomena followed by a brief explanation of the specular optical kerr effect (SOKE). The optical reflection coefficients are explained so as to describe the rotation of the polarisation and ellipticity that are induced by the pump pluses. The time resolved pump-probe technique used to measure the transient reflectivity and ellipticity signals is described. Finally the process used to fit the experimental data is explained.

5.2. Linear and nonlinear phenomena

The terms linear and non-linear describe phenomena that are independent of or dependent on the optical intensity respectively, as shown in figure 5.1. When an electromagnetic wave propagates through a medium the medium becomes electrically polarized. For a small electric field amplitude, the polarisation P is linearly proportional to the applied electric field and usually written in the form

$$\mathrm{P} = \varepsilon_{\circ}\chi E, \tag{5.1}$$

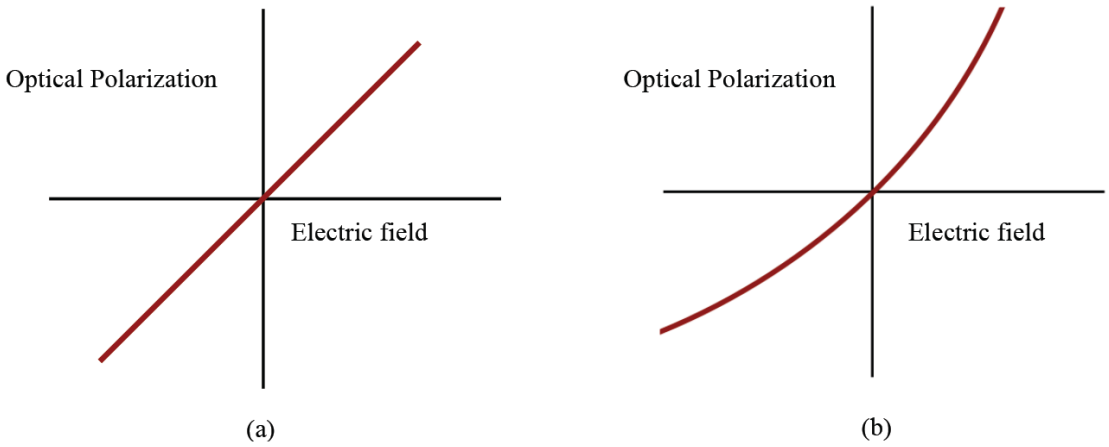

Figure 5.1.: (a) Linear and (b) nonlinear response of polarisation P to an applied electric field E [12]

where χ is the linear susceptibility and $\varepsilon_\circ$ is the permittivity of vacuum. The linear susceptibility is related to the refractive index of the medium by $\chi = n^2 - 1$ and in general is a 2nd rank tensor with symmetry that reflects that of the crystal structure.

If the magnitude of the applied electric field is large, the induced polarisation may have a non-linear dependence on the electric field amplitude and it is possible to represent the modification of the susceptibility in a nonlinear medium by a power series of the form

$$\chi_{ij}(E) = \chi_{ij}^{(1)} + \chi_{ijk}^{(2)} E_k + \chi_{ijkl}^{(3)} E_k E_l + ... \tag{5.2}$$

Thus the induced polarisation can be written as

$$\mathbf{P} = \varepsilon_\circ(\chi_{ij}^{(1)} + \chi_{ijk}^{(2)} E_k + \chi_{ijkl}^{(3)} E_k E_l + ...)\boldsymbol{E}, \tag{5.3}$$

where $\chi_{ijk}^{(2)}$ is the second order nonlinear susceptibility (tensor of rank 3) and $\chi_{ijkl}^{(3)}$ is the third order nonlinear susceptibility (tensor of rank 4). The second and third order nonlinear susceptibilities give rise to non-linear optical phenomena. For example the $\chi_{ijk}^{(2)}$ is responsible for second harmonic generation, where the frequency of the emitted photon is double the frequency of the incident photon. The third order nonlinear susceptibility is responsible for the optical Kerr effect and stimulated Raman scattering where the incident light changes the refractive index of the material [89, 27, 90, 91].

5.3. Specular optical Kerr effect (SOKE)

When the surface of a medium is illuminated by light, a fraction of the incident light is reflected and the rest transmitted. The reflection of light can be roughly categorized into two types: specular reflection where the excited electrons obey momentum conservation, and diffuse reflection where the drift velocity of the electrons is completely destroyed, so that electrons scatter to a random momentum state which means momentum is not conserved [92].

The all-optical pump-probe technique using femtosecond laser pulses is a powerful tool that can be used to investigate carrier transport processes in materials. While transient reflectivity signals can provide the time constant for thermalisation of hot electrons, the transient polarisation signal can explore the excitation and relaxation of transient linear and angular momentum. The two lowest order contributions to the transient polarisation signal result from the specular-optical Kerr effect (SOKE) and the specular inverse Faraday effect (SIFE).

"The SOKE (SIFE) may appear when pumping a solid material with a linearly (circularly) polarized pump beam, which transfers linear (angular) momentum to electrons in the surface of the sample, and induces a transient linear (circular) birefringence that causes the polarisation state of a time-delayed probe beam to be modified. Thus the transient polarisation signal explores information about the rate of relaxation of the linear and angular momentum of the excited electrons. For metals the relevant relaxation times are of the order of 10 fs. Therefore in measurements made with 100 fs pulses, the SIFE and SOKE are expected to appear as a peak in the transient polarisation signal with width determined by that of the laser pulse. However, if the electron momentum is coupled to another sub-system within the sample that relaxes more slowly, the peak may be followed by a tail from which the characteristic relaxation times of that sub-system may be determined" [93, 94].

In this study the SOKE peak has been studied through measurements of the transient ellipticity. The amplitude of transient rotation of polarisation and ellipticity due to the SOKE can be related to certain components of the susceptibility tensor. If the rotation

of polarisation and ellipticity of the applied pump and probe beams are (θ_1, η_1) and (θ_2, η_2) respectively, and if the probe beam is linearly polarized, which means $(\eta_2 = 0)$, then for an isotropic or cubic crystal the change in probe polarisation upon reflection may be expressed as

$$\begin{pmatrix} \triangle\theta_1 \\ \triangle\eta_2 \end{pmatrix} = -\frac{32\pi^2 I_{pump}}{c\,|1+n|^2} \left\{ \sin 2(\theta_1 - \theta_2)\cos 2\eta_1 \begin{pmatrix} Re \\ Im \end{pmatrix} \frac{\chi_{xxyy} + \chi_{xyyx}}{n(1-n^2)} + \sin 2\eta_1 \begin{pmatrix} -Im \\ Re \end{pmatrix} \frac{\chi_{xxyy} - \chi_{xyyx}}{n(1-n^2)} \right\}, \tag{5.4}$$

where c is the speed of light, n is the complex refractive index of the medium and I_{pump} is the intensity of the pump beam. The first term within this expression represents the contribution due to the SOKE, while the second term represent that due to the SIFE [94, 95, 96, 97]..

5.4. Jones matrix and reflectivity calculations

When light passes through an interface between two media which have different optical properties, one part is reflected back into the first medium while another part is transmitted into the second medium as shown in figure 5.2. The reflectivity of the sample is defined as the ratio of the reflected light intensity I_r to the incident light intensity I_i.

$$R = \frac{I_r}{I_i}. \tag{5.5}$$

The reflection and transmission of polarized light can be described by means of Jones matrices. When polarized light crosses an optical element, the polarisation of the emerging light is calculated by taking the product of the Jones vector of the incident light and Jones matrix of the optical element. The relative amplitude and the relative phase of the electric field are represented by a Jones vector and the optical elements are represented by Jones matrices. The s-polarized and p-polarized electric field components $E_s^{(r)}$ and $E_p^{(r)}$ of the reflected light can be related to the incident electric field components $E_s^{(i)}$ and $E_p^{(i)}$ by

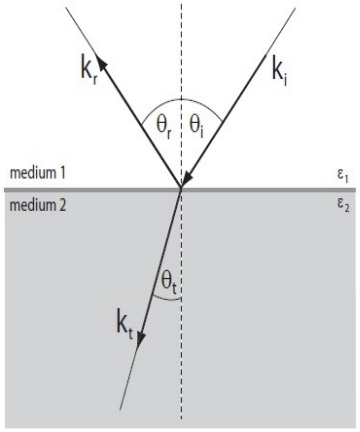

Figure 5.2.: Wave vectors of incident ($\mathbf{k}_i$), reflected ($\mathbf{k}_r$) and transmitted ($\mathbf{k}_t$) beams at an interface between two media with different refractive indices [26]

$$\begin{pmatrix} E_s^{(r)} \\ E_p^{(r)} \end{pmatrix} = \begin{pmatrix} r_{ss} & r_{sp} \\ r_{ps} & r_{pp} \end{pmatrix} \begin{pmatrix} E_s^{(i)} \\ E_p^{(i)} \end{pmatrix}, \tag{5.6}$$

where r_{ss} , r_{ps} , r_{pp} , r_{sp} are the reflection coefficients [98].

By implementing the Jones calculations, the reflectivity for incident light polarized at angle ϕ to the plane of incidence is

$$R = (|r_{ss}|^2 + |r_{ps}|^2)\sin^2\phi + (|r_{pp}|^2 + |r_{sp}|^2)\cos^2\phi + \frac{1}{2}(r_{ss}r_{sp}^* + r_{pp}r_{ps}^*)\sin^2\phi. \tag{5.7}$$

The rotation and the elllipticity of the reflected light for incident p and s polarized light are given by

For p-polarized light

$$\phi = -Re\left\{\frac{r_{sp}}{r_{pp}}\right\}, \varepsilon = Im\left\{\frac{r_{sp}}{r_{pp}}\right\}. \tag{5.8}$$

For s- polarized light

$$\phi = Re\left\{\frac{r_{ps}}{r_{ss}}\right\}, \varepsilon = Im\left\{\frac{r_{sp}}{r_{pp}}\right\}. \tag{5.9}$$

For an isotropic material the off-diagonal components r_{sp} and r_{ps} in equation 5.5 are equal to zero, while in an anisotropic material the off-diagonal components are in general non zero. As a result in an anisotropic material the incident p (or s) polarized light will induce a s (or p) polarized electric field component in the reflected light. If the incident light is not perfectly p or s polarized, the plane of polarisation may be rotated upon reflection even for an isotropic medium. Therefore to measure the rotation caused by the optical Kerr effect, the incident light should be exactly p or s polarized.

5.5. Rotation signal calculations

Within this thesis, the polarisation of the reflected probe beam will be detected through the use of an optical bridge shown in figure 5.3. The polarizing beam splitter of the bridge detector is oriented so that the reflected probe beam is separated into two beams of orthogonal polarisation and equal intensity. Therefore the electric fields of these two beams are oriented at $\pm 45^{\circ}$ relative to that of the probe beam. The output of each photodiode is proportional to the intensity incident upon it, namely $I_{\circ}$ before the pump beam induces any birefringence within the sample, and may be written as

$$I_{\circ} \propto \frac{E_{\circ}^2}{2}, \tag{5.10}$$

where $E_{\circ}$ is the amplitude of reflected probe beam before the pump beam induces a birefringence in the sample. The output of the bridge detector is proportional to the difference in intensity incident upon the two photo diodes.

In this case the output difference signal from the bridge can be written as

$$S \, \alpha \, I_A - I_B, \tag{5.11}$$

where I_A and I_B are the intensities incident upon the two photodiodes. It is straightforward to show that the difference of the photodiode outputs (S) is proportional to the rotation of the probe polarisation (θ) induced by the pump beam. Suppose that the

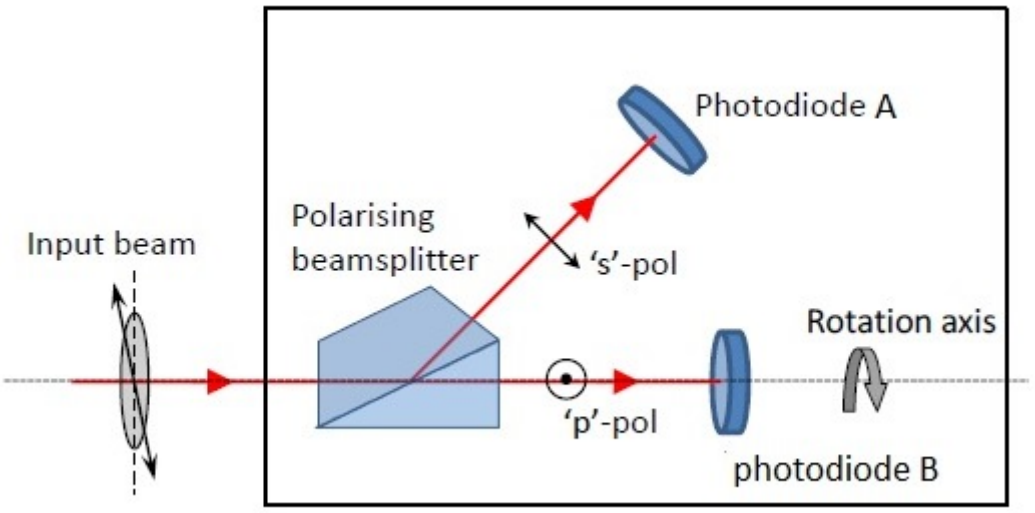

Figure 5.3.: Schematic diagram of optical bridge detector [99]

electric field of the incident beam is defined within the (x',y') coordinate system and we need to express the electric field in the (x,y) coordinate system ,which is rotated by angle θ with respect to the (x',y') system. The appropriate matrix to represent rotation by an angle θ about the origin is

$$\begin{pmatrix} \cos\theta & -\sin\theta \\ \sin\theta & \cos\theta \end{pmatrix}. \tag{5.12}$$

Therefore the electric field in the (x,y) system is related to that in the (x',y') system by

$$\begin{pmatrix} E_x \\ E_y \end{pmatrix} = \begin{pmatrix} \cos\theta & -\sin\theta \\ \sin\theta & \cos\theta \end{pmatrix} \begin{pmatrix} E_{x'} \\ E_{y'} \end{pmatrix}, \tag{5.13}$$

where E_x and E_y are the electric field components in the (x,y) system and $E_{x'}$ and $E_{y'}$ are the electric field components in (x',y') system.

The polarized pump beam induces a transient linear birefringence that causes the polarisation state of the time-delayed probe beam to be modified. If the reflected elliptically polarised probe beam has its major axis rotated by an angle θ by the pump-induced birefringence in the sample, then its electric field components in the (x',y') coordinate system can be expressed as

$$E_{x'} = E_\circ \cos(\omega t) \tag{5.14}$$

$$E_{y'} = E_\circ \sin(\varepsilon) \sin(\omega t), \tag{5.15}$$

where ε is the ellipticity of the probe beam and we have assumed $\varepsilon << 1$. Let us now set the (x,y) coordinate system to be parallel to the electric field components accepted by photodiodes A and B The electric field components x and y can be calculated by using equation 5.13 as

$$\begin{pmatrix} E_x \\ E_y \end{pmatrix} = \begin{pmatrix} \cos(\frac{\pi}{4}+\theta) & -\sin(\frac{\pi}{4}+\theta) \\ \sin(\frac{\pi}{4}+\theta) & \cos(\frac{\pi}{4}+\theta) \end{pmatrix} \begin{pmatrix} E_\circ \cos(\omega t) \\ E_\circ \sin(\varepsilon)\sin(\omega t) \end{pmatrix}. \tag{5.16}$$

Thus

$$E_x = E_\circ \cos(\omega t)\cos(\frac{\pi}{4}+\theta) - E_\circ \sin(\varepsilon)\sin(\omega t)\sin(\frac{\pi}{4}+\theta). \tag{5.17}$$

$$E_y = E_\circ \cos(\omega t)\sin(\frac{\pi}{4}+\theta) + E_\circ \sin(\varepsilon)\sin(\omega t)\cos(\frac{\pi}{4}+\theta). \tag{5.18}$$

The beam intensity at the first photodiode can be written as

$$I_A \propto \frac{\bar{E_x^2}}{2}. \tag{5.19}$$

$$I_A \propto \frac{1}{2\tau}\int_0^\tau E_\circ^2(\cos(\omega t)\cos(\frac{\pi}{4}+\theta) - \sin(\varepsilon)\sin(\omega t)\sin(\frac{\pi}{4}+\theta))^2 d\tau. \tag{5.20}$$

$$I_A \propto \frac{E_\circ^2}{2\tau}\int_0^\tau (\cos^2(\omega t)\cos^2(\frac{\pi}{4}+\theta) - \sin^2(\varepsilon)\sin^2(\omega t)\sin^2(\frac{\pi}{4}+\theta))^2 - \frac{1}{2}\sin(\varepsilon)\sin(2\omega t)\sin(\frac{\pi}{2}+2\theta) d\tau. \tag{5.21}$$

Neglecting second order terms i.e. $sin^2(\varepsilon) = 0$

$$I_A \propto \frac{E_\circ^2}{2\tau}\int_0^\tau \frac{1}{2}(1+\cos(2\omega t))\cos^2(\frac{\pi}{4}+\theta) - \frac{1}{2}\sin(\varepsilon)\sin(2\omega t)\sin(\frac{\pi}{2}+2\theta)d\tau. \quad (5.22)$$

$$I_A \propto \frac{E_\circ^2}{4}\cos^2(\frac{\pi}{4}+\theta). \quad (5.23)$$

Since $\theta \ll 1$

$$I_A \propto \frac{E_\circ^2}{4}(\frac{\cos\theta}{\sqrt{2}} - \frac{\sin\theta}{\sqrt{2}})^2. \quad (5.24)$$

$$I_A \propto \frac{E_\circ^2}{4}(\frac{1}{2} - \frac{1}{2}\sin(2\theta)). \quad (5.25)$$

In the same way, the beam intensity at the second photodiode

$$I_B \propto \frac{E_\circ^2}{4}\sin^2(\frac{\pi}{4}+\theta). \quad (5.26)$$

$$I_B \propto \frac{E_\circ^2}{4}(\frac{1}{2} + \frac{1}{2}\sin(2\theta)). \quad (5.27)$$

The difference of the intensity signals generated at photodiodes A and B is

$$I_A - I_B \propto \frac{E_\circ^2}{4}(\frac{1}{2} - \frac{1}{2}\sin(2\theta)) - \frac{E_\circ^2}{4}(\frac{1}{2} + \frac{1}{2}\sin(2\theta)). \quad (5.28)$$

$$I_A - I_B \propto \frac{E_\circ^2}{4}\sin(2\theta). \quad (5.29)$$

since θ is small

$$I_A - I_B \, \alpha \, I_\circ\theta. \quad (5.30)$$

Equation 5.30 shows that the difference of the two photodiode signals is proportional to

both the optical rotation and the intensity, and independent of the ellipticity .

5.6. Time resolved pump probe technique

The availability of ultrafast laser sources allows us to excite a large number of phonons coherently, i.e the phonons are associated with one mode and have a constant phase relation. In a pump-probe measurement each pulse from the laser source is divided into two different intense ultrashort pulses called the pump pulse and the probe pulse. The pump pulse excites the sample and the probe pulse monitors the change in the sample. The intensity of the probe beam must be far lower than the intensity of the pump beam to avoid excitation of the sample by the probe pulse.

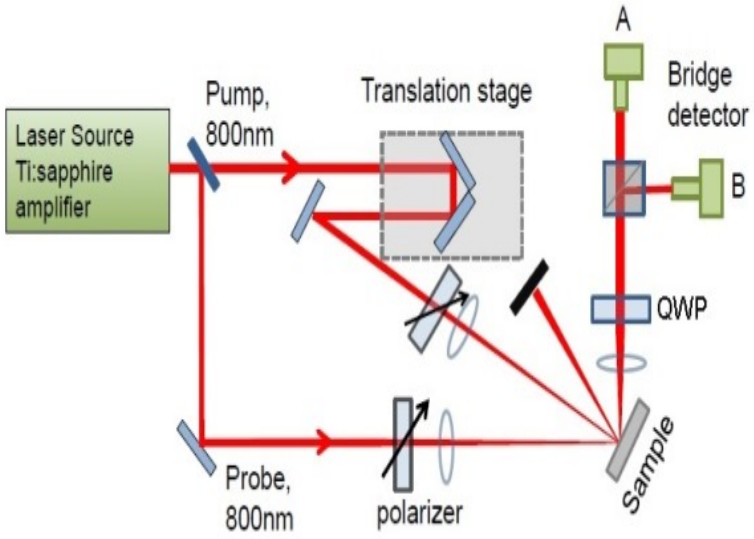

Figure 5.4.: Typical time resolved optical pump probe experimental arrangement

The experimental arrangement used in this study is shown in figure 5.4. The amplified ultrafast Ti:sapphire laser system consists of a Verdi V-18 pump, Mira seed oscillator and RegA-9050 amplifier, all manufactured by Coherent Inc. The coherent Verdi V 18 has continuous wave (CW) output of 532 nm wavelength and 18 W power. The 18 W beam is split with 6 W going to pump the Mira seed Ti:sapphire laser and 12 W going to the regA amplifier. The Mira seed produces ultrashort pulses of 800 nm wavelength and 45 fs duration at a repetition rate of 80 MHz. The Mira mode-locked power is around 500 mW corresponding to a pulse energy of 6 nJ. The pulses inside the Mira have high

peak power which can damage the RegA amplifier cavity. Therefore to avoid damage a stretcher/compressor system is used to chirp and temporally stretch the pulses that come from the Mira. The pulse duration of the stretcher pulse is more than 100 ps which can safely enter the RegA amplifier. The RegA amplifies the pulses energy from nJ to μJ. The repetition rate and the average power of the RegA amplifier are 250 KHz and 750 mW respectively. The stretched amplified pulses from the RegA amplifier are sent to the compressor in the stretcher/compressor to correct the chirp and recompress the pulses to produce ultrashort pulses. The resultant pulses have average power of more than 600 mW and pulse duration less than 60 fs.

The output beam was separated by a beamsplitter into two beams with wavelength of 800 nm. The pump and probe beams are focused to overlap at the sample. The arrival time of the pump beam is delayed by a retroreflector mirror fixed in translation stage in the pump beam path. The probe beam was s-polarized while the pump beam is linearly polarized at an angle that can be varied continuously by using a polarizer. The polarizers in the pump and probe beams paths were fixed close to the sample to avoid the polarizing effects of other optical components. To insure an area with uniform temperature is sampled the probe spot was centered with a pump beam of three times greater diameter. The CCD beam profiler is used to measure, overlap and focused the spots of both beams. A CCD camera was used to monitor the overlap of the pump and probe spots at the sample surface after removing the beam profiler. An optical chopper is used in the pump beam path to modulate its intensity at a frequency of 690 Hz. To measure the changes in ellipticity signal a quarter wave plate is located after the sample with its fast axis parallel to one of the major axes of the polarisation ellipse. The reflected probe beam was passed to an optical bridge detector which has a beamsplitter and two photodiodes. The beamsplitter separated the reflected probe beam into orthogonal linearly polarized p and s components. Inside the bridge detector the intensity of these beams was recorded by two photodiodes and an electronic circuit was used to determine the sum and difference signals. The alignment of the bridge detector is adjusted so that the reflected probe beam from the sample is normally incident on the front face of the beamsplitter. The intensity is equally divided between the two

photodiodes (or s and p polarisation modes) by rotating around the axis defined by the laser beam so as to null the difference between the intensity of these beams. To achieve this, the bridge detector is tilted at $45°$to the plane of incidence. The sum and difference of the beams intensities give the reflectance and the ellipticity (with the $\lambda/4$ plate inserted) signals respectively. Two lock in amplifiers are used to extract the reflectance and ellipticity signals.

The pump beam could induce a change in the diagonal reflection coefficients (r_{ss} and r_{pp}) leading to what is known as "reflectivity breakthrough" in the rotation and ellipticity signals when the probe polarisation is not precisely s or p polarized. To avoid the appearance of the reflectivity breakthrough in the ellipticity signal, the alignment of the bridge detector and the probe beam must be precise. Therefore the probe polarisation must be changed gradually and after each change the bridge detector should be realigned so that the difference of the photodiode intensities is equal to zero.

5.7. Optical bridge detector

The optical bridge detector is used to measure the transient rotation ellipticity and reflectivity signals. It is comprised of a polarizing cube beamsplitter of the Glan-Thompson type and two photo-diodes. The beamsplitter is made from birefringent calcite material and divides the reflected probe beam into two orthogonal linearly polarized (s and p polarisation) beams separated by an angle of 45 degrees as in figure 5.3 . The angular separation of these two beams is independent of the wavelength of the incident beam. The silicon photo-diode detectors (A and B) receive these two beams and measure their intensity. The photo-diodes connect to an electronic circuit that gives (A + B) and (A-B) outputs. The intensities of both beams recorded by the photo-diodes, A and B, should be approximately equal i.e. (A-B) output is zero. The (A+B) channel measures the total intensity of the reflected probe beam, and so is sensitive to any change in the reflectivity of the sample. The (A-B) channel is sensitive to any change in the polarisation of the reflected probe beam and therefore measures the transient rotation signal of the incoming beam.

5.8. Lock in amplifier

Each output channel of the optical bridge detector is connected to a lock in amplifier in order to filter out background noise, which interferes with the transient rotation and reflectivity signals. Two lock-in amplifiers of model 7265DSP from Signal Recovery (AMETEK) were used to record these two signals. This model of lock in amplifier uses a phase sensitive detection technique to extract the amplitude and phase of the signal at a specific reference frequency.

The operation of the lock-in amplifier is very simple and involves one sinusoidal input signal and one square reference signal:

Suppose the input signal has the form

$$V(t) = V_\circ \sin(\omega t + \phi)$$

while the reference signal has the form

$$V_R(t) = \sin(\Omega t)$$

The product of these two signals is

$$V(t)V_R(t) = \frac{V_\circ}{2}\left\{\cos\left[(\omega - \Omega)t + \phi\right] - \cos\left[(\omega + \Omega)t + \phi\right]\right\}$$

If $\omega \neq \Omega$ the product oscillates in time with an average value of zero. However if $\omega = \Omega$ the product contains a DC component.

Figure 5.5 shows a block diagram of a lock in amplifier. The input signal passes through a capacitor and then into the input amplifier, while the reference signal passes through a phase shifter. The two resulting signals are multiplied by passing through a mixer. The output is then passed through a low pass filter which removes the $2\Omega t$ component, leaving the DC component as the output of the lock-in amplifier. Within this thesis a mechanical chopper (MC1000 chopper) from Thorlabs was used to modulate the pump beam and provide a reference signal, both at a frequency of 690 Hz.

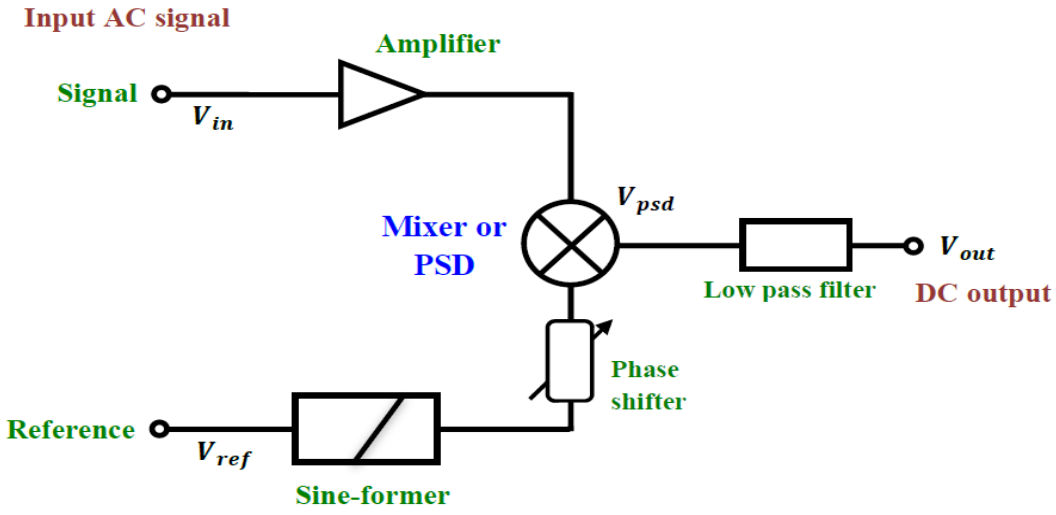

Figure 5.5.: Lock in amplifier diagram [12]

5.9. Delay line stage

An optical delay line translation stage IMS-CCHA from Newport Corp was used in the experiment to delay the pump pulse with respect to the probe pulse. The resolution of this translation stage is 0.1 μm which gave a temporal resolution of 6.67 fs. The stage has maximum travel distance of 600 mm. A hollow corner cube retroreflector was used with this stage to provide a maximum delay length of 1200mm, equivalent to 4ns of time delay.

5.10. Beam profiler

In time resolved measurements, the fluence of the probe beam should be smaller than the fluence of the pump beam and the probe spot size should be smaller than the pump spot size.

In order to have small spot size, the focal length (f) of the focusing lens or/and the divergence of the beam (θ) should be small so that the spot diameter

$$d = f\theta. \tag{5.31}$$

is also small. In this experiment the pump and probe beams pass through telescopes to reduce their divergence. The pump beam passes through a final lens with focal length of 25cm while the probe beam passes through a lens of focal length 6.3 cm before being focused on the sample. This gives only an estimate of the spot size, so it is necessary to accurately determine the spot sizes and to monitor their overlap.

The CCD beam profiler is used to measure the pump and probe spots sizes and achieve the ideal overlap. The CCD beam profiler used in this experiment is a DataRay WinCAM UCD12, with a 6.3 $\times$4.8 mm^2 CCD with pixel size of 4.6 μm. The beam profiler is fixed at the overlap position of the pump and probe beams. The beam profiler software can be used to show the overlap of the beams. Moving the probe lens forward or away from the beam profiler can minimize the spot size of the probe beam. The pump lens, with a larger focal length than the probe lens, can be used to overlap the beams by moving it up or down and from side to side.

5.11. Fitting of the time resolved ellipticity signal

The time resolved signal contains a variety of features resulting from different physical phenomena, which have different characteristic time scales. For example, the characteristic time of interaction between light and electrons is different to that for the interaction between the light and the lattice. A typical time resolved ellipticity signals obtained from InAs sample and two $Ge_2Sb_2Te_5$ samples can be divided into three regions with respect to the delay time t_d between pump and probe. The first region is when $t_d < 0$ and the probe pulse reaches the sample before the pump pulse. In this region the reflected probe beam does not record any change in the sample response. The second region appears around $t_d = 0$ when pump and probe beams have similar optical path length and overlap in time at the sample. Within this region a large peak is seen in the transient polarisation signal due to the specular optical Kerr effect within the sample. The last region occurs for $t_d > 0$ when the pump beam arrives at the sample before the probe beam. In this region the reflected probe beam carries information about the changes that occur in the sample due to excitation by the pump beam, which causes a finite change in the probe

polarisation. Typically in this region an oscillatory component associated with a coherent optical phonon is superimposed upon an exponential background.

As a consequence, the ellipticity signal can generally be fitted by an equation containing a Gaussian function, an exponentially damped oscillatory function and a simple exponential decay term. Assuming that both the pump and probe beam have Gaussian shape, the intensity of the pump beam can be written as [100]

$$I_{(t)} \propto \frac{1}{\sqrt{2\pi w}} \exp\left(\frac{-t_d^2}{2w^2}\right)$$

The ellipticity signal as a function of time delay is calculated as a double convolution of the Gaussian pump and probe beams with the system response. Calculating the convolution integral we obtain for the ellipticity signal:

$$\begin{aligned} S \propto A\exp\left(-\tfrac{(t-t_\circ)^2}{4w^2}\right) + \tfrac{B}{2}\exp\left(\tfrac{w^2}{t_1^2} - \tfrac{t-t_\circ}{t_1}\right)\left[1-\operatorname{erf}\left(\tfrac{w}{t_1} - \tfrac{t-t_\circ}{2w}\right)\right] \\ + \sum \tfrac{C_i}{2}\exp\left(-\tfrac{t-t_\circ}{t_{2i}}\right)\left[1+\operatorname{erf}\left(\tfrac{t-t_\circ}{2w}\right)\right].\cos\left[2\pi f_i(t-t_\circ) + 2\pi\beta_i(t-t_\circ)^2 + \phi_i\right] \end{aligned} \tag{5.32}$$

where A is the Gaussian peak amplitude, $t_\circ$ is zero delay position, t is the time, w is the width of the optical pulse, B is the amplitude of the simple exponential decay, t_1 is the relaxation time for the simple exponential decay, erf is the Gaussian error function, C_i is amplitude of the damped oscillatory response, f_i is frequency of oscillation, t_{2i} is damping time of the oscillation, β_i is a chirp parameter, and ϕ_i is the initial phase of the cosine oscillation. The first term in equation 5.32 represents the instantaneous incoherent sample response and is used to fit the SOKE peak within the ellipticity signal. The second term represents a relaxation process with relaxation time t_1 and is used to fit the exponential background within the signal. The last term represents the damped oscillatory response of a phonon mode to the Gaussian impulse with relaxation time t_2. The chirp parameter is included in the cosine function to describe any changes in the phonon frequency with time due to changes in the temperature. An offset signal that sometimes occurs at negative time delay has been taken into account. A constant has been included in the fitting function to describe the an offset that may arise from other

background signals such as diffuse pump scatter, or because the repetition rate is high and the system could not fully relax before the next pulse arrives.

The time resolved ellipticity signal contains the SOKE peak and weak oscillations, therefore it was difficult to fit all components of the signal at the same time. For this reason just the exponential decay and oscillatory components were fitted by using just the second and the third terms of equations 5.32. In the third term two oscillatory components ($i = 1, 2$) were required to fit the data.

The process of fitting the ellipticity signal that has chirp in the oscillations was done in two steps so as to be able to describe the change in the phonon frequency with time. Firstly, the raw time resolved data was fitted by using the second and the third terms of equation 5.32. Then the oscillatory signal components were isolated by subtracting the fitted exponential relaxation background. The chirp parameter β and the zero delay $t_\circ$ were fixed at 0 and the pulse width was fixed at $10^{-4}ns$. In the third term two oscillatory components were used to fit two oscillations, one in the THz regime and the other in GHz regime. Then the frequency of the oscillatory residual was extracted from a fast Fourier transformation (FFT). A Lorentzian curve was used to fit the peak in the FFT. Secondly, the oscillatory residual was fitted by using the second and third terms in 5.32. In the third term one oscillatory component was used to fit the THz frequency oscillation. The initial frequency values were set equal to those obtained from the FFT and the chirp parameter was allowed to vary so as to determine any change in the phonon frequency with time.

The Lorentz equation used to fit the peak in the FFTs peak had the form

$$y = y_\circ + \left(\frac{2\mathrm{A}}{\pi}\right)\left[\frac{\mathrm{w}}{4(x - x_c)^2 + \mathrm{w}^2}\right]$$

where $y_\circ$ is the y value offset, A is the area under the curve, w is the full width of the peak at half height, and x_c is the centre frequency of the peak.

The ellipticity signal of the InAs (111) wafer did not exhibit any clear chirp, therefore the fitting process involved just the first step used in fitting the ellipticity signal of GST/InAs (111).

5.12. Summary

In this chapter I have described the pump and probe experiment setup for generating and detecting coherent optical phonons. In addition the process of fitting the ellipticity signal was explained.

6. Observation of coherent optical phonons in a InAs(111) wafer

In this chapter I will present time resolved optical pump-probe measurements that provide information about the amplitude, phase, frequency and relaxation of coherent optical phonons in a InAs(111) wafer. The pump-probe technique employed to perform time resolved transient reflectivity (R) and ellipticity which is the imaginery part of the Anisotropic Reflectance (AR), measurements will be described. I will also present measurements that show how the response of the InAs sample depends upon the pump polarisation, sample orientation and pump fluence. The results are interpreted by using a theory of transient stimulated Raman scattering (TSRS) that can account for the excitation of a phonon by either impulsive stimulated Raman scattering or the effect of an optically induced space charge (SSC) field.

6.1. Ultrafast pump-probe measurements.

The limited time resolution of optical detectors largely prevents ultrafast processes from being observed directly. One solution is to use a streak camera, which transforms the temporal intensity profile of a light pulse into a spatial profile on the display of the detector. To resolve the dynamics of ultrafast phenomena such as the excitation and damping of optical phonons, several data points must be recorded within each period of the phonon oscillation. Due to its limited temporal resolution, this cannot be accomplished with a streak camera.

A way to solve this problem is to measure the optical properties using the pump-probe

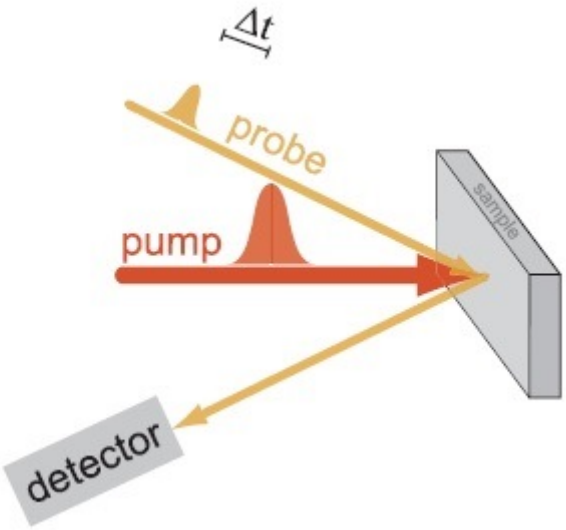

Figure 6.1.: Schematic of pump-probe technique[26]

technique, which is explained in figure 6.1. A first laser pulse, called the pump, induces a dynamic process that changes the optical properties of the sample. A second laser pulse, called the probe, arrives after a certain time at the excited area. The reflected probe pulse is passed into a detector to measure the changes in the optical properties. The intensity of the probe pulse needs to be far lower than the intensity of the pump pulse to avoid excitation of the sample by the probe pulse. In this configuration the duration of the probe pulse is what limits the time resolution .

6.2. Measuring transient reflectivity and ellipticity signals

Understanding of phonon spectra can provide information about the crystallographic structure of a material. Time resolved pump-probe measurements can offer information about fast relaxation of photo-excited carriers and the phase and amplitude of coherent optical phonons [43, 7]. Increasing the pump intensity, and hence the amplitude of the coherent optical phonons within the material, can in principle lead to a change in the phase of the material. The symmetry of a particular coherent optical phonon can be studied by changing the polarisation of the pump and probe relative to the crystallographic axes. The time resolved transient R and ellipticity of InAs (111) wafer have

been measured. The time resolved measurements were performed in three different sets in order to study the dependence of the coherent optical phonons upon one parameter while the others were fixed. The first measurement was performed by changing the pump polarisation while the probe polarisation was fixed at s polarisation. The second measurement was performed by changing the sample orientation while the difference between the pump and probe polarisation was fixed at 45°. The last measurement was performed by varying the pump fluence.

6.3. Experimental details of optical pump probe measurements

Time resolved transient R and ellipticity measurements were performed on the (111) orientation of the InAs sample. The measurements were made using a single colour optical pump-probe technique. A pulsed laser beam with 800 nm wavelength and 45 fs duration was generated by a 100 kHz Ti:sapphire regenerative amplifier and divided into pump and probe beams. The sample was pumped at near to normal incidence by the pump beam with variable polarisation state and fluence of 1.06 $\mathrm{mJ/cm^2}$. The pump beam induced transient changes in the R and ellipticity signals that were detected by an s-polarized probe beam. The probe beam was incident at 45° to the sample normal with a much weaker fluence of 0.018 $\mathrm{mJ/cm^2}$. The pump and probe were focused so as to overlap on the sample. Focusing lenses fixed on three axes translation stages were used to adjust the overlap of the spots as they were viewed with a high magnification CCD camera. The sizes of the pump and probe spots measured by a beam profiler were 121 μm×128 μm and 43 μm×49 μm respectively. The pump beam intensity was modulated at 690 Hz by a mechanical chopper. The reflected probe beam was incident upon an optical bridge detector connected to two lock in amplifiers to detect the transient reflectivity and ellipticity signals. The alignment of the probe beam and the bridge detector should be precise in order to avoid the breakthrough of the transient reflectivity into the ellipticity signal. The sample was fixed on a tripod platform that has three bolts to adjust the alignment of the sample so that the direction of the reflected

probe beam does not change as the sample is rotated about its normal .

6.4. Experimental results

6.4.1. Changing the pump polarisation

Time resolved transient R and ellipticity measurements were performed on an InAs(111) wafer of 350 μm thickness. To investigate the dependence of the time resolved transient R and ellipticity signals upon the pump polarisation, the applied pump beam was incident nearly normal to the sample while the s- polarized probe beam was incident at 45° as shown in figure 6.2. The p-polarisation state of the pump beam, with the direction of the pump polarisation parallel to the plane of the incidence, was defined as the 0° orientation. The polarisation state of the pump beam was varied through 180° in 10° steps starting from p-polarisation.

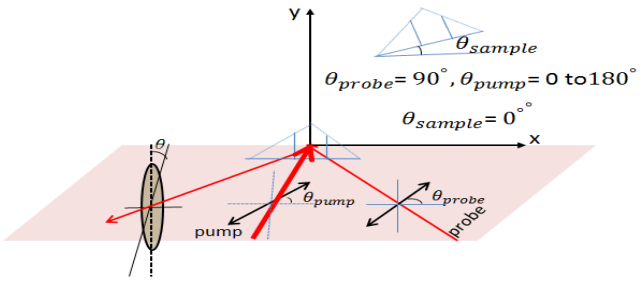

Figure 6.2.: Experimental geometry for study of the response of the InAs sample to the changing pump polaraization

Figure 6.3 shows a typical transient R signal obtained from the InAs(111) wafer, with an s-polarized probe beam and for different pump polarisations. Figure 6.3 (a) shows the transient reflectivity with the pump polarized at 45° relative to the probe. The initial rise of the signal occurs within about 150 fs and is associated with the photo-excitation and thermalization of an electron- hole plasma. Weak oscillations are observed within the signal. The transient R signal is independent of the pump polarisation except in the region where the pump and probe overlap in time for which bleaching of the optical transition may occur.

Figure 6.4 (a) presents a typical time resolved ellipticity signal obtained from the InAs(111)

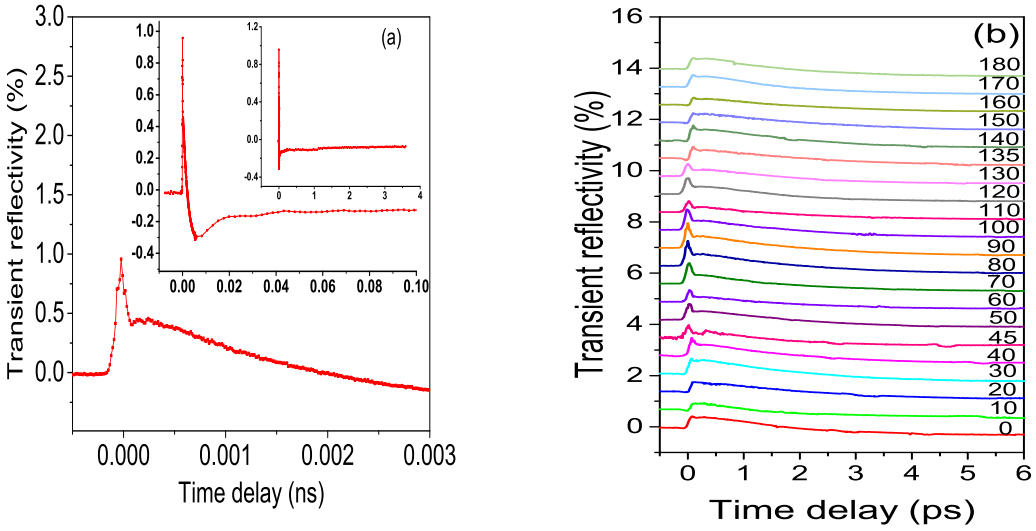

Figure 6.3.: Time resolved R signals obtained from a InAs (111) wafer. The pump beam was applied normal to the sample while the probe beam was s-polarized and incident at $45°$. (a) Typical transient R signal, for $45°$ pump polarisation, plotted on different timescales. (b) Transient R signals for different pump polarisations.

wafer, for an s-polarized probe beam and with the pump polarisation set at $45°$ relative to the probe. Around zero time delay, where the pump and probe overlap in time, a large peak is observed due to the specular optical Kerr effect (SOKE). The SOKE peak is observed to have maximum amplitude when the pump and probe polarisations are set $45°$ apart. The SOKE peak is succeeded by many cycles of oscillation with relaxation time of around 3ps. The variation of the ellipticity signal with pump polarisation is shown in figure 6.4 (b). The oscillatory component obtained from the ellipticity signal is plotted in figure 6.4 (c). The experimental data has been cut immediately after the SOKE peak and fitted to equation 5.32, without subtracting a background, and with the chirp parameter set equal to zero. The power spectra obtained from this oscillatory component are shown in figure 6.4 (d) for different pump polarisations. The oscillation frequencies obtained both by fitting the power spectrum to a Lorentzian curve, and by fitting equation 5.32 to the time domain data before subtracting the background and with the chirp parameter set equal to zero, are shown in figure 6.5 (a). The frequencies obtained by the two methods are in good agreement, being approximately equal to 6.511±0.007 THz for FFT data and 6.495±0.005 THz for the raw time domain data and independent of pump polarisation. However figure 6.5 (b) shows that the phonon amplitude has a

definite dependence on pump polarisation that is suggestive of the SOKE, with the amplitude reaching maximum value when the pump and probe polarisations lie 45° apart. The dependence of phase upon pump polarisation is shown in figure 6.5 (c). The phase of oscillation changes by approximately π radians as the pump polarisation crosses 90°. The dependence of the line width and relaxation time upon pump polarisation is shown in figure 6.5 (d) and (e) respectively. Panel (e) shows a well defined variation of the relaxation time that is symmetric about the 90° orientation, with maximum relaxation time occuring at approximately 70 and 110°. The variation of the linewidth in (d) is less clear and is not consistent with the variation of the relaxation time shown in (e) for an unknown reason.

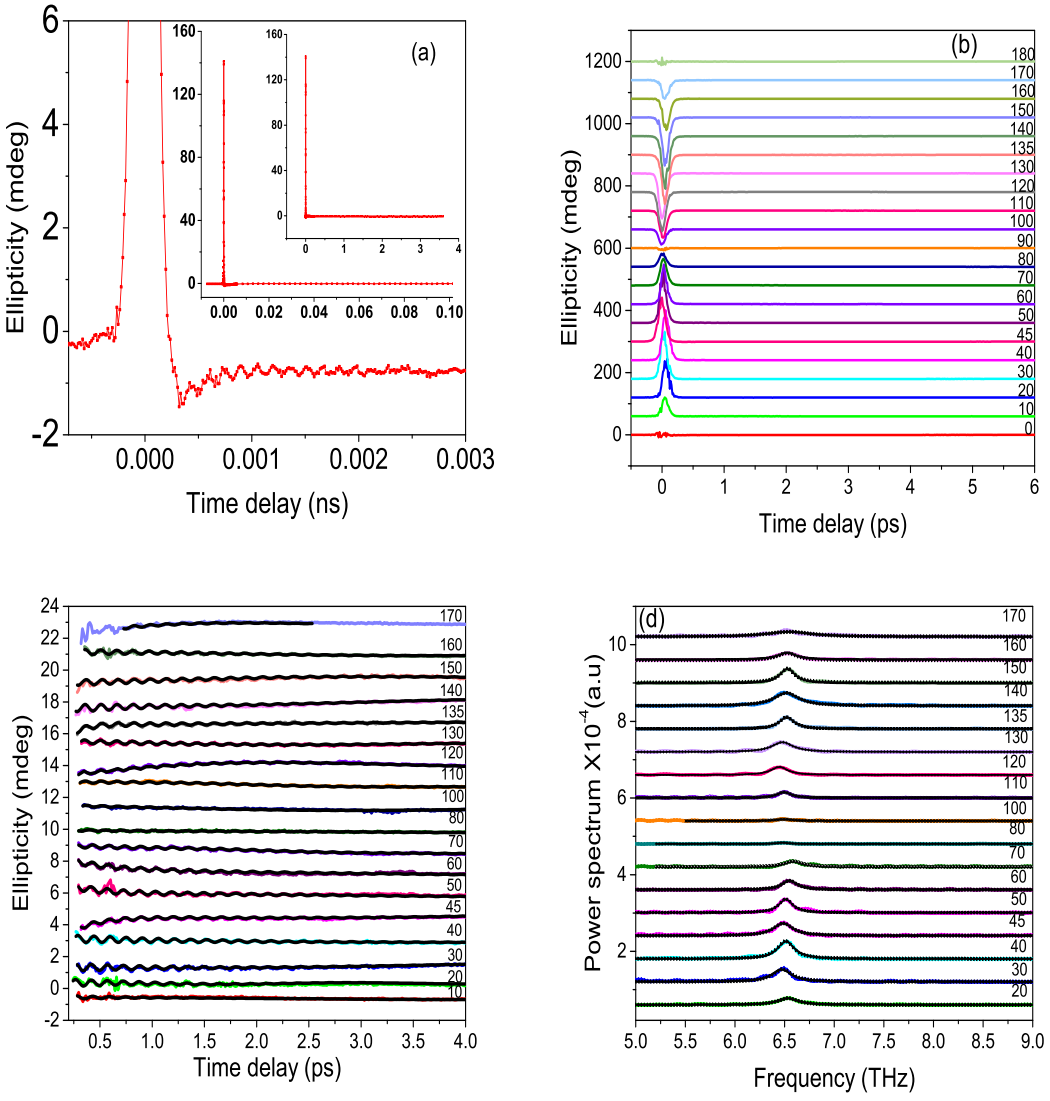

Figure 6.4.: Time resolved ellipticity signals obtained from the InAs(111) wafer. The pump beam was applied normal to the sample while the probe beam was s-polarized and incident at $45°$. (a) Typical ellipticity signal for $45°$ pump polarisation, plotted on different timescales. (b) Ellipticity signals for different pump polarisations. (c) Oscillatory component of ellipticity signal after subtracting the SOKE peak and fitting equation 5.32 to the time domain data. (d) Power spectra obtained from the oscillatory components of the ellipticity signals.

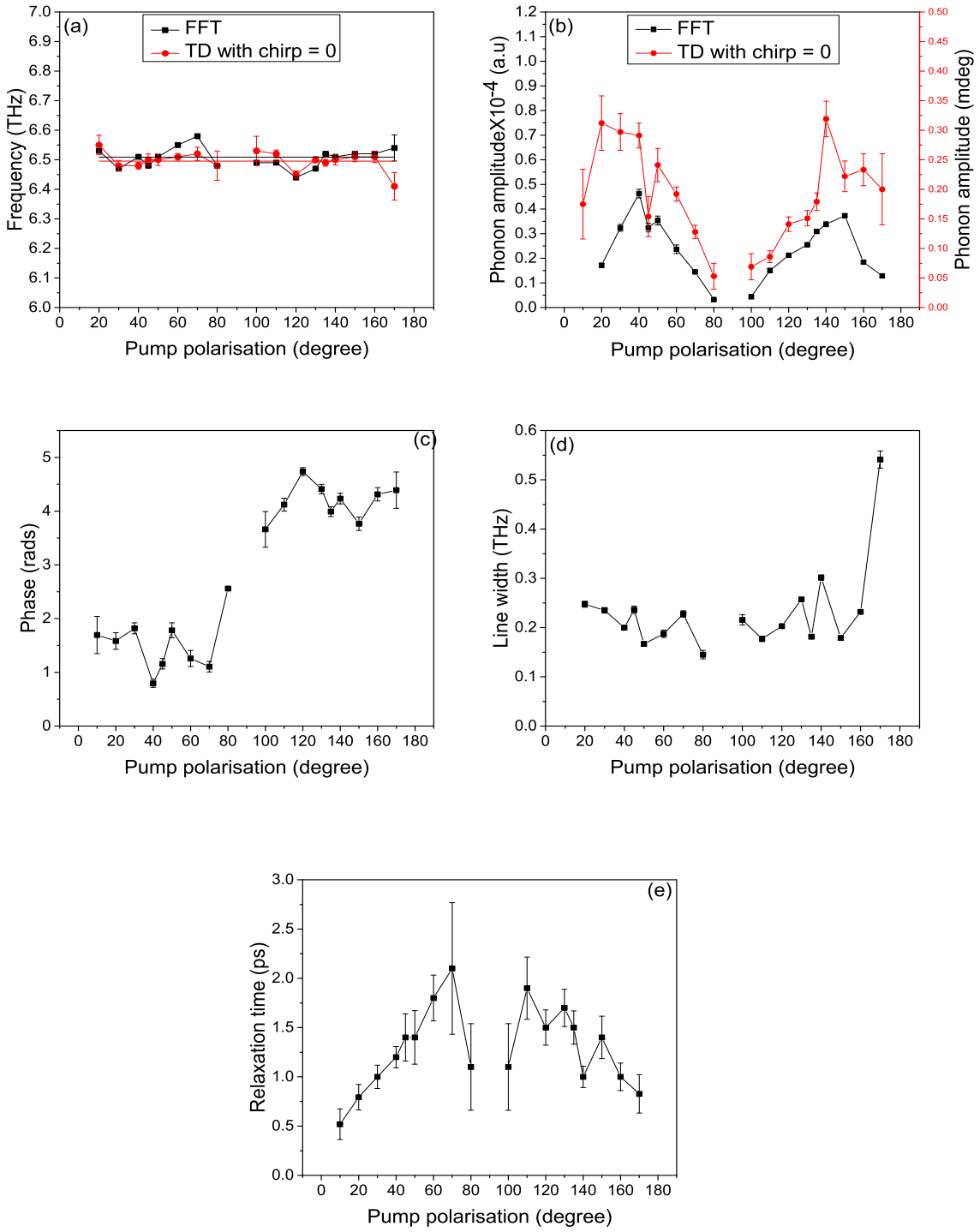

Figure 6.5.: The dependence of (a) frequency, (b) amplitude, (c) phase, (d) line width, (e) relaxation time, obtained from the ellipticity signal upon the pump polarisation is shown for measurements made on the InAs (111) wafer. The pump beam was incident normal to the sample while the probe beam was incident at 45° and s-polarized. In (a) each black square represents the frequency value obtained by fitting a Lorentzian to the power spectrum, and the red circles represent the frequency values obtained by fitting the data to equation 5.32, with the chirp parameter set equal to zero, before subtracting the background. In (b) the black circle represent the amplitude values obtained by fitting a Lorentzian lineshape to the power spectra, while the red circles represent the amplitude values obtained from fits to equation 5.32 before subtracting the background.

6.4.2. Changing the sample orientation

To study the dependence of the transient R and ellipticity signals upon the sample orientation, the pump polarisation was fixed at 45° while the probe polarisation was s polarised, and the sample was rotated about its normal from through 180° as shown in figure 6.6. The sample orientation θ_{sample} has been defined as the angle between the long sample edge and the plane of incidence.

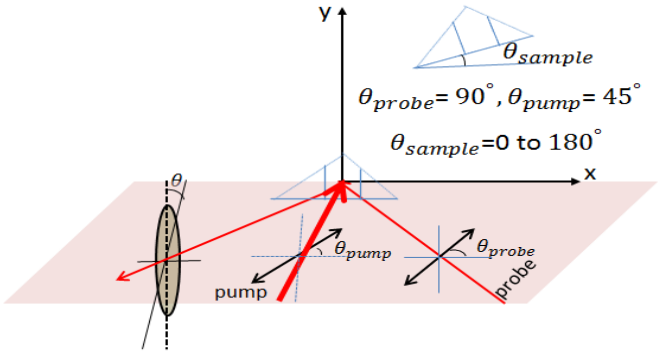

Figure 6.6.: Experimental geometry for study of the dependence of optical response upon orientation of the InAs(111) wafer.

Figure 6.7 (a) presents the dependence of the ellipticity signal on sample orientation when the polarisation of pump and probe were set 45° apart. The signal is dominated by the initial SOKE peak, the form of which appears to be independent of the sample orientation. The oscillatory component of the ellipticity signal is plotted in figure 6.7 (b), and appears to have similar phase for all sample orientations. The power spectra obtained from the oscillatory components of the ellipticity signal are shown in figure 6.7 (c). The phonon frequencies extracted from fitting both the power spectra and the time domain signals are plotted in figure 6.8 (a). The phonon frequency is seen to be equal to 6.493±0.002 THz for FFT data and 6.487±0.003 THz for the time domain data and independent of sample orientation. The dependence of the phonon amplitude on the sample orientation is plotted in figure 6.8 (b). Allowing for some scatter in the extracted values we can conclude that the phonon amplitude is independent of sample orientation. Figure 6.8 (c), (d) and (e) show the dependence of line width, relaxation time and phase of the oscillations on sample orientation. Again there is no systematic variation of any of these parameters, suggesting that their values are independent of sample orientation.

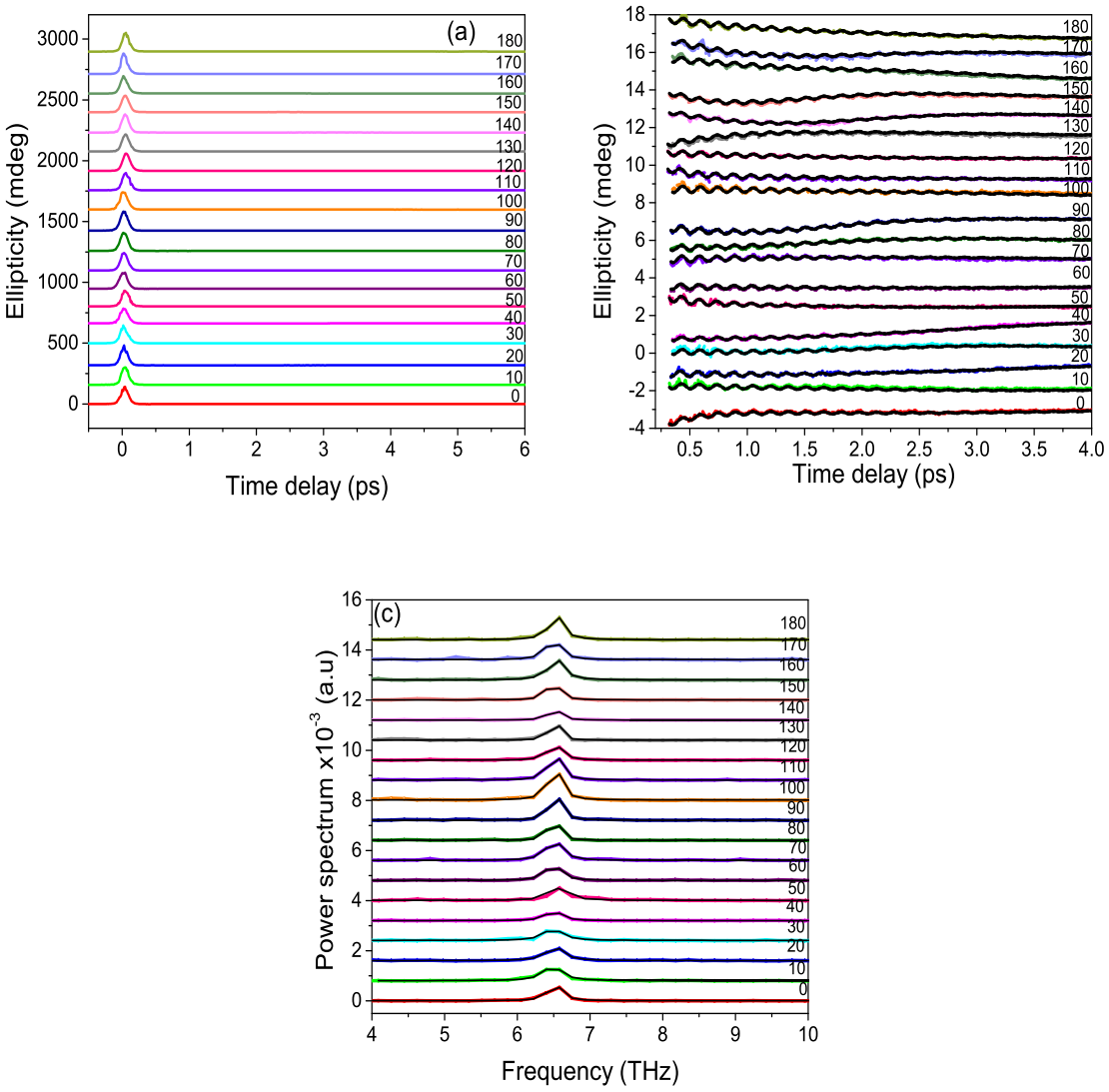

Figure 6.7.: Time resolved ellipticity signals obtained from the InAs (111) wafer as the sample was rotated from 0 to $180°$ about its normal direction. The pump beam was at close to normal incidence with polarisation angle of $45°$ while the probe beam was incident at $45°$ to the normal with s-polarisation. (a) Ellipticity signals for different sample orientations. (b) Oscillatory components of the ellipticity signal before background subtraction. (c) Power spectra obtained from the oscillatory components of the ellipticity signals.

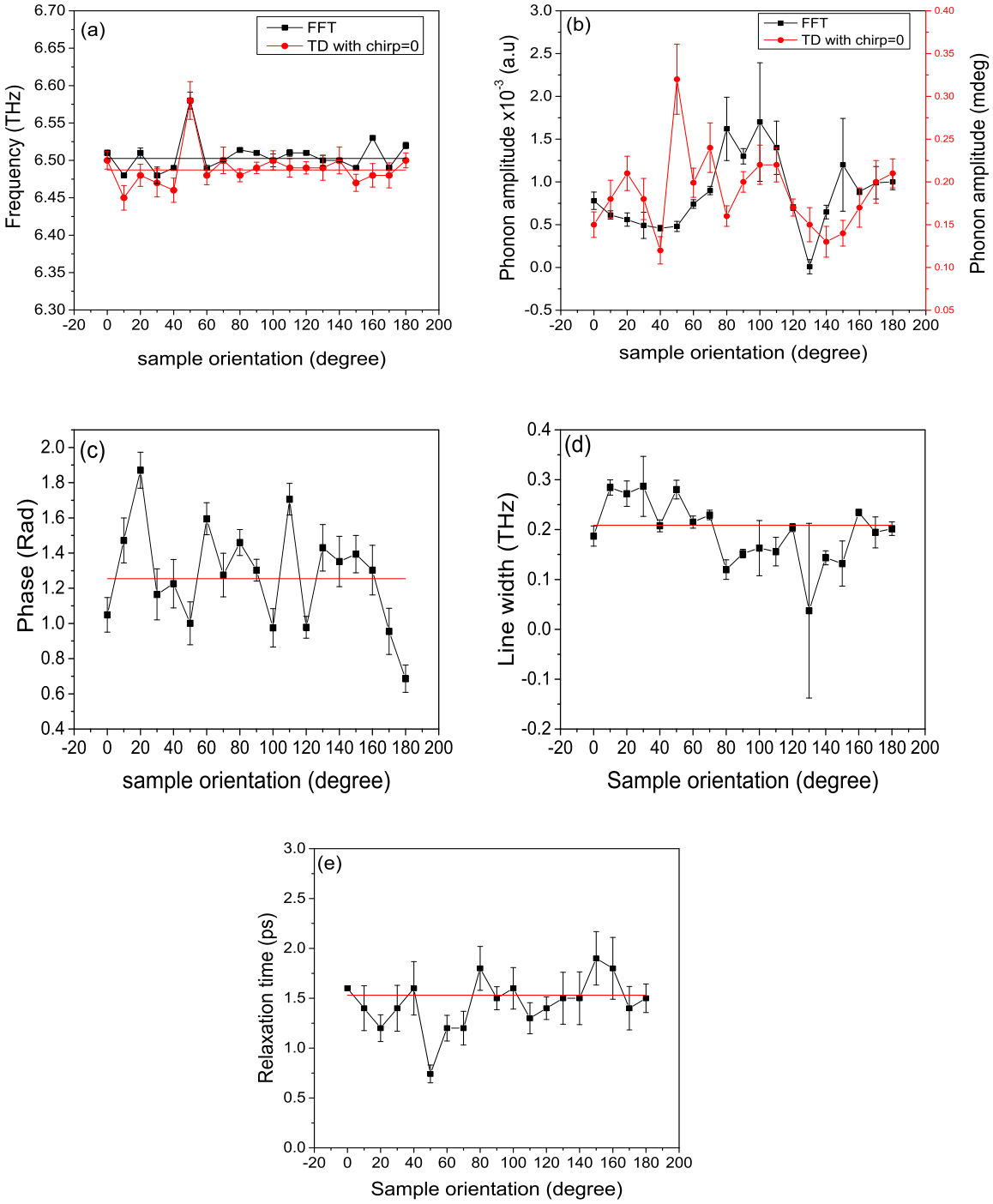

Figure 6.8.: The dependence of (a) frequency, (b) amplitude, (c) phase, (d) line width, and (e) relaxation time, upon the sample orientation are shown for measurements made upon the InAs (111) wafer. The pump beam was at close to normal incidence upon the sample with fixed polarisation angle of $45°$ while the probe was incident at $45°$ and s-polarized. In (a) the black squares represent the frequency values obtained by fitting a Lorentzian to the power spectrum, while the red circles represent the frequency values obtained from fitting equation 5.32 to the data before subtracting the background and with the chirp parameter set equal to zero. In (b) the black squares represent the amplitude values obtained from fitting a Lorentzian to the power spectrum while the red circles represent the amplitude values obtained from fitting equation 5.32 to the data before subtracting the background.

6.4.3. Changing pump fluence

The effect of pump fluence on the transient ellipticity and R signals and hence upon the COPs within InAs (111) was studied with the pump and probe polarisations set 45° apart as shown in figure 6.9. The measurements were made at high pump fluence and then immediately repeated at a lower fluence of 1.01 $\mathrm{mJ/cm^2}$.

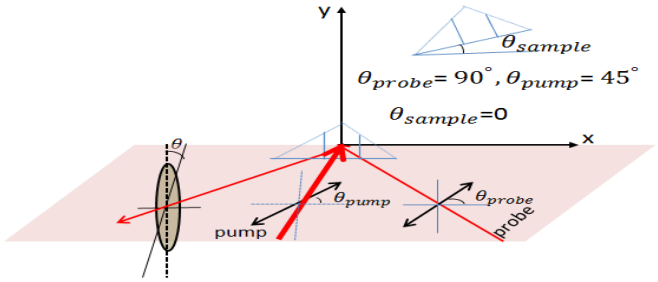

Figure 6.9.: Experimental geometry for study of the dependence of the optical response of the InAs sample upon pump fluence.

The transient ellipticity and R signals obtained from the repeated measurement at 1.01 $\mathrm{mJ/cm^2}$ are shown in figure 6.10 (a) and (b). The transient ellipticity and R signals obtained at the elevated pump fluence are shown in figure 6.11 (a) and (b). Figure 6.10 (c) and 6.11 (c) show the power spectra obtained from the ellipticity signals acquired during the repeated measurement at 1.01 $\mathrm{mJ/cm^2}$ and at the elevated pump fluence values respectively. The repeated measurements at low fluence suggest that the signal shape and oscillation frequency are unaffected by exposure to elevated pump fluence, which implies that no structural changes have taken place. This is consistent with InAs being a hard material with a high melting point . The peak height of the reflectivity signals obtained at elevated pump fluence increase up to a pump fluence of 5.05 $\mathrm{mJ/cm^2}$ and then decrease, indicating that there saturation of the absorption occurs at about 5.05 $\mathrm{mJ/cm^2}$.

After exposure to high fluence (measurement pump fluence = 1.01 $\mathrm{mJ/cm^2}$)

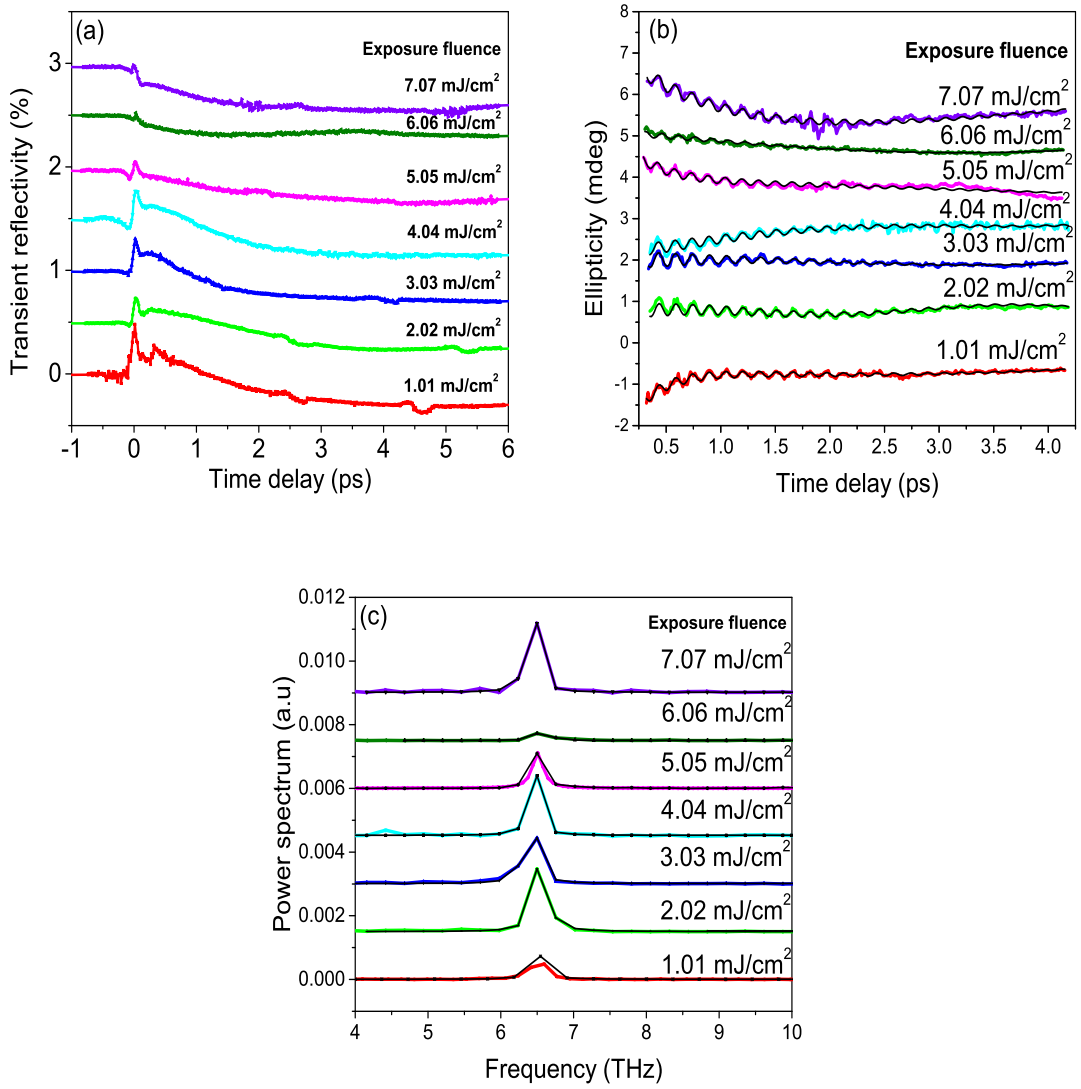

Figure 6.10.: The dependence of transient reflectivity and ellipticity signals obtained from InAs (111) wafer after exposure to elevated pump fluence when the pump and probe polarisations were set 45° apart. A measurement was made at high pump fluence then immediately repeated at a lower pump fluence of 1.01 $\mathrm{mJ/cm^2}$. (a) and (b) transient reflectivity and ellipticity signals respectively obtained from the repeated measurements at the lower pump fluence of 1.01 $\mathrm{mJ/cm^2}$ after exposure to the elevated fluence shown in the legend. (c) shows the power spectra obtained from the ellipticity signals obtained at pump fluence of 1.01 $\mathrm{mJ/cm^2}$.

The frequency and amplitude of oscillations observed in the ellipticity signals obtained from repeated scans at low pump fluence and at elevated fluence are presented in figure 6.12(a) and (b) and figure 6.13 (a) and (b) respectively. The plots confirm that the frequency of oscillation is independent of pump fluence. Surprisingly the amplitude of oscillation measured at elevated fluence seems to be only weakly dependent upon the

value of the fluence . Figure 6.12 (c), (d), (e) and figure 6.13 (c), (d), (e) show that the linewidth, and relaxation time and phase of the oscillations observed in the ellipticity signals are independent of fluence for both repeated scans at low pump fluence and scans at elevated pump fluence .

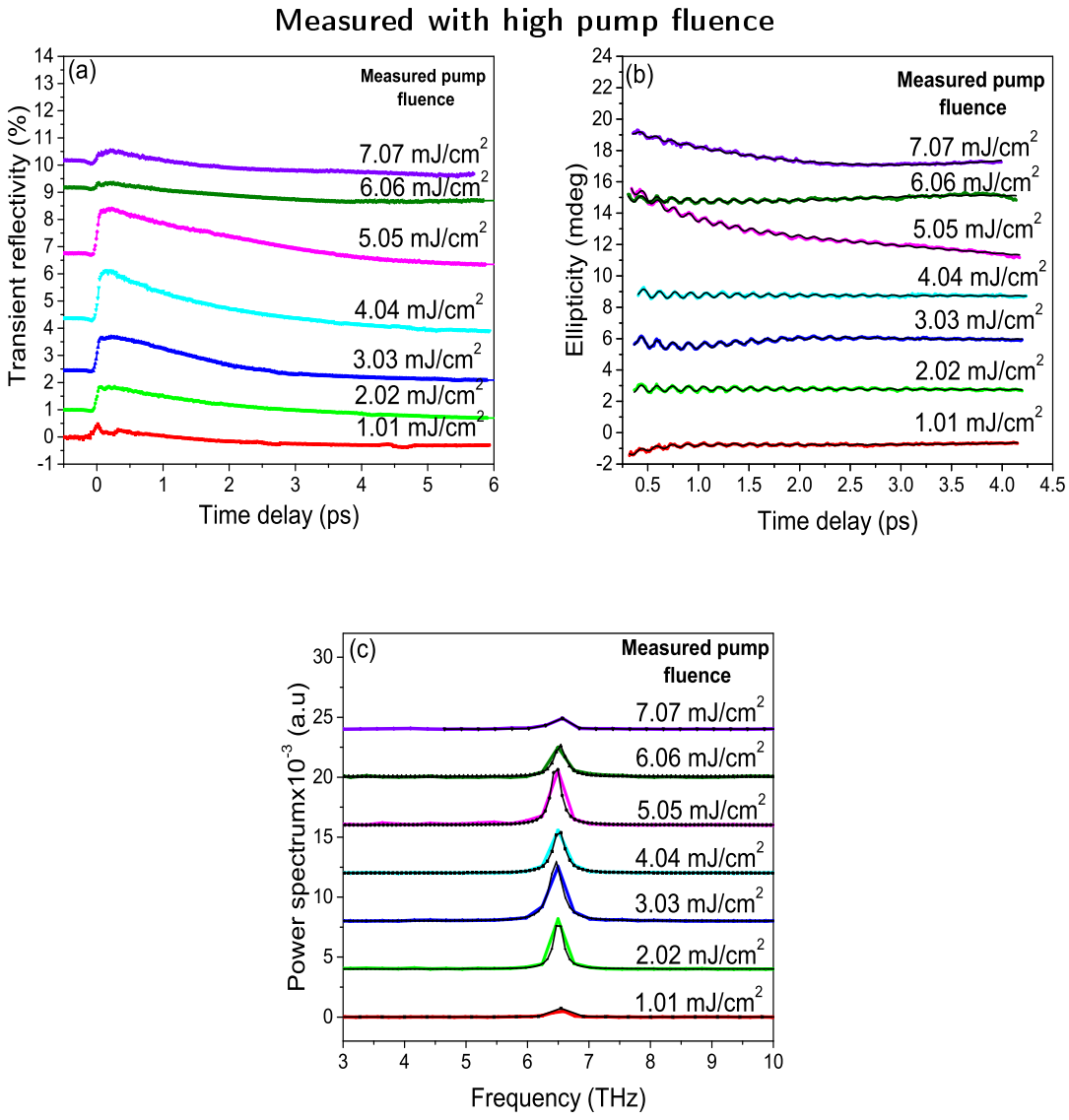

Figure 6.11.: The dependence of transient R and ellipticity signals obtained from InAs (111) wafer at elevated pump fluence when the pump and probe polarisations were set 45° apart. (a) and (b) transient R and ellipticity signals respectively obtained at elevated pump fluence. (c) shows the power spectra obtained from the ellipticity signals.

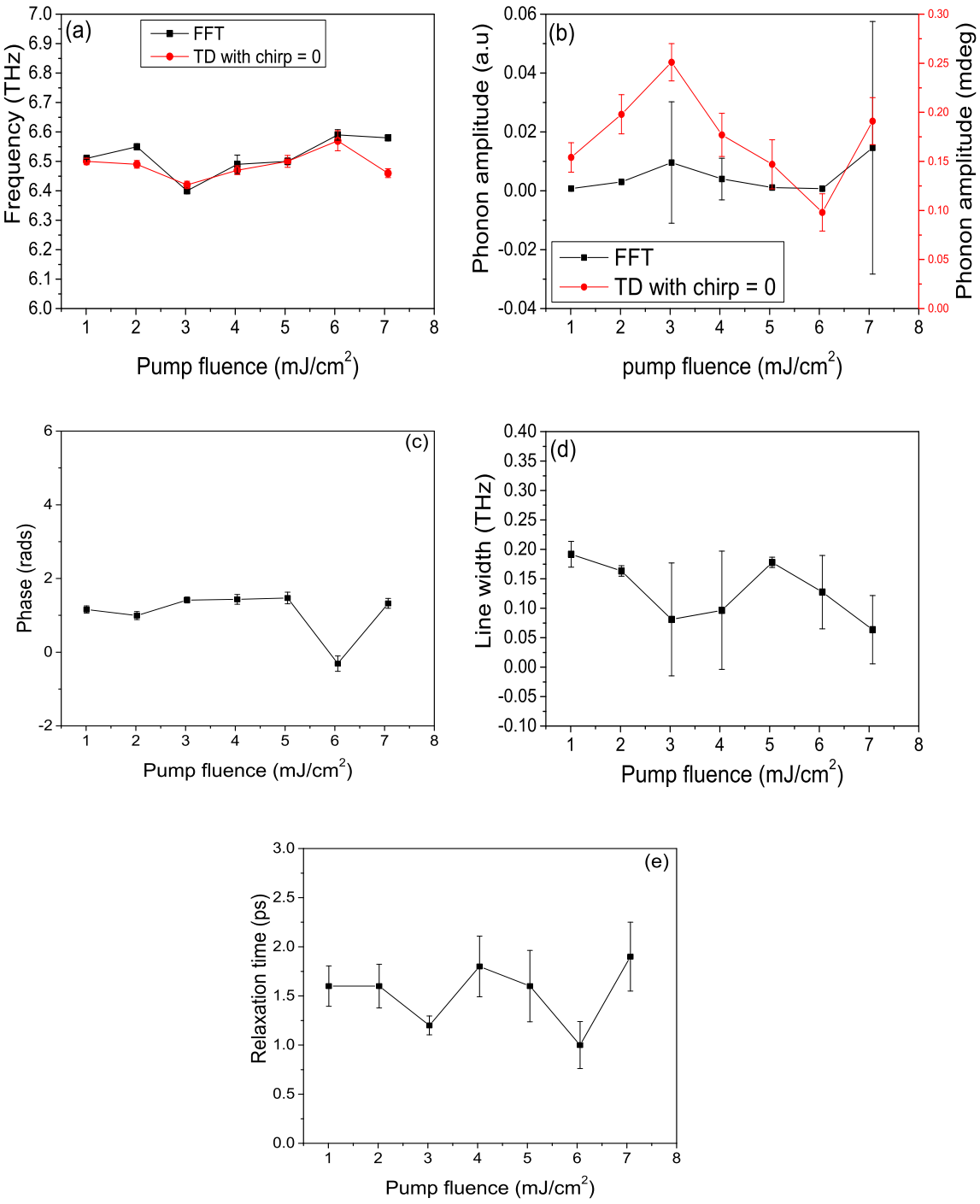

Figure 6.12.: (a) frequency, (b) amplitude, (c) phase, (d) line width, and (e) relaxation time of the phonon oscillation observed in the ellipticity signals obtained from InAs (111) wafer at pump fluence of 1.01 mJ/cm2 after exposure to the pump fluence used to label the horizontal axis. The pump beam was at close to normal incidence upon the sample with $45°$ polarisation angle while the probe was incident at $45°$ and s-polarized. In (a) the black squares represent the frequency values obtained by fitting a Lorentzian to the power spectrum, while the red circles represent the frequency values obtained by fitting equation 5.32 to the data before subtracting the background and with the chirp parameter set equal to zero. In (b) the black squares represent the phonon amplitude values obtained by fitting a Lorentzian to the power spectrum, while the red circles represent the phonon amplitude values obtained from fitting equation 5.32 to the data before subtracting the background and with the chirp parameter set equal to zero.

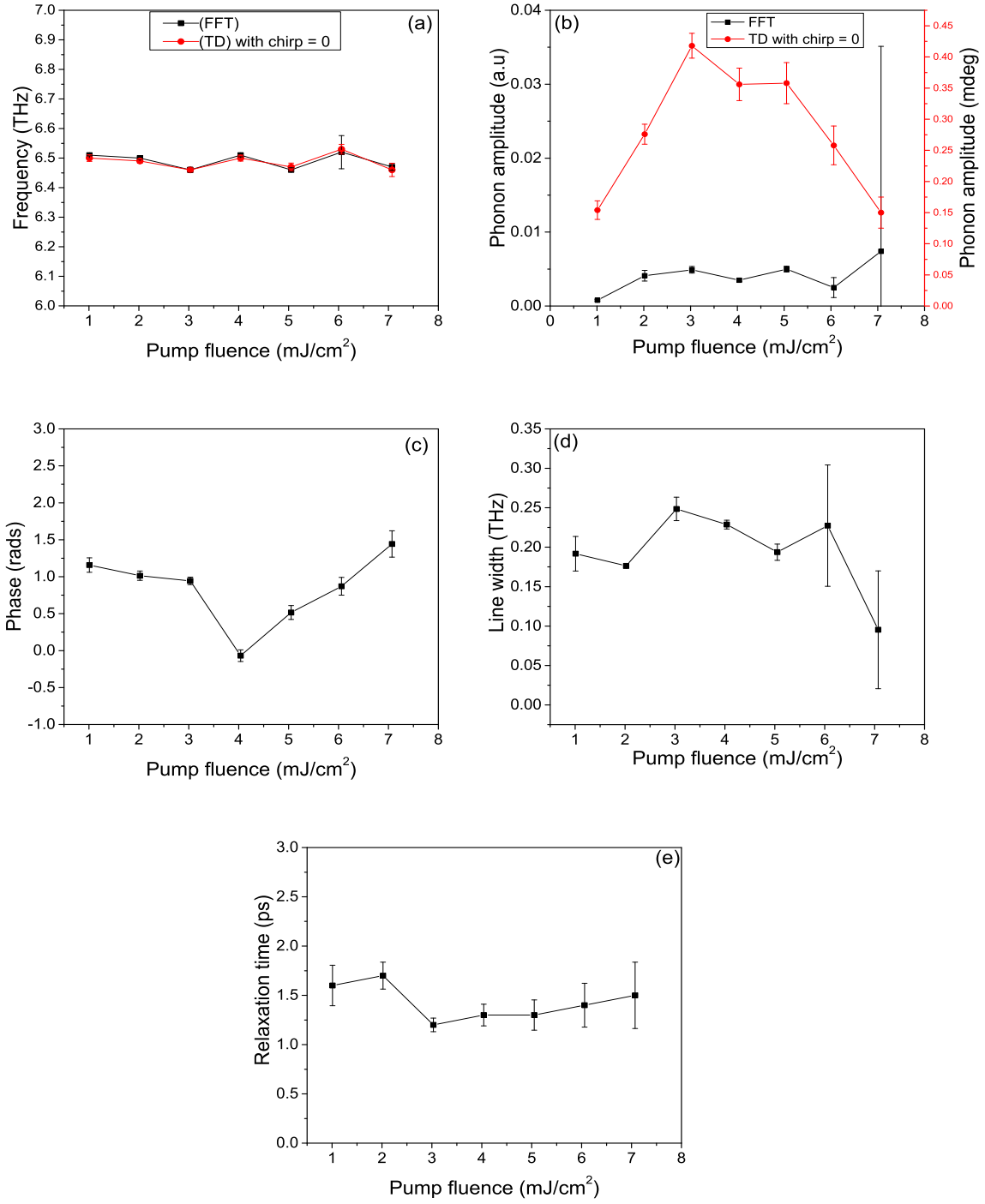

Figure 6.13.: (a) frequency, (b) amplitude, (c) phase, (d) line width, and (e) relaxation time of the phonon oscillation observed in the ellipticity signals obtained from the InAs (111) wafer at the elevated pump fluence used to label the horizontal axis. The pump beam was at close to normal incidence upon the sample with $45°$ polarisation angle while the probe was incident at $45°$ and s-polarized. In (a) the black squares represent the frequency values obtained by fitting a Lorentzian to the power spectrum, while the red circles represent the frequency values obtained from fitting equation 5.32 to the data before subtracting the background and with the chirp parameter set equal to zero. In (b) the black squares represent the phonon amplitude values obtained by fitting a Lorentzian to the power spectrum, while the red circles represent the phonon amplitude values obtained from fitting equation 5.32 to the data before subtracting the background and with the chirp parameter set equal to zero.

6.5. Raman spectra of the InAs (111) wafer

Micro-Raman measurements was performed on the InAs(111) wafer. Spectra were acquired with a Renishaw Raman System 1000 spectrometer equipped with a laser emitting light of 532nm wavelength. The laser beam was directed at normal incidence onto the sample and focused with a 40 $\times$ objective of 0.55 NA (numerical aperture) that yielded a spot with area <10 $\mu\mathrm{m}^2$. The reflected inelastically scattered light was directed onto a diffraction grating and from there onto the detector. An optical microscope was used to image the sample area being investigated with the Raman probe. For polarisation measurements a half-wave plate could be introduced into the incident beam path to change its polarisation. By introducing a polariser into the scattered light path, measurements with incident and scattered polarisation that were either parallel or perpendicular could be achieved. The intensity count of the inelastically scattered light was plotted against the wavenumber (cm^{-1}) . Before starting the measurements, a calibration measurement was performed upon a Si sample and the frequency of Si at around 520 cm^{-1} was observed.

The Raman spectrum of the InAs (111) wafer is shown in figure 6.14. The spectrum shows three peaks, one centred at about 216 cm^{-1} (6.5 THz) which can be associated with the zone center TO phonon, which is also detected in pump-probe measurements, and one centered at 234 cm^{-1} (7.0 THz) which can be associated with the zone center LO phonon. Beside the TO and LO phonon peaks there is another peak centered at 226 cm^{-1} (6.8 THz) which can be associated with the Fuchs-Kliewer surface optical phonon. The frequency of the Fuchs-Kliewer surface optical phonon mode [101] is related to the frequency of the bulk transverse optic TO (Γ), mode, and can be written as

$$\omega_{\mathrm{FK}} = \omega_{\mathrm{TO}}[(\varepsilon_\circ + 1)/(\varepsilon_\infty + 1)]^{1/2}$$

where $\varepsilon_\circ$ and ε_∞ are the static and high frequency dielectric constants respectively of the substrate material. Remembering the Lyddane-Sachs-Teller relation between the bulk TO and LO frequencies, namely $\omega_{\mathrm{LO}}^2/\omega_{\mathrm{TO}}^2 = \varepsilon_\circ/\varepsilon_\infty$, and noting that $\varepsilon_\circ > \varepsilon_\infty$, it can be seen that the Fuchs- Kliewer frequency should lie between the bulk TO and LO

frequencies: $\omega_{\mathrm{TO}} < \omega_{\mathrm{FK}} < \omega_{\mathrm{LO}}$ [102].

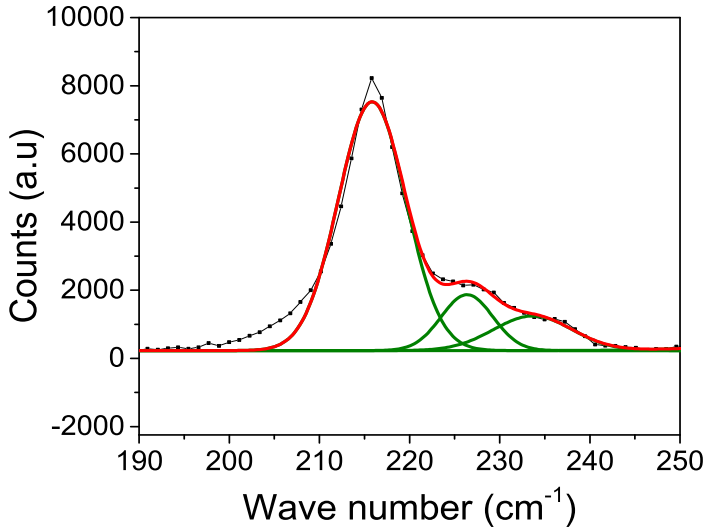

Figure 6.14.: Multipeak fitting of the Raman spectrum of the InAs(111) wafer

The mode frequencies observed in our Raman measurements are close to those found within the literature [103, 104, 105]. In previous Raman measurements [106] performed upon GaSb(001), a phonon with frequency of 6.7 THz was observed and associated with the zone center LO phonon. The observation of TO and LO phonons in InAs (111) and GaSb (001) are in agreement with the calculations of section (1.6.1) that consider the Raman selection rules for backscattering at normal incidence from the (111) and (001) surfaces of the zinc blend structure. The calculations reveal that for backscattering from the (100) surface only the LO phonon is Raman active, while for backscattering from the (111) plane both the LO and TO phonons are Raman active. The calculations also show that the LO phonon intensity is lower than the TO phonon intensity in agreement with our experimental measurements. Table (6.1) shows the phonon frequency of InAs(111) wafer that extracted from Raman and Pump-probe measurements.

Multi-peak fitting of the Raman spectrum was carried using the Origin software using the following procedure. First a baseline was removed from the spectrum, and then the peak centers were chosen manually using the peak analyzer preview function, before the multipeak fit tool was finally used to fit the peaks. The green lines represent the individual fitted peaks and the red line represents the superposition of all the individual modes as shown in figure 6.14.

Pump-probe measurement	Pump polarisation	Power spectrum
		6.511 ± 0.002 THz
		Time domain
		6.495 ± 0.005 THz
	Sample orientation	Power spectrum
		6.493 ± 0.002 THz
		Time domain
		6.487 ± 0.003 THz
Raman measurement	6.5 ± 0.003THz 6.8 ± 0.023 THz 7 ± 0.084 THz	

Table 6.1.: Frequency of phonon modes of InAs(111) wafer that extracted from the time resolved ellipticity signals and Raman measurement.

6.6. Discussion

A theory of transient stimulated Raman scattering (TSRS) was developed in chapter 3 in which the pump beam can excite COPs by either impulsive stimulated Raman scattering (ISRS) or by generation of a surface space charge (SSC). If we first confine the discussion to the ISRS mechanism, it was shown that for a (111) plane of a cubic crystal, A and E type phonons can be observed only in the R signal without any dependence on pump or probe polarization, while the T_2 phonon can be observed in both R and AR signals. Figure 6.15 shows the predicted dependence of the amplitude of the T_{2x}, T_{2y}, and T_{2z} modes upon pump and probe polarization. Each amplitude exhibits a sinusoidal dependence upon both θ (the angle between the pump electric field and the [1-10] axis) and ϕ (the angle between the probe electric field angle and the [1-10] axis) with period of 180° . Values of θ and ϕ that lead to zero amplitude should be avoided if a particular mode is to be observed within the experiment. The figure also shows that however the pump and probe are oriented, at least two of the three T_2 phonon modes should be excited and detected. The theory predicts what is allowed on grounds of symmetry but does not quantify the amplitude of the phonon signal.

Table 3.1 includes the expressions for the T_{2x}, T_{2y}, and T_{2z} modes for both the R and AR signals. Dropping the constant post-factors of $-2/3$ in the R and summing the three expressions yields a constant value as explained bellow.

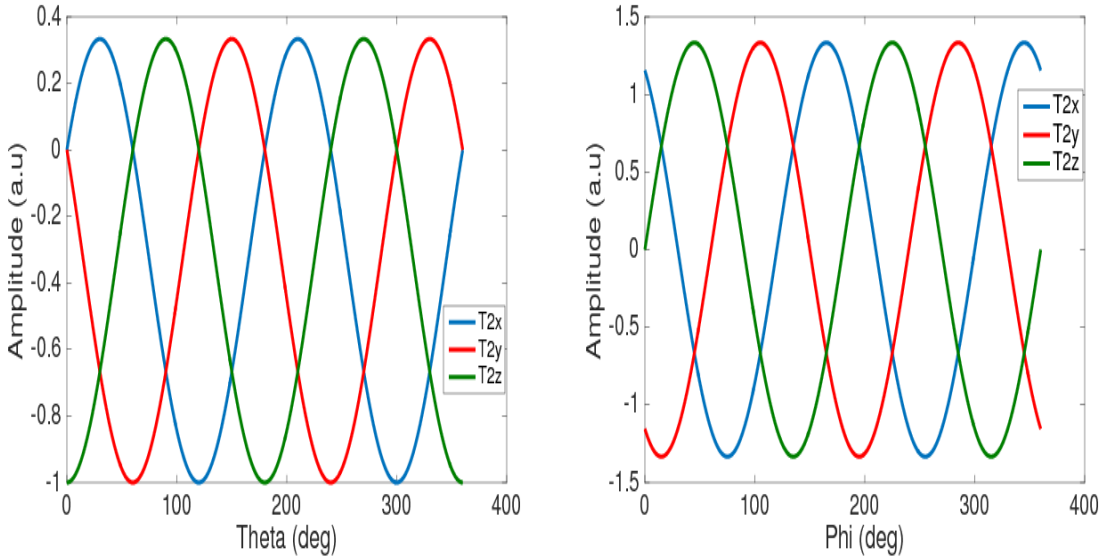

(a) Pump (b) Probe

Figure 6.15.: Dependence of the amplitude of the T_{2x}, T_{2y}, and T_{2z} modes upon the angles θ and ϕ that define the orientation of the electric field of the pump and probe respectively within the plane of the GST/InAs(111) structure.

$$\left[\frac{1}{\sqrt{3}}\sin(2\theta) - \frac{2}{3}\sin^2(\theta)\right] + \left[\frac{-1}{\sqrt{3}}\sin(2\theta) - \frac{2}{3}d\sin(\theta)\right] + \left[-\cos^2(\theta) + \frac{1}{3}\sin^2(\theta)\right]$$

$$= \frac{2}{3}\left[\cos\left(2\theta - \frac{\pi}{3}\right) - \frac{1}{2}\right] + \frac{2}{3}\left[\cos\left(2\theta + \frac{\pi}{3}\right) - \frac{1}{2}\right] + \frac{2}{3}\left[\cos\left(\theta + \pi\right) - \frac{1}{2}\right]$$

$$= \frac{2}{3}\left[\cos\left(2\theta - \frac{\pi}{3}\right) + \cos\left(2\theta + \frac{\pi}{3}\right) + \cos\left(\theta + \pi\right)\right] - 1$$

$$= \frac{2}{3}\left[\cos 2\theta\left(\frac{1}{2} + \frac{1}{2} - 1\right) - \sin 2\theta\left(\frac{-\sqrt{3}}{2} + \frac{-\sqrt{3}}{2} + 0\right)\right] - 1$$

$$= -1$$

The summation of the expressions for the three modes in the AR signal leads to $\frac{2}{3}\sin(2(\theta - \phi))$ as shown below

$$\begin{array}{cc} \left(\frac{1}{\sqrt{3}}\sin(2\theta) - \frac{2}{3}\sin^2(\theta)\right) & \left(\frac{2}{\sqrt{3}}\cos(2\phi) - \frac{2}{3}\sin(2\phi)\right) \\ + \left(-\frac{1}{\sqrt{3}}\sin(2\theta) - \frac{2}{3}\sin^2(\theta)\right) & \left(-\frac{2}{\sqrt{3}}\cos(2\phi) - \frac{2}{3}\sin(2\phi)\right) \\ + \left(-\cos^2(\theta) + \frac{1}{3}\sin^2(\theta)\right) & \left(\frac{4}{3}\sin(2\phi)\right) \end{array}$$

$$= \frac{2}{3}\sin 2\theta\cos 2\phi + \frac{4}{9}\sin^2\theta\sin 2\phi - \frac{2}{3}\cos^2\theta\sin 2\phi + \frac{2}{9}\sin^2\theta\sin 2\phi$$

$$= \frac{2}{3}\sin 2\theta\cos 2\phi + \frac{2}{3}(\sin^2\theta - \cos^2\theta)\sin 2\phi$$

$$= \frac{2}{3}(\sin 2\theta\cos 2\phi - \cos 2\theta\sin 2\phi)$$

$$= \frac{2}{3}\sin(2(\theta - \phi)).$$

From the above summations it can be seen that for a (111) plane the TSRS theory predicts the excitation of three degenerate phonon modes that have three dimensional representations T_{2x}, T_{2y}, and T_{2z} and which can be observed in R and AR signals. For the R signal a linear superposition of three different polarisations of the T_2 mode leads to an amplitude of oscillation that does not change as the pump and probe polarisations change. However for the AR signal, the TSRS theory predicts a dependence on pump and probe polarisation that varies as $\sin(2(\theta - \phi))$, so that when the angle between the pump and probe polarisation is $45°$, the amplitude of the oscillation will reach its maximum value. This angular dependence is exactly the same as that expected for the specular optical Kerr effect (SOKE).

As was mentioned in chapter 2, InAs has the T_d point group with five irreducible representations denoted as A_1, A_2, E, $T_1$and T_2 [107, 6, 8]. The zone centre phonon mode has the representation T_2 mode that is Raman active. At the zone center, the three dimensional T_2 mode splits into the longitudinal optical phonon and the doubly degenerate transverse optical phonon. In the Raman spectra obtained from the InAs (111) wafer the transverse optical phonon TO and longitudinal optical phonon LO have both

been detected. The ellipticity signal obtained from the InAs (111) wafer shows a clear oscillation with frequency of about 6.5 THz. The TSRS theory suggests that this is one of the three dimensional T_2 phonon modes, while the Raman spectra suggest that it is the transverse optical phonon.

The amplitude of the phonon observed in InAs (111) shows a clear $\sin(2(\theta-\phi))$ dependence on pump and probe polarization that can be explained by the TSRS theory and is also characteristic of the SOKE. The phonon amplitude at 0, 90 and 180° degrees is almost zero, therefore the SSC mechanism does not contribute to the excitation of the COPs because this mechanism does not depend upon the pump polarisation.

In the Raman spectra obtained from the InAs(111) wafer, TO and LO phonons are observed while in the pump-probe measurements only the TO phonon is observed. The reason why the pump-probe measurement detects the TO phonon mode but not the LO phonon mode is not yet clear, but there are three possibilities. First, from the calculations of section (1.6.1) that consider the Raman selection rules for backscattering from the (111) wafer of zinc blend structure, to detect both TO and LO phonon modes, the polarisation of the incident and scattered beams should be in the same plane. In pump-probe measurements two beams interact with different electric polarisations so perhaps the polarisation of the incident and scattered beams are not in the same plane. Second, there may be some fundamental reason, based upon a more detailed microscopic treatment, for why a pump-probe signal from the LO phonon is either forbidden or so weak as to be undetectable. The third possibility could be instrumental, for example due to limited frequency resolution.

The study of the dependence of the phonon signal upon evaluated pump fluence for InAs (111) wafer revealed no change in the frequency, amplitude or phase of the observed phonon mode, suggesting that no pump-induced structural modification of the InAs (111) structure takes place.

6.7. Summary

Time resolved pump-probe measurements were performed on InAs (111) wafer to obtain information about the frequency, amplitude, phase, and relaxation time of coherent optical phonons within the material. Time resolved transient refelctance (R) and ellipticity (complex anisotropic reflectance (AR)) measurements were made. A three-dimensional T_2 optical phonon was observed in the ellipticity signal and this identical as the transverse optical phonon mode TO. The sensitivity of the phonon amplitude to pump polarisation was similar to that expected from the specular optical Kerr effect (SOKE) within anisotropic medium. It was shown that this behaviour is predicted by a theory of impulsive stimulated Raman scattering (ISRS) in which three degenerate T_2 modes are excited simultaneously and superpose to yield the observed change in the probe beam polarisation. Raman spectra obtained from InAs (111) reveal the transverse optical phonon mode observed in pump-probe measurements, in addition to two other modes which are ascribed to the longitudinal and surface optical phonons. Exposure of InAs(111) to elevated pump fluence appears not to induce any significant structural changes.

7. Observation of coherent optical phonons in GST epilayers grown on an InAs(111) wafer

In this chapter I will present time resolved reflectivity and ellipticity measurements that can help to understand the excitation of coherent optical phonons in GST, which may give insight into the non-thermal nature of phonon excitation and the structural phase transition at high fluence. The response of the sample to the pump and probe polarisations, to the sample orientation and to high pump fluence will be described. The results are interpreted in terms of the transient stimulated Raman scattering (TSRS) theory that was explained in Chapter 3.

7.1. Experimental results

The pump-probe technique used to perform the time resolved transient reflectivity and ellipticity measurements on epitaxial $\mathrm{Ge_2Sb_2Te_5/InAs(111)}$ is same as that used for InAs (111). The measurements have been performed on two different epitaxial GST/InAs(111) samples provided by the Paul Drude Institute, Berlin. The thickness of the first epitaxial GST/InAs(111) sample was 22 nm while the second epitaxial GST/InAs(111) sample had a thickness of 20 nm.

7.1.1. Dependence of the coherent optical phonon signal upon pump polarisation for the first epitaxial GST/InAs(111) sample

To investigate the dependence of time resolved transient reflectivity and ellipticity signals upon the pump polarisation, the applied pump beam was incident normal to the sample while the s- polarised probe beam was incident at 45° as shown in figure 7.1. The p-polarised state of the pump beam, with the pump electric field parallel to the plane of the optical table, was defined as the 0° orientation. The polarisation state of the pump beam was varied through 180° in 10 steps starting from p-polarisation.

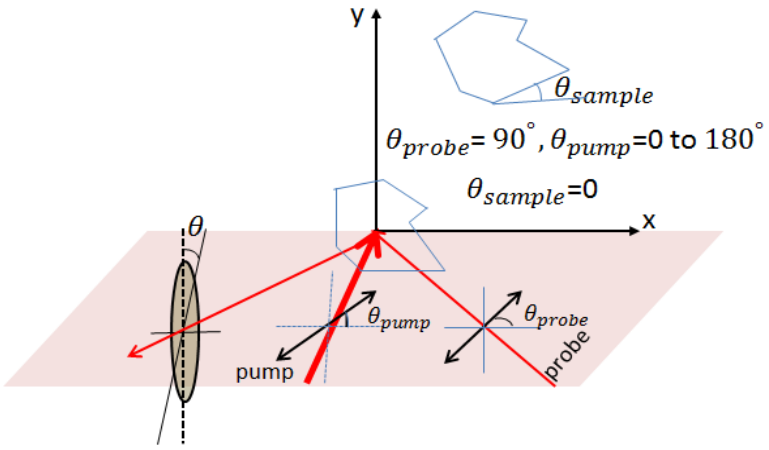

Figure 7.1.: Experimental configuration for study of the response of the first GST/InAs(111) sample to the changing pump polaraization

Figure 7.2 shows typical transient reflectivity (R) signals obtained from the first GST/InAs (111) structure. The probe beam was s-polarised while the pump polarisation was varied. The initial rise of the signal occurs within about 124 fs and is attributed to the photo-excitation and thermalization of an electron-hole plasma. Weak oscillations are observed within the signal. The measurements reveal that the transient R signal is independent of pump polarisation except for a small variation in the signal amplitude around zero delay. Similar transient R signals were detected for the InAs(111) reference sample, suggesting that the transient R signal observed in GST/InAs(111) is dominated by the response of the InAs substrate.

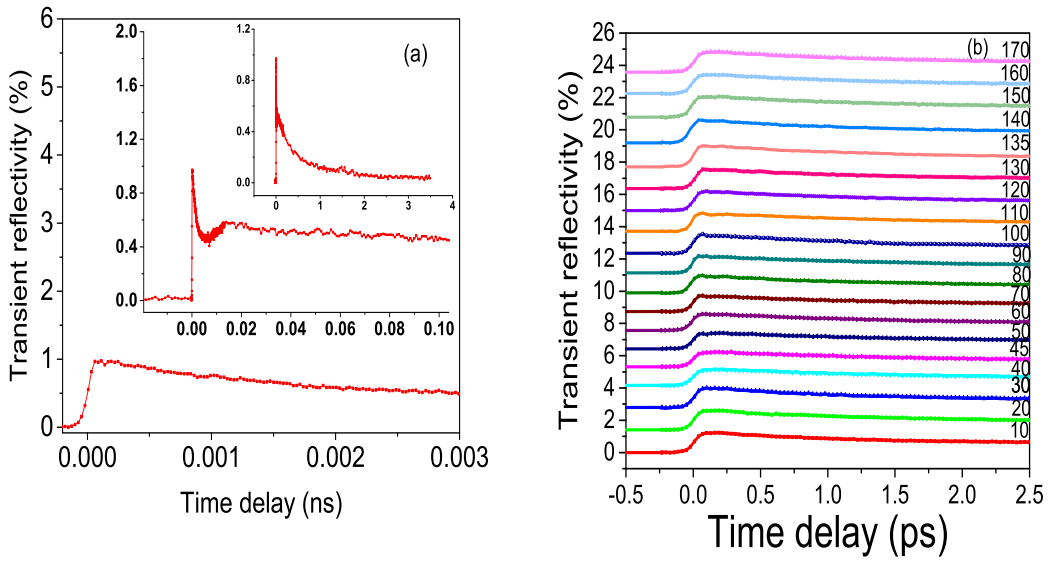

Figure 7.2.: Time resolved reflectivity signals obtained from GST/InAs (111). The pump beam was applied nearly normal to the sample while the probe beam was s-polarised and incident at $45°$. (a) Typical transient reflectivity signal, for $45°$ pump polarisation, plotted on different timescales. (b) Transient reflectivity signals for different pump polarisations.

Figure 7.3 (a) shows a typical time resolved ellipticity signal obtained from the first GST/InAs(111) structure. The probe beam was s-polarized while the pump polarisation was varied. Around zero time delay, when the pump and probe overlap in time, a large peak is observed due to the specular optical Kerr effect (SOKE). The SOKE peak has maximum amplitude when the pump and probe polarisations lie $45°$ apart. The peak appears because the electron momentum distribution in the sample is modified by the pump, and is short-lived due to the short momentum relaxation time. The SOKE peak is followed by an oscillation with frequency that increases with time during the scan, and which has a relaxation time of about 1.75 ps. After applying heat to the sample the bonding between neighbouring ions is weakened, which leads to oscillations of lower frequency, but with the frequency increasing as the samples cools. Figure 7.3 (b) shows the ellipticity signals obtained for different pump polarisations, while figure 7.3(c) is an expanded view that shows the oscillations more clearly. The oscillatory components obtained after subtracting a background are shown in figure (d). The power spectra obtained from the oscillatory components of the ellipticity signals are shown in Figure 7.3 (e).

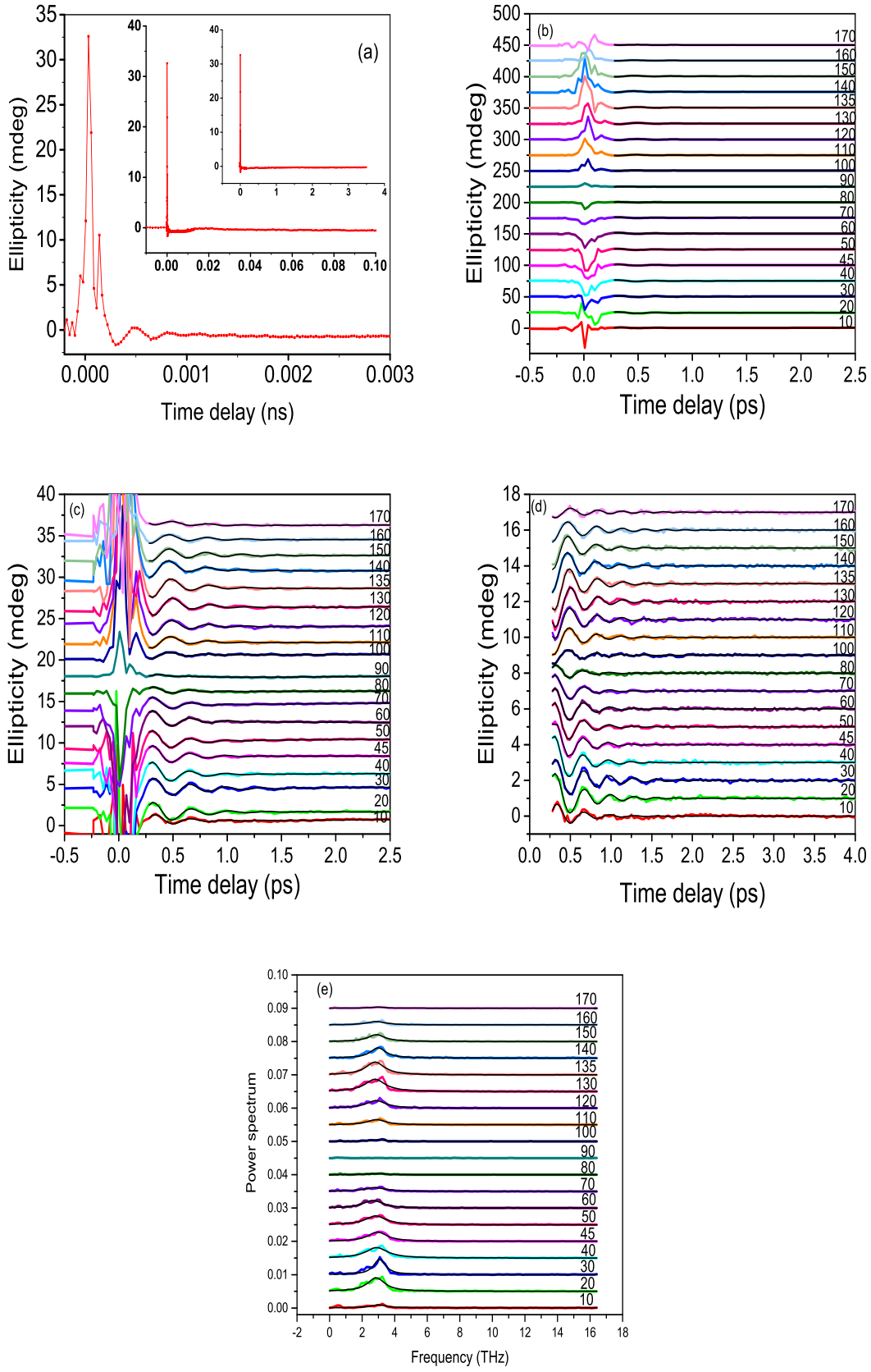

Figure 7.3.: Time resolved ellipticity signals obtained from the first GST/InAs (111) sample. The pump beam was applied nearly normal to the sample while the probe beam was s-polarised and incident at $45°$. (a) Typical ellipticity signal for $45°$ pump polarisation, plotted on different timescales. (b) Ellipticity signals for different pump polarisations. (c) Expanded view of ellipticity signals. (d) Oscillatory component of ellipticity signal after subtraction of background. (e) Power spectra obtained from the oscillatory components of the ellipticity signals.

Figures 7.4 (a) and (b) present the dependence of the oscillation frequency upon pump polarisation. Figure 7.4 (a) shows the oscillation frequencies obtained firstly by fitting a Lorentzian curve to the peak in the power spectrum, and secondly by fitting the raw time domain data to equation 5.32 with the chirp parameter set equal to zero. The frequencies determined by these two methods are found to be in good agreement and appear to be independent of pump polarisation. The results for 90° have been excluded on the grounds that the oscillation amplitude was too small to yield a reliable fit. The frequency for the combined data in (a) is determined to be 2.897 $\pm$ 0.025 THz for FFT data and 2.925$\pm$ 0.017 THz for raw time domain data. Figure 7.4 (b) again displays the frequency of oscillation determined from the power spectrum, but this time in comparison with that obtained by fitting equation 5.32 to the oscillatory component of the data after background subtraction, and allowing the chirp parameter to vary. The latter method yields a frequency of 2.380 $\pm$ 0.073 THz. The power spectrum yields the average value of the frequency during the whole scan, while fitting the time domain data to a chirped sinusoid yields the value of the frequency at beginning of the scan when the bonding is weakest and the frequency lowest. The instantaneous frequency ω when the oscillations have just damped out, and are no longer detectable in the measurement, can be estimated. To do this we take the difference of the frequency extracted from the power spectrum ω_{ps} and the instantaneous frequency at the beginning of the scan that extracted from time domain fitting ω_{TD}, and add it to the frequency extracted from the power spectrum ω_{ps} (i.e $\omega = (\omega_{ps} - \omega_{TD}) + \omega_{ps}$). In the present case this yields a frequency of 3.41 THz. Figure 7.4 (c) and (d) show the dependence of the phonon amplitude upon pump polarisation. The amplitude shows a clear dependence on pump polarisation and has maximum value when pump and probe polarisations lie 45° apart. The variation of phase is shown in figure 7.4(e). The phase has a value of about 0 rads until the orientation of the pump electric field reaches 90° after which it has a value of about π rads. The dependence of the line width, relaxation time and chirp upon pump polarisation is shown in figure 7.4 (f), (g) and (h) respectively and exhibit no clear trend. The observed variations are probably due to a gradual drift in the optical alignment since the 0 and 180° configurations should in principle be equivalent .

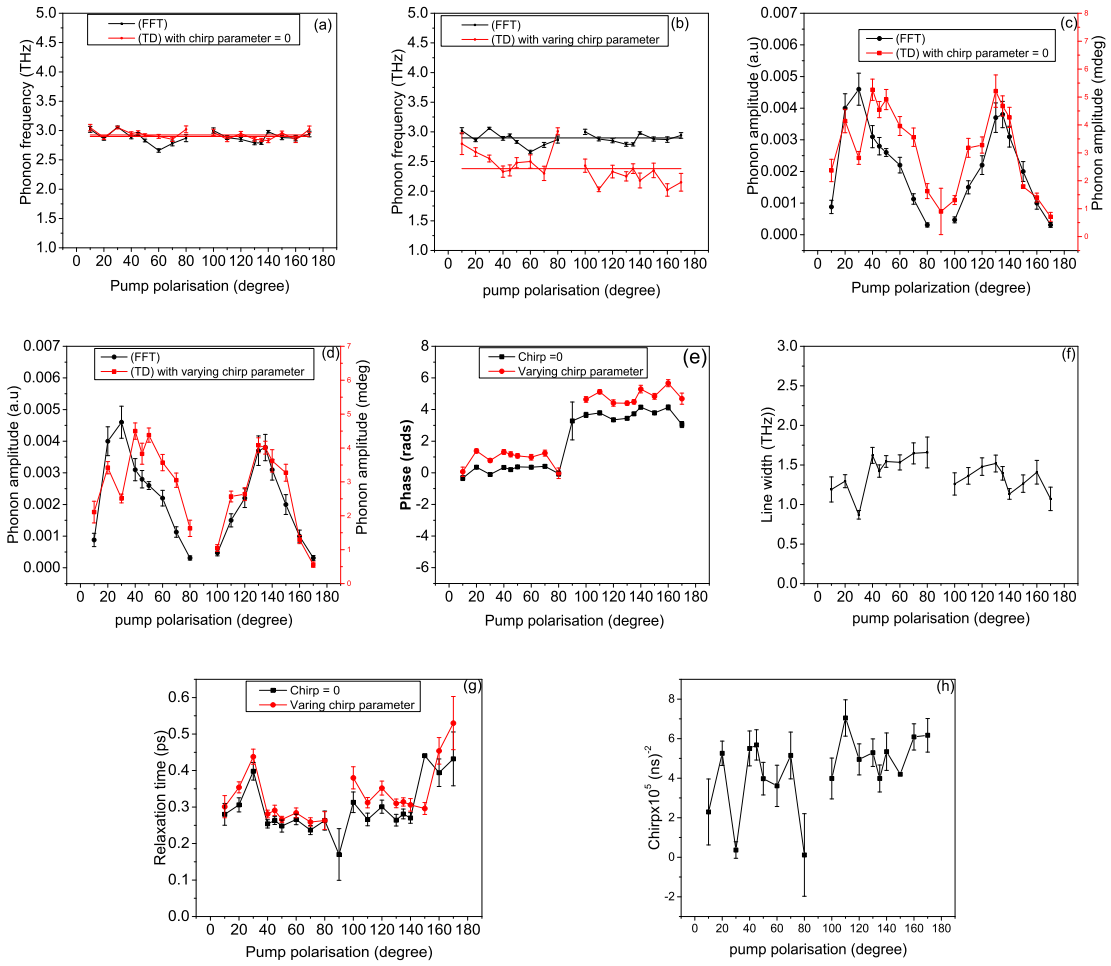

Figure 7.4.: The dependence of (a), (b) frequency, (c), (d) amplitude, (e) phase, (f) line width, (g) relaxation time, and (h) chirp parameter upon the pump polarisation are shown for measurements made on the first GST/InAs (111) sample. The pump beam was incident normal to the sample while the probe beam was incident at $45°$ and s-polarised. In (a) each black square represents the frequency value obtained by fitting a Lorentzian to the power spectrum, and the red circles represent the frequency values obtained by fitting the data to equation 5.32, with the chirp parameter set equal to zero, before subtracting the background. In (b) the black squares represent the frequency values obtained from the power spectra, while the red circles represent the frequency values obtained from fits to equation 5.32 after subtracting the background and allowing the chirp parameter to vary. In (c) the black circles represent the amplitude values obtained by fitting a Lorentzian lineshape to the power spectra, while the red squares represent the amplitude values obtained from fits to equation 5.32 before subtracting the background. In (d) the black circles represent the amplitude values obtained by fitting a Lorentzian lineshape to the power spectra while the red squares represent the amplitude values obtained from fits to equation 5.32 after subtracting the background from the data and allowing the chirp parameter to vary. In (e) and (g) the black circles represent the phase and relaxation time values respectively obtained from fitting equation 5.32 to the data before subtracting the background and with the chirp parameter set equal to zero while the red circles represent the phase and relaxation time values obtained from fits to equation 5.32 after subtracting the background and allowing the chirp parameter to vary.

7.1.2. Dependence of the coherent optical phonon signal upon sample orientation for the first epitaxial GST/InAs(111) sample

The dependence of the coherent optical phonon signal from the first GST/InAs (111) sample was studied as the sample orientation was changed from 0 to $180°$. The pump beam was applied close to normal to the sample with fixed polarisation angle of $45°$ while the probe beam was incident at $45°$ to the normal with fixed s-polarisation as shown in figure 7.5.

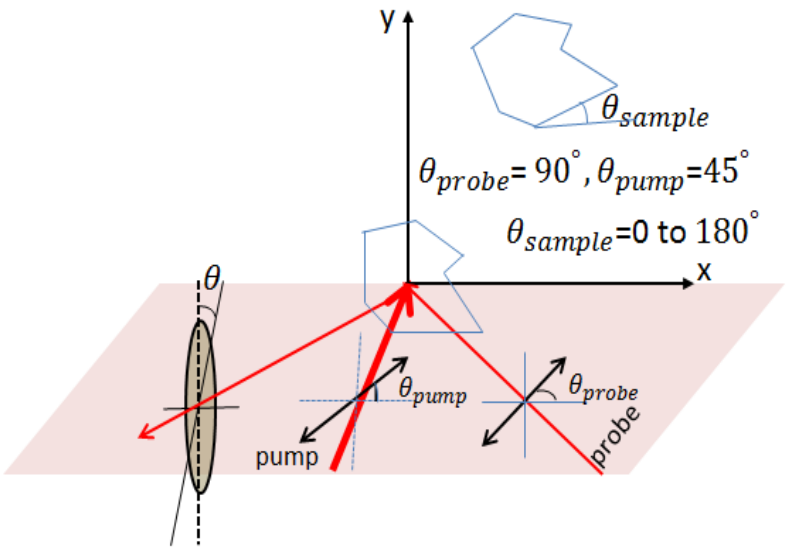

Figure 7.5.: Experimental configuration used to study the response of the first GST/InAs(111) sample to changing the sample orientation

The sign of the SOKE peak and the phase of the oscillation are unchanged as the sample orientation is varied. The oscillatory signal before and after subtraction of a background is shown in Figure 7.6 (a) and (b) respectively. The power spectra obtained from the subtracted data are shown in figure 7.6 (c).

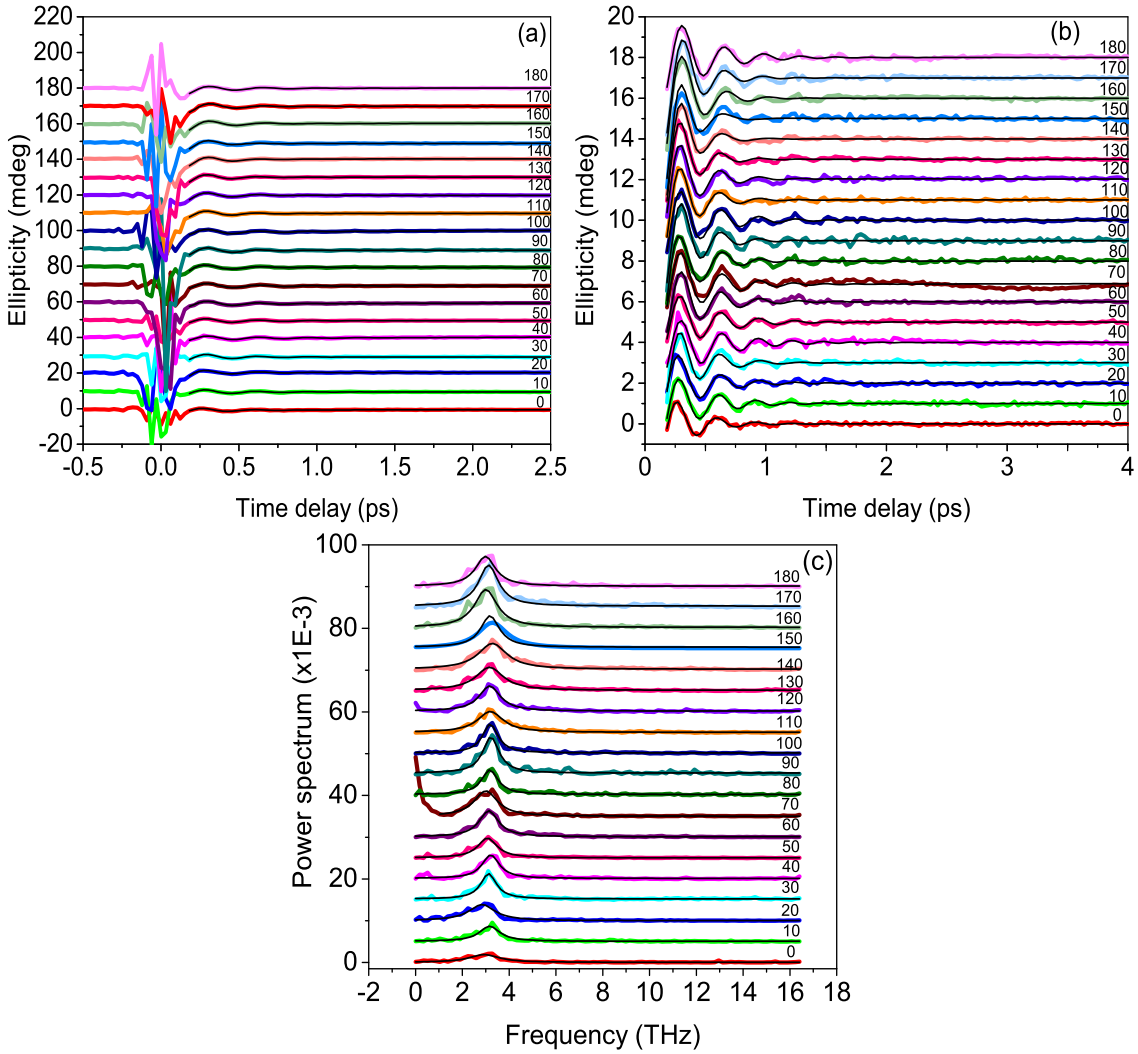

Figure 7.6.: Time resolved ellipticity signals obtained from the first GST/InAs (111) sample as the sample was rotated from 0 to 180° about its normal direction. The pump beam was at close to normal incidence with polarisation angle of 45° while the probe beam was incident at 45° to the normal with s-polarisation. (a) Ellipticity signal before subtraction of a background. (b) Oscillatory components of the ellipticity signal after subtraction of a background as described in chapter (5). (c) Power spectra obtained from the oscillatory component of the ellipticity signal shown in (b).

Figure 7.7(a) shows the dependence of the phonon frequency upon the sample orientation. The phonon frequency was determined firstly by fitting a Lorentzian curve to the peak in the power spectrum and secondly by fitting equation 5.32 to the time domain signal before subtracting the background and setting the chirp parameter equal to zero. The phonon frequency is 3.12±0.02 THz for the FFT data and 3.00±0.02 THz for the time domain data and independent of sample orientation. In Figure 7.7 (b) the frequency obtained from the power spectrum is compared with that obtained by fitting equation 5.32 to the oscillatory component of the data, after subtraction of a back-

ground, and with the chirp parameter allowed to vary. The phonon frequency from this method is determined to be 2.76 $\pm$ 0.06 THz which yields the instantaneous frequency at the beginning of the scan. The phonon frequency extracted from this measurement is slightly higher than that extracted from measurements in which the pump polarisation was varied. This difference in frequency might due to a difference in the accuracy with which the pump and probe spots were focused and overlapped leading to a difference in the pump fluence at the position of the probe spot that results in a difference in the sample temperature in each measurement. The instantaneous frequency ω when the oscillations have just damped out, and are no longer detectable in the measurement, can be estimated in the same way as before. Again we take the difference of the frequency extracted from the power spectrum ω_{ps} and the instantaneous frequency at the beginning of the scan that extracted from the time domain fitting ω_{TD}, and add it to the frequency extracted from the power spectrum ω_{ps} (i.e $\omega = (\omega_{ps} - \omega_{TD}) + \omega_{ps}$). In the present case this yields a frequency of 3.48 THz. The systematic difference in the frequencies obtained by the first two and third method has a similar origin to that in the previous section . The variation of the phonon amplitude extracted by the same fitting methods is plotted in Figure 7.7(c) and (d). An apparent variation in phonon amplitude is observed as the sample is rotated. This may be due either to inhomogeneity of the sample or a variation in the overlap of the pump and probe spots. The amplitude at 0 and 180° should be exactly equivalent, which suggests that when the sample is rotated between these two angles the position of the laser spots on the sample is different. The phase of the oscillation is presented in figure 7.7 (e) and shows a fairly constant value with sample orientation. The line width, the relaxation time and chirp parameter are plotted in figure 7.7 (f), (g) and (h) respectively. While there is some scatter in the values, there is no systematic variation, suggesting that these parameter values are independent of the sample orientation.

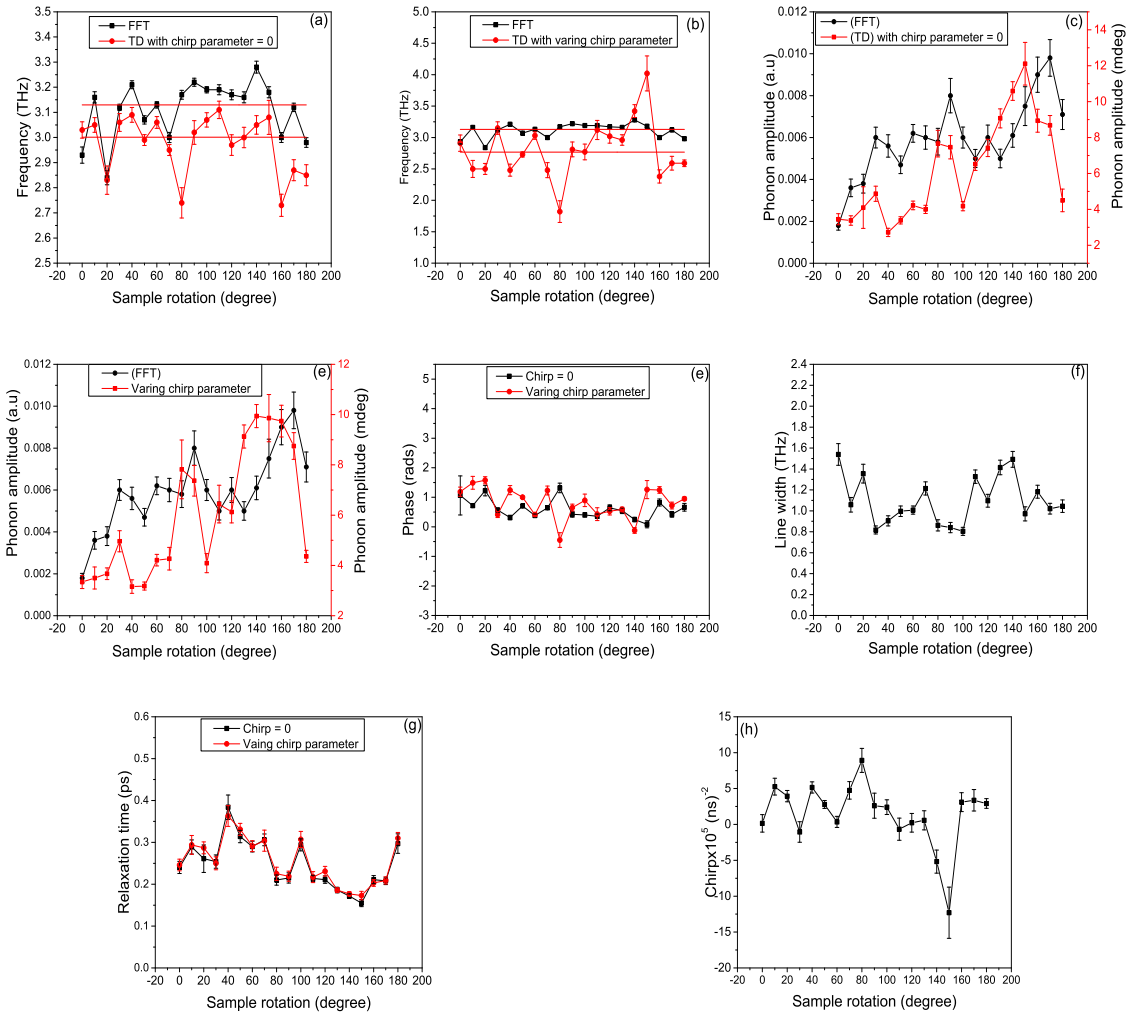

Figure 7.7.: The dependence of (a), (b) frequency, (c), (d) amplitude, (e) phase, (f) line width, (g) relaxation time, and (h) chirp parameter upon the sample orientation are shown for measurements made upon the first GST/InAs (111) sample. The pump beam was at close to normal incidence upon the sample with fixed polarisation angle of 45° while the probe was incident at 45° and s-polarised. In (a) the black squares represent the frequency values obtained by fitting a Lorentzian to the power spectrum, while the red circles represent the frequency values obtained from fitting equation 5.32 to the data before subtracting the background and with the chirp parameter set equal to zero. In (b) the black squares again represent the frequency values obtained from the power spectra, while the red circles represent the frequency values obtained from fits to equation 5.32 after subtracting the background and allowing the chirp parameter to vary. In (c) the black circles represent the amplitude values obtained from fitting a Lorentzian to the power spectrum while the red squares represent the amplitude values obtained from fitting equation 5.32 to the data before subtracting the background. In (d) the black circles represent the amplitude values obtained from fits to the power spectra while the red squares represent the frequency values obtained from fitting equation 5.32 to the data after subtracting the background and allowing the chirp parameter to vary. In (e) and (g) the black circles represent the phase and relaxation time values respectively obtained from fitting equation 5.32 to the data before subtracting the background and with the chirp parameter set equal to zero while the red circles represent the phase and relaxation time values obtained from fits to equation 5.32 after subtracting the background and allowing the chirp parameter to vary.

7.1.3. Dependence of the coherent optical phonon signal upon probe polarisation for the first epitaxial GST/InAs(111) sample

The dependence of the coherent phonon signal from the first GST/InAs (111) upon the probe polarisation was studied by fixing the probe polarisation at $45°$and rotating the pump polarisation and the sample together so that their orientation relative to the probe polarisation was varied. The pump beam was applied close to normal to the sample while changing its polarisation, while the probe beam was incident at $45°$ to the normal with fixed s-polarisation as shown in figure 7.8.

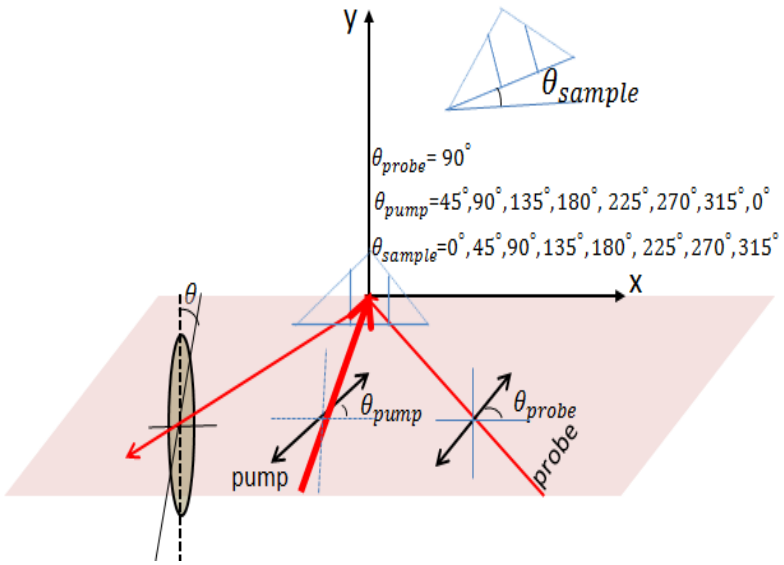

Figure 7.8.: Experimental configuration for studying the response of the first GST/InAs(111) sample to probe polarisation

The coherent phonon oscillations appear when the difference in polarisation between pump and probe is $45°$ and disappear when the difference in polarisation between pump and probe is $90°$. The time resolved ellipticity signal and the oscillatory component of the ellipticity signal for different probe polarisations are shown in figure 7.9 (a) and 7.9(b). The oscillatory signal before and after subtraction of a background is shown in Figure 7.9(c) and 7.9(d) respectively. The power spectra obtained from the subtracted data are shown in figure 7.9 (e).

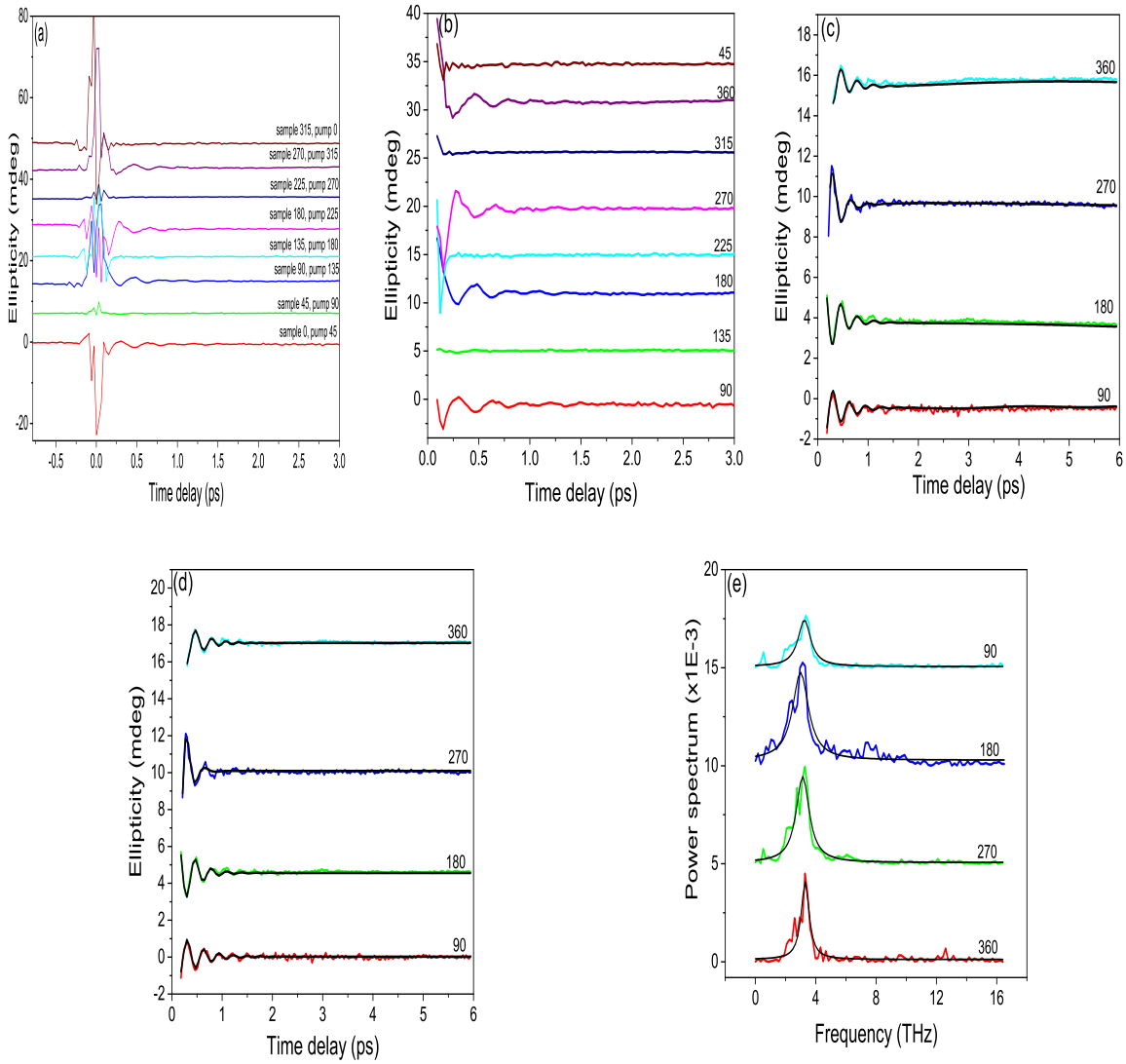

Figure 7.9.: Time resolved ellipticity signals obtained from the first GST/InAs (111) sample as the sample and pump polarisation were rotated together with fixed probe polarisation. The pump beam was at close to normal incidence while the probe beam was incident at $45°$ to the normal with s-polarisation. The angle between the pump polarisation and the sample edge was fixed to $45°$. (a) The ellipticity signal for different probe polarisations. (b) Oscillatory components of the ellipticity signal. (c) Ellipticity signal before subtraction of a background. (d) Oscillatory components of the ellipticity signal after background subtraction. (e) Power spectra obtained from the oscillatory component of the ellipticity signal shown in (c).

Figure 7.10 (a) shows the dependence of the phonon frequency upon the probe polarisation. The phonon frequency was determined firstly by fitting a Lorentzian curve to the peak in the power spectrum and secondly by fitting equation 5.32 to the time domain signal before subtracting the background and setting the chirp parameter equal to zero and finally by fitting equation 5.32 to the oscillatory component of the data, after sub-

traction of a background, and with the chirp parameter allowed to vary. The frequency for the combined data in (a) was determined to be 3.19 $\pm$ 0.06 THz for the FFT data and 3.00$\pm$ 0.05 THz for the raw time domain data when the chirp parameter was set to equal zero and 2.76$\pm$ 0.16 THz for the raw time domain data when chirp parameter was allowed to vary. The variation of the phonon amplitude extracted by the same fitting methods is plotted in Figure 7.10 (b). An apparent variation in phonon amplitude is observed as the probe polarisation is changed. The phase of the oscillation is presented in figure 7.10 (c) and shows there is not much variation in the signals apart from the phase alternating by pi rads between successive points . The relaxation time and the line width are presented in figure 7.10 (d) and (e) and show a fairly constant value. The chirp parameter is presented in figure 7.10 (f) and shows no clear dependence on the probe polarisation.

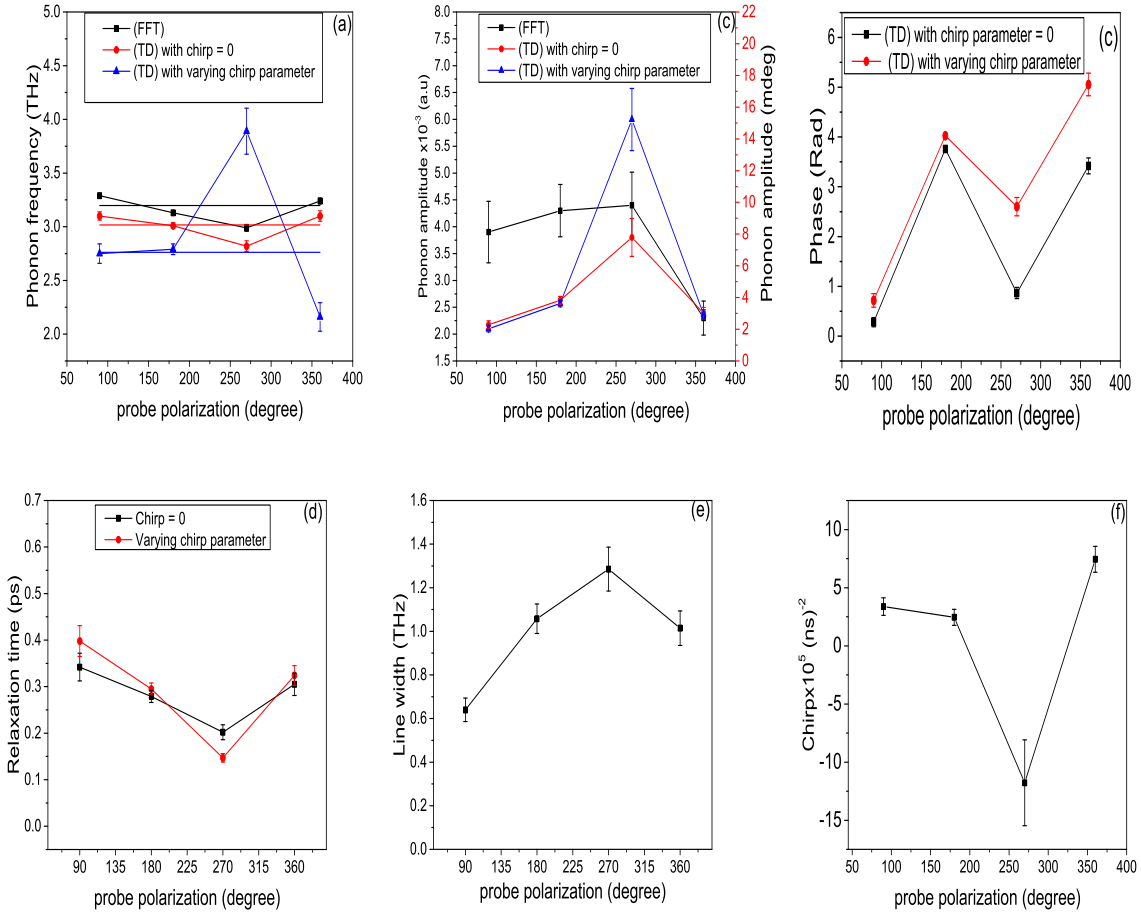

Figure 7.10.: The dependence of (a) frequency, (b) amplitude, (c) phase, (d) relaxation time, (e) line width and (f) chirp parameter upon the probe polarisation are shown for measurements made upon the first GST/InAs (111) sample. The pump beam was at close to normal incidence upon the sample with varied polarisation angles while the probe was incident at $45°$ and s-polarised. In (a) the black squares represent the frequency values obtained by fitting a Lorentzian to the power spectrum, while the red circles represent the frequency values obtained from fitting equation 5.32 to the data before subtracting the background and with the chirp parameter set equal to zero and the blue triangles represent the phonon frequency obtained from fitting equation 5.32 to the data after subtraction of a background, and with the chirp parameter allowed to vary. In (b) the black squares represent the amplitude values obtained from fitting a Lorentzian to the power spectrum while the red circles represent the amplitude values obtained from fitting equation 5.32 to the data before subtracting the background and with the chirp parameter set equal to zero and the blue triangles represent the amplitude values obtained from fitting equation 5.32 to the data after subtracting the background and allowing the chirp parameter to vary. In (c) and (d) the black squares represent the phase and relaxation time values respectively obtained from fitting equation 5.32 to the data before subtracting the background and with the chirp parameter set equal to zero while the red circles represent the phase and relaxation time values respectively obtained from fitting equation 5.32 after subtracting the background and allowing the chirp parameter to vary.

7.1.4. Dependence of the coherent optical phonon signal upon pump fluence for the first epitaxial GST/InAs(111) sample

A structural phase transition may occur when a phase change material such as GST is heated by one or more laser pulses [108, 109, 110]. The effect of pump fluence on the transient ellipticity and reflectvity signals, and hence upon the COPs within GST/InAs (111), was studied when the pump and probe polarisations were set $45°$ apart. The pump beam was applied close to normal to the sample with fixed polarisation of $45°$ while the probe beam was incident at $45°$ to the normal with fixed s-polarisation as shown in figure 7.11.

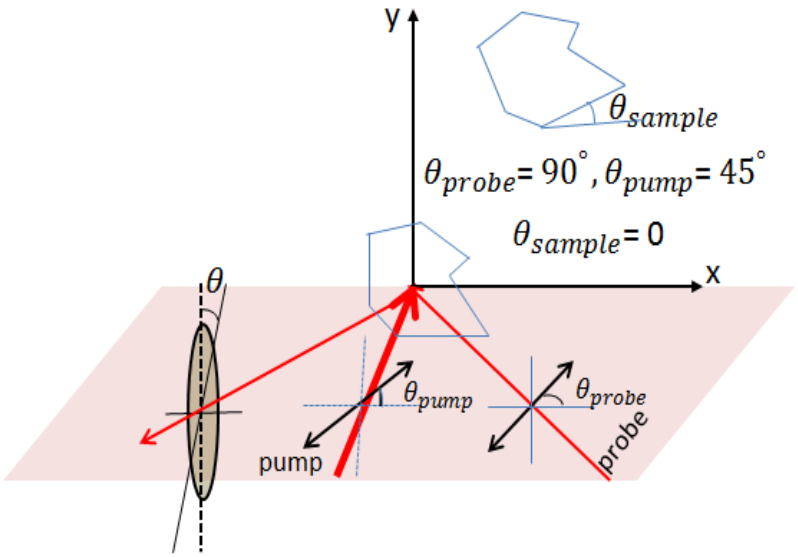

Figure 7.11.: Experimental configuration for studying the response of the first GST/InAs(111) sample to changing pump fluence

A measurement was made at high pump fluence then immediately repeated at a lower pump fluence of 0.99 $\mathrm{mJ/cm^2}$. The transient ellipticity and reflectivity signals obtained from the repeated measurements at the lower pump fluence of 0.99 $\mathrm{mJ/cm^2}$ are shown in figure 7.12 (a) and (b), while the signals obtained at the higher pump fluence are shown in figure 7.13 (a) and (b). Figure 7.12 (c) and (d) and 7.13(c) and (d) show the power spectra obtained from the ellipticity and reflectivity signals in the low and elevated fluence measurements respectively. At low pump fluence, oscillations associated with a coherent optical phonon, with frequency of about 3 THz, are observed in the ellipticity

signal but not the reflectivity signal. The mode with frequency of about 3 THz vanishes after exposure to a fluence of 2.97 $\mathrm{mJ/cm^2}$, while another COP with frequency of about 3.5 THz and larger amplitude appears in both ellipticity and reflectivity signals .

After exposure to high fluence (measurement pump fluence = 0.99 $\mathrm{mJ/cm^2}$)

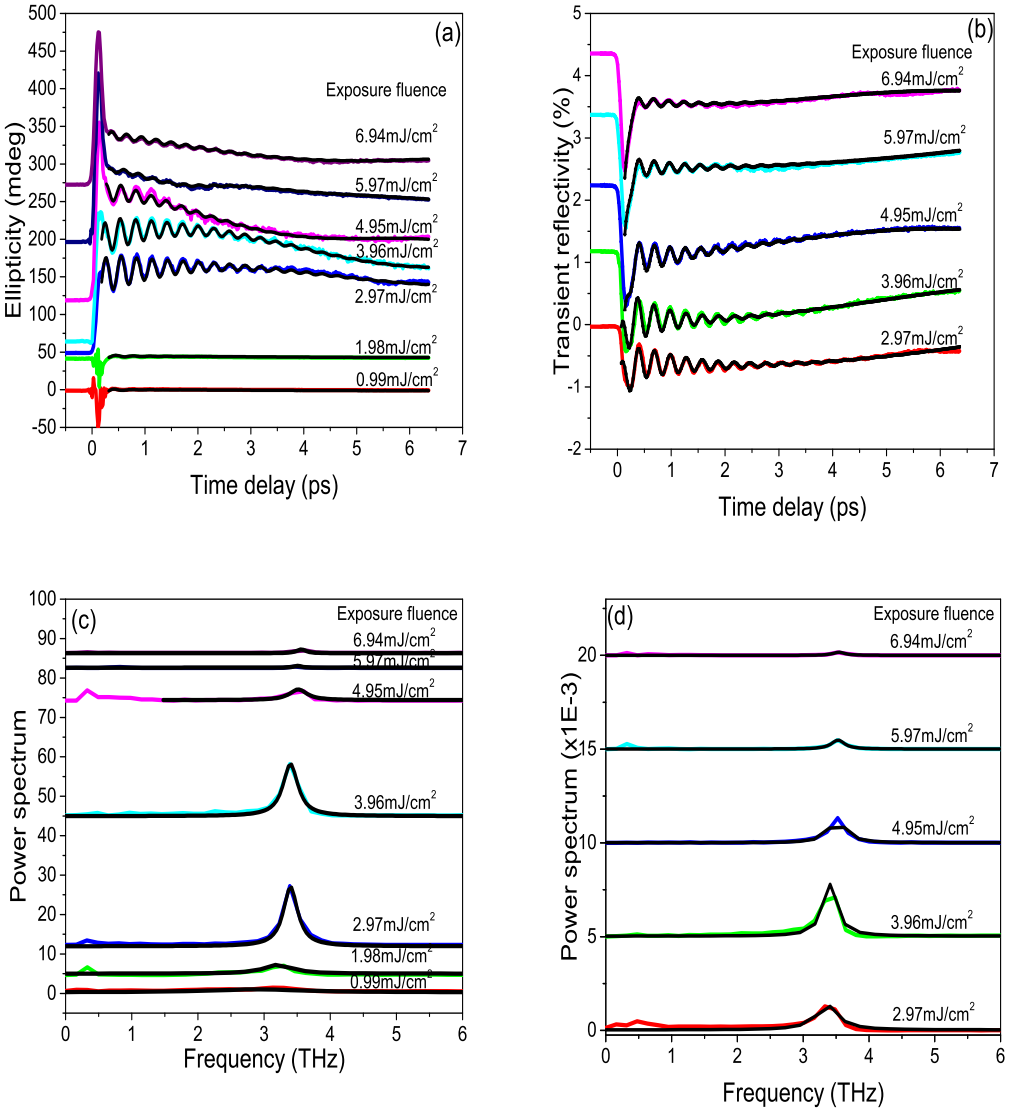

Figure 7.12.: The dependence of transient ellipticity and reflectivity signals obtained from the first GST/InAs (111) sample after exposure to elevated pump fluence when the pump and probe polarisations were set 45° apart. A measurement was made at high pump fluence then immediately repeated at a lower pump fluence of 0.99 $\mathrm{mJ/cm^2}$. (a) and (b) transient ellipticity and reflectivity signals respectively obtained from the repeated measurements at the lower pump fluence of 0.99 $\mathrm{mJ/cm^2}$ (c) and (d) are the power spectra obtained from (a) and (b) respectively .

The reflectivity and ellipticity signals obtained from the repeated measurements at the lower pump fluence in Fig 7.12 (a) and (b) and the reflectivity and ellipticity signals

obtained at the higher pump fluence in figure 7.13 (a) and (b) were fitted by fitting the raw time domain data to equation 5.32 with the chirp parameter set equal to zero. The power spectrums in figure 7.12 (c) and (d) and figure 7.13 (c) and (d) were fitted to a using Lorentzian form.

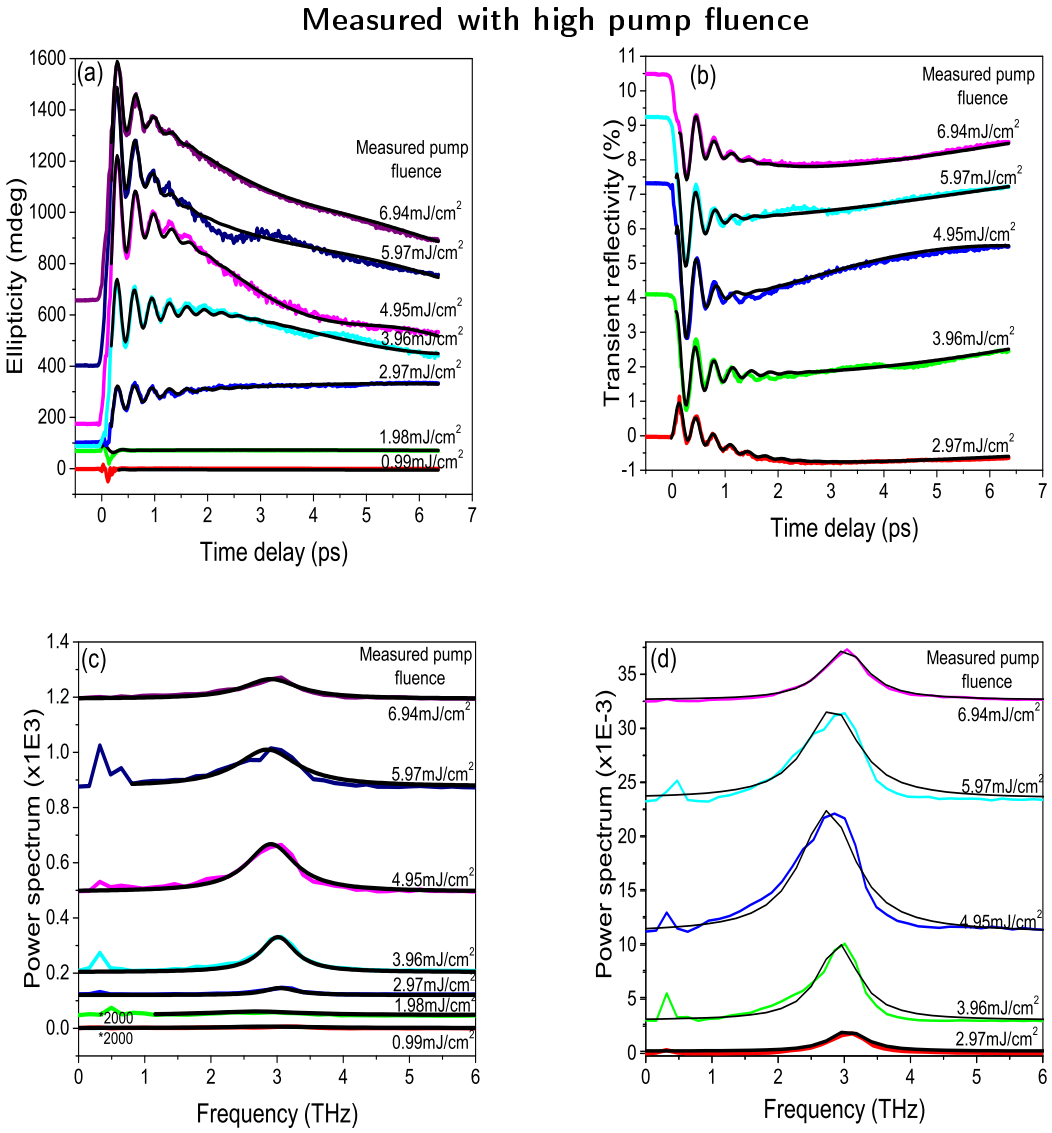

Figure 7.13.: The dependence of transient ellipticity and reflectivity signals obtained from the first GST/InAs (111) sample at elevated pump fluence when the pump and probe polarisations were set 45° apart. (a) and (b) ellipticity and transient reflectivity signals respectively obtained at elevated pump fluence. (c) and (d) are the power spectra obtained from the transient ellipticity and reflectivity signals in (a) and (b) respectively.

Figure 7.14(a) and (f) shows the variation of the phonon frequency obtained from ellipticity and reflectivity signals during repeated scans at low fluence respectively. The

phonon frequency was determined firstly by fitting a Lorentzian curve to the peak in the power spectrum and secondly by fitting equation 5.32 to the time domain signal before subtracting the background and setting the chirp parameter equal to zero. The variation of the phonon amplitude obtained from ellipticity and reflectivity signals during repeated scans at low fluence extracted by the same fitting methods is plotted in figure 7.14 (b) and (g) respectively. The amplitudes increase up until an elevated fluence of 2.97 $\mathrm{mJ/cm^2}$and then decrease monotonically with increasing pump fluence. The phase of the oscillations observed in the transient ellipticity and reflectivity signals during repeated scans at low fluence are shown in Figure 7.14 (c) and (h) respectively. The phase of oscillation also varies with increasing pump fluence. The variation of the amplitude and phase again suggests a change in the structure of the sample with increasing fluence. Figure 7.14 (d), (e) and (i), (j) show only a small variation of the line width and the relaxation time once the elevated pump fluence has exceeded 2 $\mathrm{mJ/cm^2}$

Figure 7.15 (a) and (f) shows the dependence of the phonon frequency obtained from ellipticity and reflectivity signals at elevated pump fluence respectively. The phonon frequency was determined firstly by fitting a Lorentzian curve to the peak in the power spectrum and secondly by fitting equation 5.32 to the time domain signal before subtracting the background and setting the chirp parameter equal to zero. The variation of the phonon amplitude obtained from ellipticity and reflectivity signals at elevated pump fluence extracted by the same fitting methods is plotted in figure 7.15(b) and (g) respectively. The amplitudes of both signals increased for elevated fluence values up to 4.95 $\mathrm{mJ/cm^2}$ before decreasing with further increase of the pump fluence. The phase of oscillation shows small variations with the pump fluence. Figure 7.15 (d), (e) and (i), (j) show only a small variation in the line width and the relaxation time with pump fluence.

At elevated pump fluence the COP frequency observed in ellipticity and reflectivity signals is approximetly 3.00 THz as shown in figure 7.15 (a) and (f). The oscillations obtained from the repeated scans at low fluence have a longer relaxation time than those obtained at high fluence. The lower pump fluence and the longer relaxation time mean that the sample temperature is on average much lower in the time period during which

oscillations are observed as compared to the measurements made at the elevated fluence. The extracted average frequency is therefore expected to be higher for the repeated measurement at low fluence compared to that at elevated fluence. The increase in frequency observed after increasing the pump fluence suggests that a structural change has been induced.

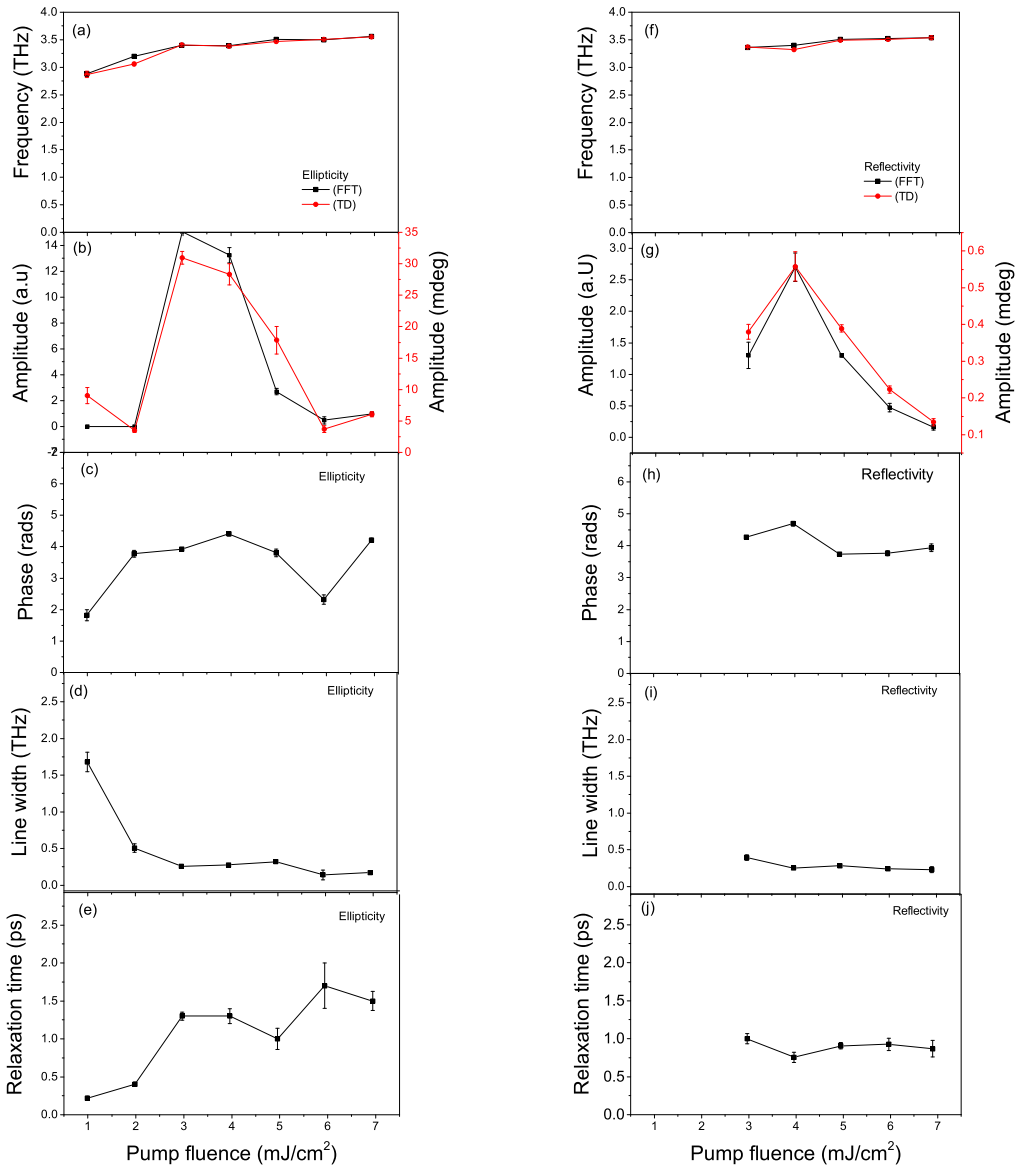

Figure 7.14.: The dependence of (a) and (f) frequency, (b) and (g) amplitude, (c) and (h) phase, (d) and (i) line width, (e) and (j) relaxation time of the oscillations observed in ellipticity and transient reflectivity signals acquired from repeated scans at a low fluence of 0.99 $\mathrm{mJ/cm^2}$ after measurements at elevated pump fluence are shown for measurements made upon the first GST/InAs (111) sample. The pump beam was at close to normal incidence upon the sample with $45°$ polarisation angle, while the probe was incident at 45° and s-polarised. In (a) and (f) the black squares represent the frequency values obtained by fitting a Lorentzian to the power spectrum, while the red circles represent the frequency values obtained from fitting equation 5.32 to the data before subtracting the background and with the chirp parameter set equal to zero. In (b) and (g) the black squares represent the phonon amplitude values obtained by fitting a Lorentzian to the power spectrum, while the red circles represent the phonon amplitude values obtained from fitting equation 5.32 to the data before subtracting the background and with the chirp parameter set equal to zero.

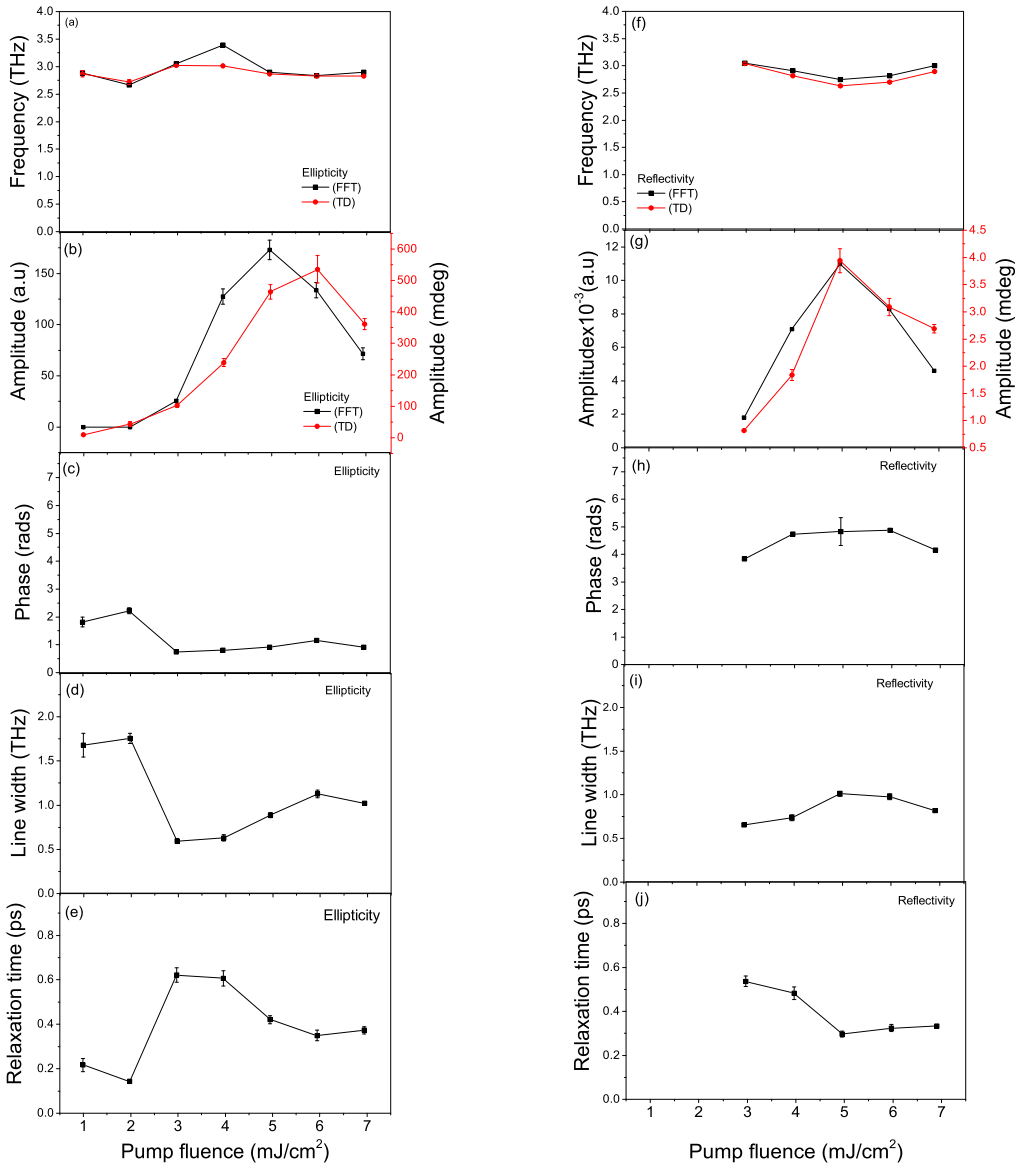

Figure 7.15.: The dependence of (a) and (f) frequency, (b) and (g) amplitude, (c) and (h) phase, (d) and (i) line width, (e) and (j) relaxation time of the oscillations upon pump fluence, observed in ellipticity and transient reflectivity signals acquired at elevated pump fluence, are shown for measurements made upon the first GST/InAs (111) sample. The pump beam was at close to normal incidence upon the sample with $45°$ polarisation angle while the probe was incident at $45°$ and s-polarised. In (a) and (f) the black squares represent the frequency values obtained by fitting a Lorentzian to the power spectrum, while the red circles represent the frequency values obtained from fitting equation 5.32 to the data before subtracting the background and with the chirp parameter set equal to zero. In (b) and (g) the black squares represent the phonon amplitude values obtained by fitting a Lorentzian to the power spectrum, while the red circles represent the phonon amplitude values obtained from fitting equation 5.32 to the data before subtracting the background and with the chirp parameter set equal to zero.

7.1.5. Dependence of the coherent optical phonon signal upon pump polarisation for the second epitaxial GST(111) sample

Figure 7.17 (a) shows a typical time resolved transient R signal obtained from the second GST/InAs(111) structure with s-polarised probe beam and pump beam with polarisation angle of 45° as shown in figure 7.16.

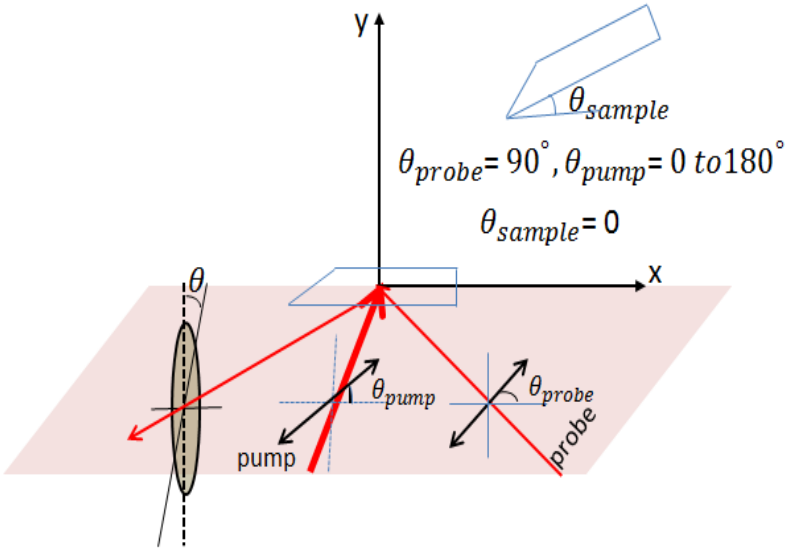

Figure 7.16.: Experimental configuration for studying the response of the second GST/InAs(111) sample to different pump polarization

The initial rise of the signal occurs within about 124 fs and is attributed to the photo-excitation and thermalization of an electron-hole plasma. Clear oscillations are observed within the signal. The transient R signals obtained for different pump polarisations are presented in figure 7.17 (b). The transient R signal appears to be independent of pump polarisation except for a small variation of the signal amplitude around zero time delay. The power spectra obtained from the transient R signals for time delays of 0.1 ps onwards are shown in figure 7.17 (c). Figure 7.18 (a) shows the oscillation frequencies obtained firstly by fitting a Lorentzian curve to the peak in the power spectrum, and secondly by fitting the raw time domain data to equation 5.32 with the chirp parameter set equal to zero. The phonon frequency is determine to be 3.37±0.03 THz for the FFT data and 3.34±0.03 THz for the raw time domain data with the chirp parameter set equal to zero. The phonon frequency appears independent of pump polarisation. Figure 7.18

(b), (c), (d) and (e) show the dependence of amplitude, line width, relaxation time and phase of oscillation upon pump polarisation. The plots suggest that there is no clear dependence upon pump polarisation.

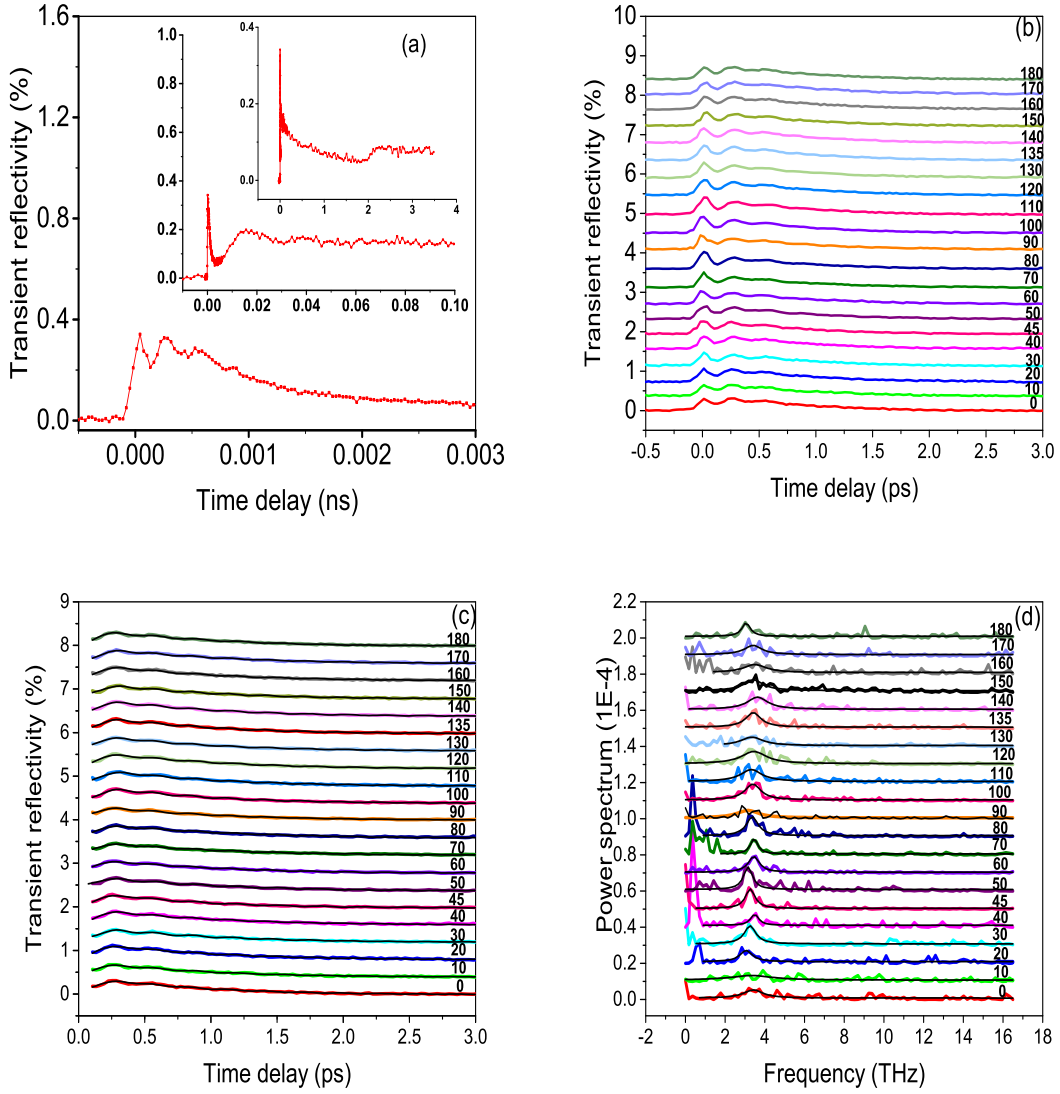

Figure 7.17.: Time resolved R signals obtained from the second GST/InAs (111) sample. The pump beam was incident nearly normal to the sample while the probe beam was s-polarised and incident at $45°$. (a) Typical transient R signal, for $45°$ pump polarisation, plotted on different timescales. (b) Transient R signals for different pump polarisations. (c) Oscillatory component obtained from the transient R signal for varied pump polariztion. (d) Power spectra obtained from the transient R signal at varied pump polarisation.

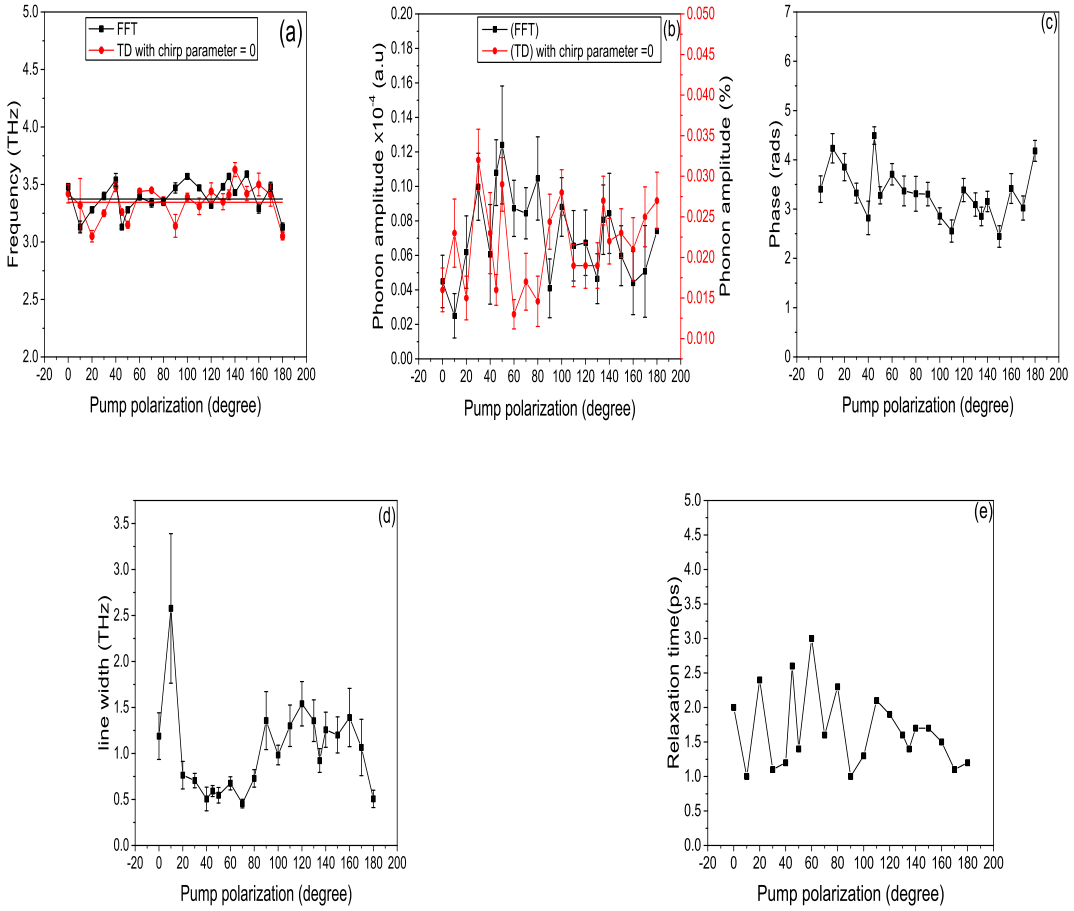

Figure 7.18.: The dependence of (a) frequency, (b) amplitude, (c) phase, (d) line width, and (e) relaxation time upon the pump polarisation are shown for R measurements made on the second GST/InAs (111) sample. The pump beam was incident nearly normal to the sample while the probe beam was incident at 45° and s-polarised. In (a) each black square represents the frequency value obtained by fitting a Lorentzian to the power spectrum, and the red circles represent the frequency values obtained by fitting the data to equation 5.32, with the chirp parameter set equal to zero, before subtracting the background. In (b) the black circles represent the amplitude values obtained by fitting a Lorentzian lineshape to the power spectra, while the red squares represent the amplitude values obtained from fits to equation 5.32 before subtracting the background. In (c) and (e) the black squares represent the phase and relaxation time values respectively obtained from fitting equation 5.32 to the data before subtracting the background and with the chirp parameter set equal to zero.

Figure 7.19 (a) shows a typical time resolved ellipticity signal obtained from the second GST/InAs(111) structure with an s-polarised probe beam, pump polarisation of 45° and pump fluence of 1.06 $\mathrm{mJ/cm^2}$. A large peak is observed around zero time delay, when the pump and probe overlap in time, due to the specular optical Kerr effect (SOKE). The SOKE peak has maximum amplitude when the pump and probe polarisations lie

$45°$ apart. The SOKE peak is followed by a heavily damped oscillation, with frequency that increases gradually with increasing time during the scan, and with a relaxation time of around 1.75ps. Figure 7.19 (b) shows the ellipticity signals obtained as the pump polarisation was varied. In Figure 7.19(c) the data is plotted without the initial peak in order to reveal the oscillatory component more clearly. The black curves were fitted with the chirp parameter set equal to zero. Figure 7.19(d) shows the oscillatory component after subtraction of a slowly varying background, with fitted curves for which the chirp parameter was allowed to vary. The power spectra obtained from the ellipticity signals are presented in figure 7.19 (e). The quality of the ellipticity data obtained from the second GST/InAs (111) sample appears somewhat worse than that obtained from the first sample. Figure 7.20 (a) shows the oscillation frequencies obtained from fitting a Lorentzian to the peak in the power spectrum, and fitting the time domain data with and without allowing for chirp. The frequencies obtained by these different methods are in good agreement. Indeed the frequency appears to be independent of pump polarisation with a frequency of 3.18 $\pm$ 0.03 THz for the FFT data, 3.03 $\pm$ 0.06 THz for the raw time domain data with chirp parameter set to zero and 3.06 $\pm$ 0.17 THz for the raw time domain data with the chirp parameter allowed to vary which corresponds to the instantaneous frequency at the beginning of the scan. The instantaneous frequency ω when the oscillations have just damped out, can again be estimated. Taking the difference of the frequency extracted from the power spectrum ω_{ps} and the instantaneous frequency at the beginning of the scan that extracted from the time domain fitting ω_{TD}, and adding it to the frequency extracted from the power spectrum ω_{ps} (i.e $\omega = (\omega_{ps} - \omega_{TD}) + \omega_{ps}$), we obtain a frequency of 3.3THz. Figure 7.20 (b) shows the phonon amplitude obtained using each of the three fitting methods. While there is quite a lot of scatter in the extracted values, the amplitude tends to be large for values of the pump orientation around 45° and 135°. Also the phase of oscillation, shown in figure 7.20 (c), seems to increase by π radians as the pump polarisation passes through $90°$. These last two observations suggest that the oscillatory response again has a SOKE-like dependence upon pump polarisation. The dependence of the line width, relaxation time and chirp upon pump polarisation are shown in figure 7.20 (d), (e) and

(f) respectively. The line width and the relaxation time show no clear dependence upon the pump polarisation. The values of the extracted chirp parameter show a great deal of scatter, perhaps due to the smaller signal to noise ratio for the present set of data.

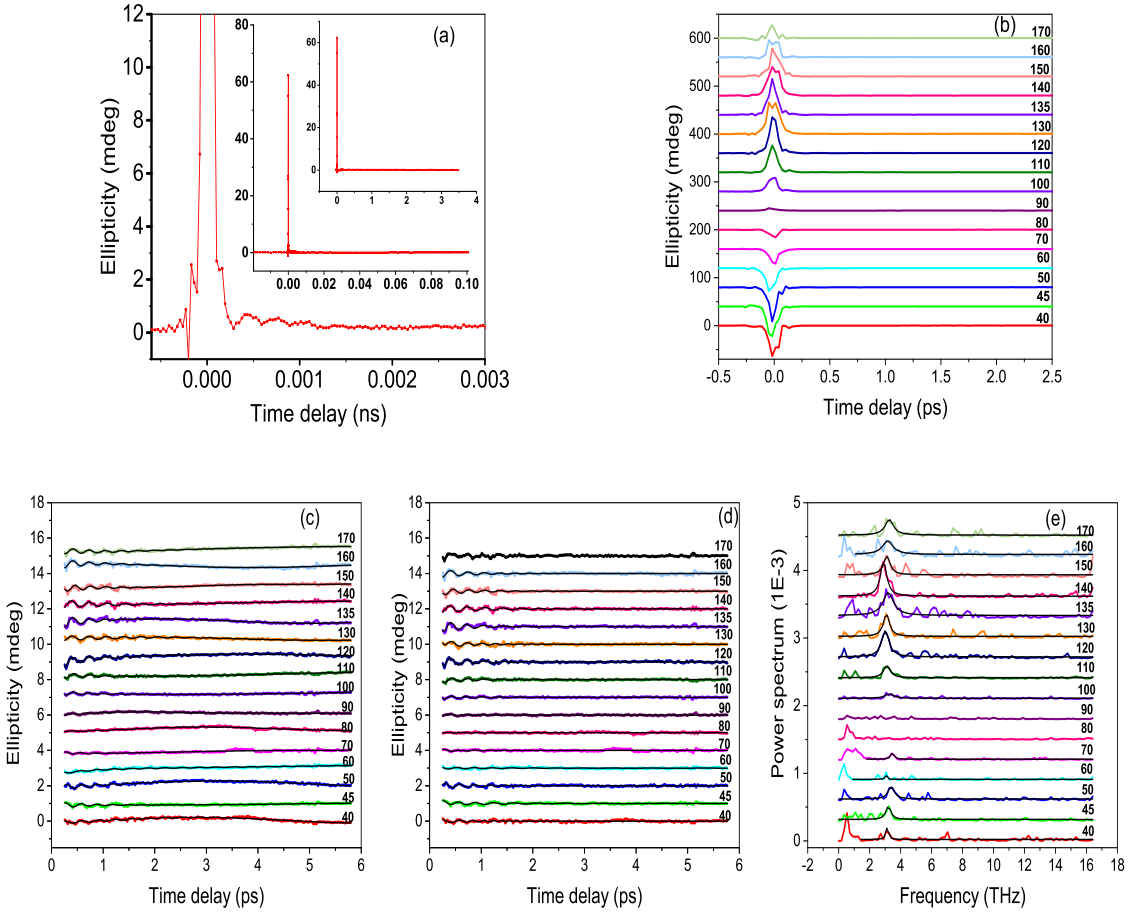

Figure 7.19.: Time resolved ellipticity signals obtained from the second GST/InAs (111) sample. The pump beam was applied normal to the sample while the probe beam was s-polarized and incident at $45°$. (a) Typical ellipticity signal for $45°$ pump polarisation, plotted on different timescales. (b) Ellipticity signals obtained for different pump polarisations. (c) Expanded view of ellipticity signals. (d) Oscillatory component of ellipticity signal after subtraction of background. (e) Power spectra obtained from the oscillatory components of the ellipticity signals in (d).

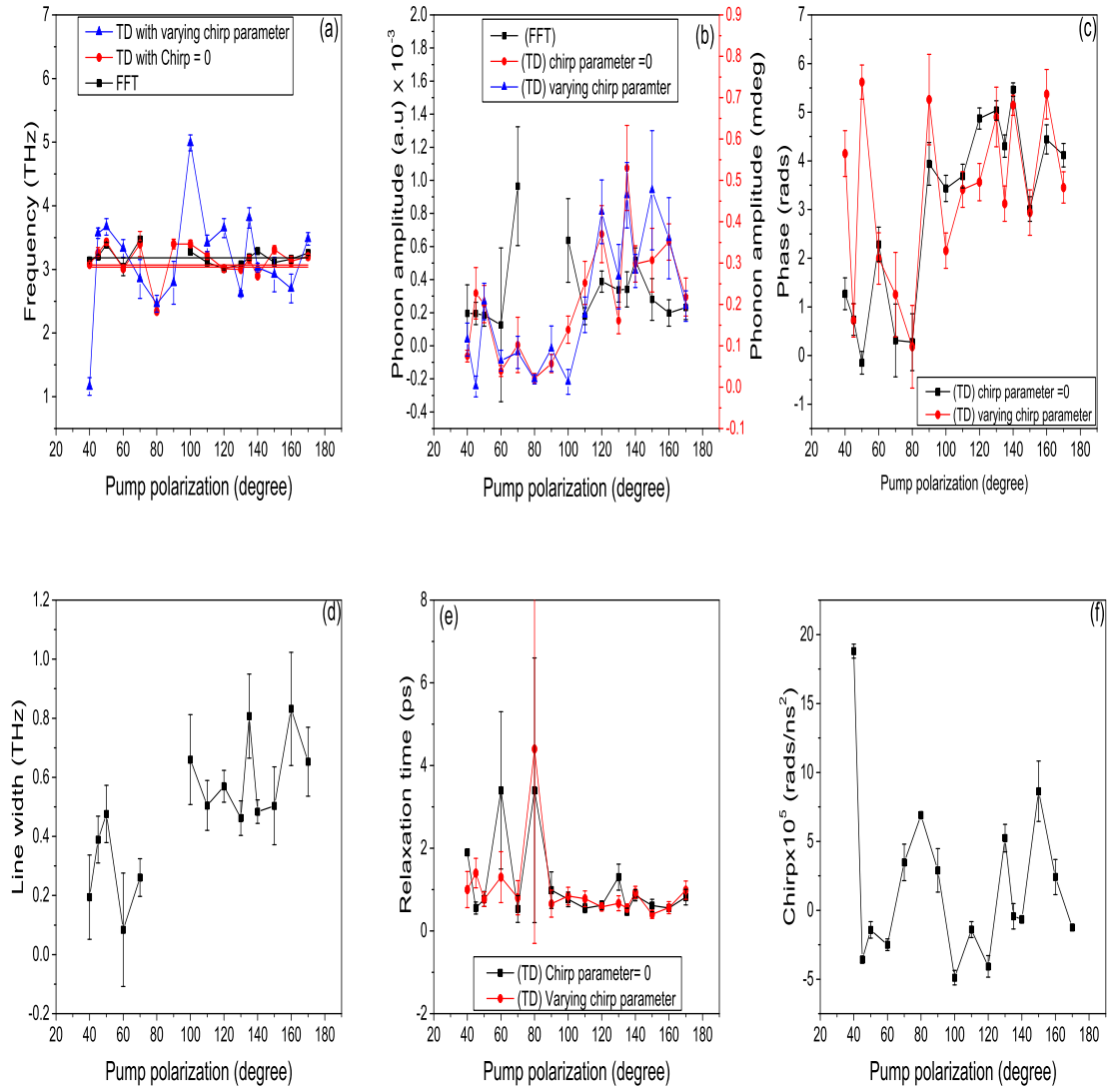

Figure 7.20.: The dependence of (a) frequency, (b) amplitude, (c) phase, (d) line width, (e) relaxation time, and (f) chirp parameter upon the pump polarisation are shown for ellipticity measurements made on the second GST/InAs (111) sample. The pump beam was at nearly normal incidence to the sample while the probe beam was incident at 45° and s-polarised. In (a) each black square represents the frequency value obtained by fitting a Lorentzian to the power spectrum, and the red circles represent the frequency values obtained by fitting the data to equation 5.32, with the chirp parameter set equal to zero and before subtracting the background, while the blue triangles represent the frequency values obtained from fits to equation 5.32 after subtracting the background and allowing the chirp parameter to vary. In (b) the black circles represent the amplitude values obtained by fitting a Lorentzian lineshape to the power spectra, while the red squares represent the amplitude values obtained from fits to equation 5.32 before subtracting the background, while blue triangles represent the amplitude values obtained from fits to equation 5.32 after subtracting the background from the data and allowing the chirp parameter to vary. In (c) and (e) the black circles represent the phase and relaxation time values respectively obtained from fitting equation 5.32 to the data before subtracting the background and with the chirp parameter set equal to zero, while the red circles represent the phase and relaxation time values obtained from fits to equation 5.32 after subtracting the background and allowing the chirp parameter to vary.

7.1.6. Dependence of the coherent optical phonon signal upon sample orientation for the second epitaxial GST/InAs(111) sample

Time resolved transient R and ellipticity signals were acquired from the second GST/InAs(111) structure with the pump and probe polarisations set $45°$ apart as the sample was rotated about its normal through $180°$ in $10°$ steps starting from $0°$. The pump beam was at near to normal incidence to the sample while the s-polarised probe beam was incident at $45°$ as shown in figure 7.21.

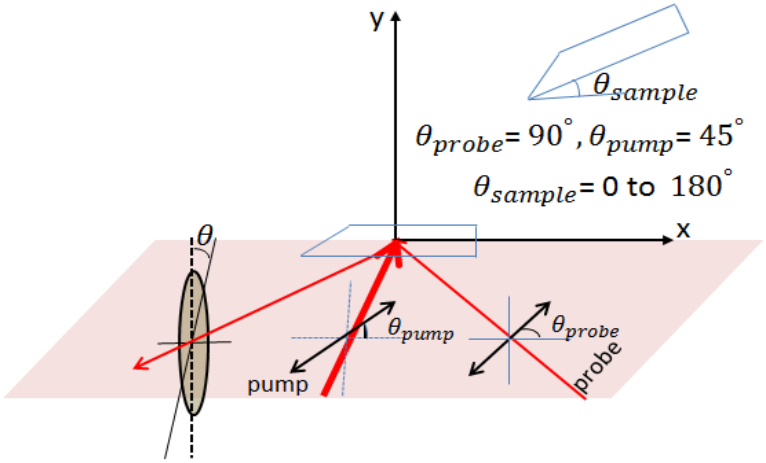

Figure 7.21.: Experimental configuration for studying the dependence of the sample response upon orientation of the second GST/InAs(111) sample

The quality of the ellipticity data is poor in this set of measurements as can be seen from figure 7.22. The transient R signals acquired simultaneously with the ellipticity data are shown in figure 7.23 (a). The power spectra obtained from the transient reflectivity signals from 0.1 ps onwards are shown in figure 7.23 (b). Figure 7.24 (a) shows the oscillation frequencies obtained firstly from fitting a Lorentzian curve to each power spectrum, and secondly by fitting the time domain data with the chirp parameter set equal to zero. The reflectivity signal contains an oscillation of frequency 3.32 $\pm$ 0.02 THz for FFT data and 3.37$\pm$ 0.02 THz for the raw time domain data and appears to be independent of sample orientation. The amplitudes of oscillation obtained from the two fitting methods are shown in figure 7.24(b). There is no clear dependence of the amplitude upon the orientation of the sample. Figure 7.24(c), (d), and (e) show the

line width, the relaxation time and the phase of oscillation, and again there is no clear dependence on the orientation of the sample.

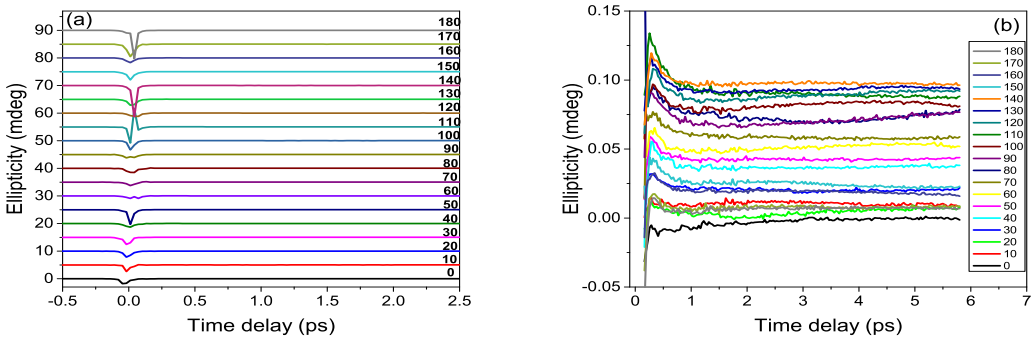

Figure 7.22.: Time resolved ellipticity signals obtained from the second the GST/InAs (111). The pump beam was applied at near normal incidence while the probe beam was s-polarized and incident at $45°$. (a) Ellipticity signals for different sample orientations. (b) Expanded view of ellipticity signals.

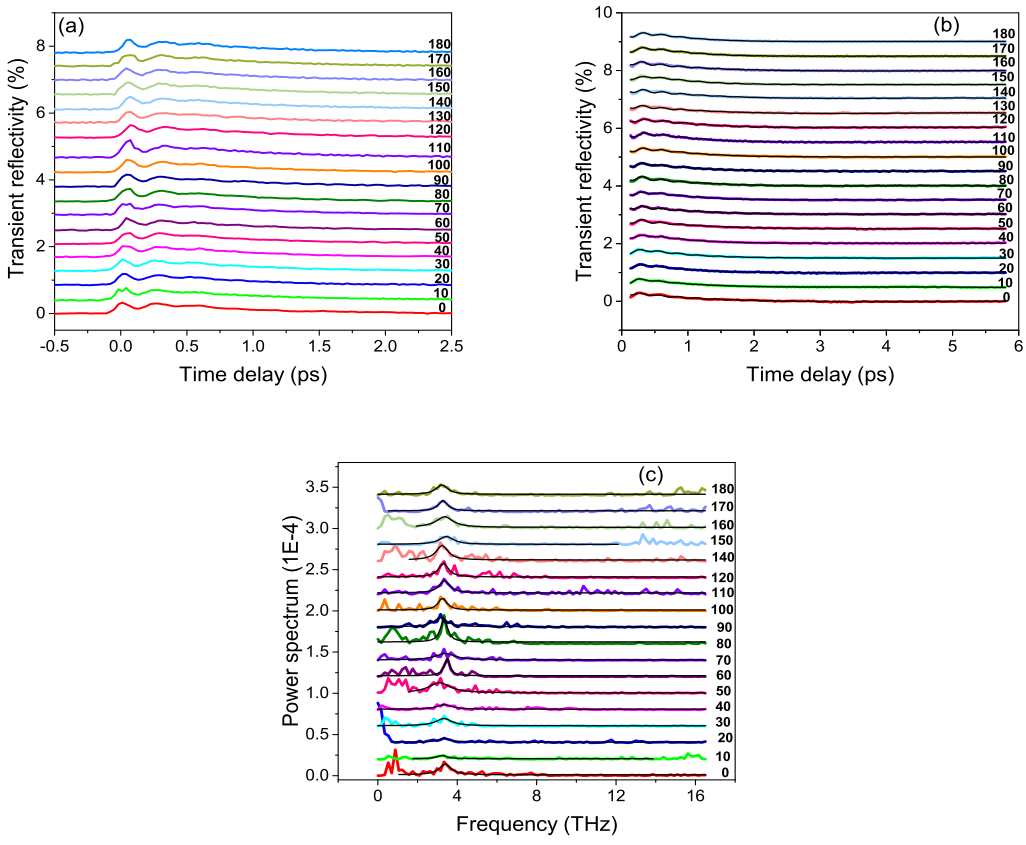

Figure 7.23.: Time resolved transient R signals obtained from the second GST/InAs (111) sample. The pump beam was at near normal incidence while the probe beam was s-polarized and incident at $45°$. (a) Transient R signals for different sample orientations. (b) Oscillatory component obtained from the transient R signal before subtracting the background. (c) Power spectra obtained from the transient R signal for different sample orientations.

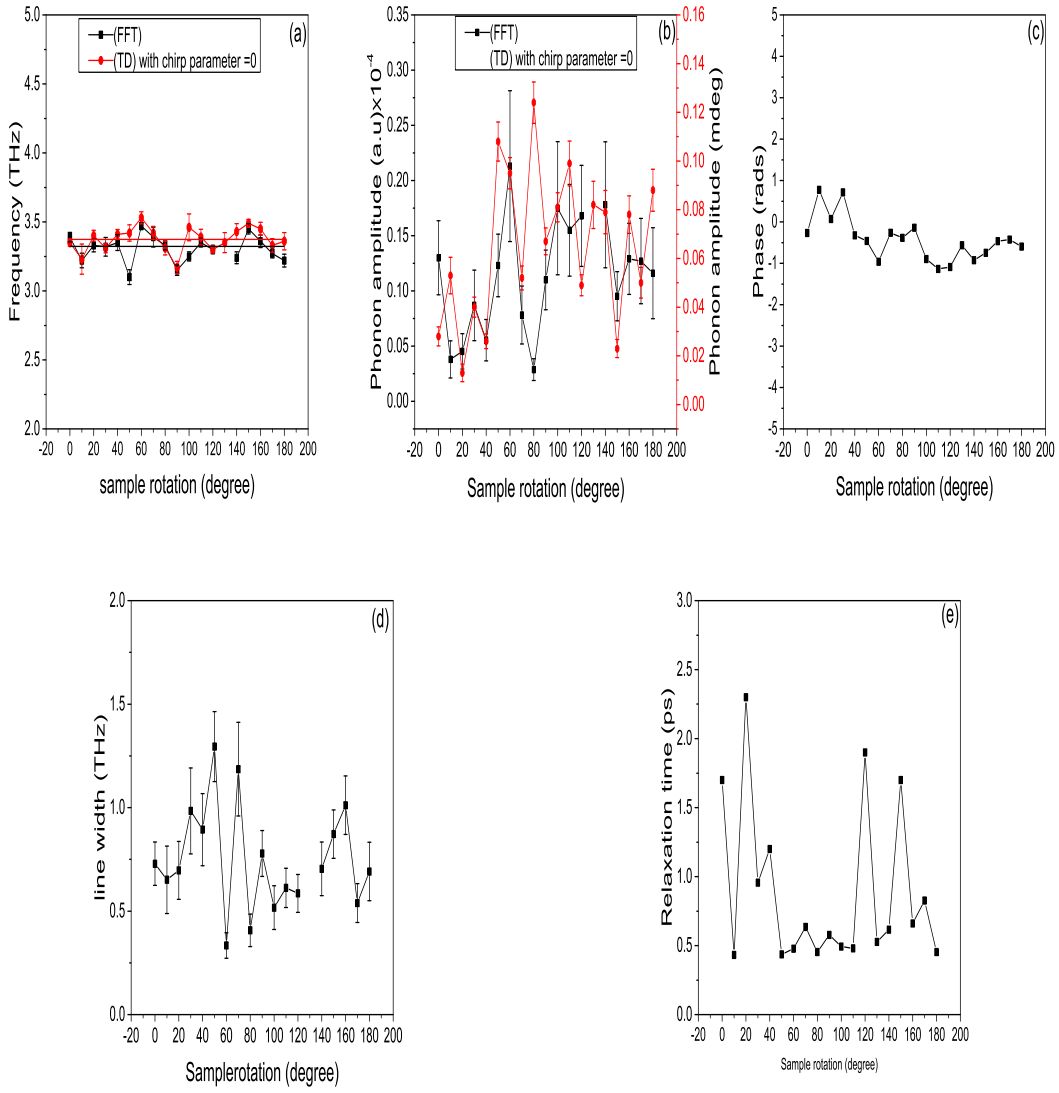

Figure 7.24.: The dependence of (a) frequency, (b) amplitude, (c) phase, (d) line width, and (e) relaxation time upon the pump polarisation are shown for measurements made on the second GST/InAs (111) sample. The pump beam was incident normal to the sample while the probe beam was incident at 45° and s-polarised. In (a) each black square represents the frequency value obtained by fitting a Lorentzian to the power spectrum, and the red circles represent the frequency values obtained by fitting the data to equation 5.32 before subtracting the background and before varying the chirp parameter. In (b) the black circles represent the amplitude values obtained by fitting a Lorentzian lineshape to the power spectra, while the red squares represent the amplitude values obtained from fits to equation 5.32 before subtracting the background and before varying the chirp parameter.

7.1.7. Dependence of the coherent optical phonon signal upon pump fluence for the second epitaxial GST(111) sample

The transient R and ellipticity signals obtained from the second GST/InAs(111) samples at reduced fluence after exposure to elevated pump fluence are shown in figure 7.26 . The measurements were made with the pump and probe polarisations set 45° apart. The pump beam was applied close to normal to the sample with fixed polarisation of 45^{0} while the probe beam was incident at 45° to the normal with fixed s-polarisation as shown in figure 7.25. The measurements performed at elevated pump fluence showed no oscillation and therefore have not been presented.

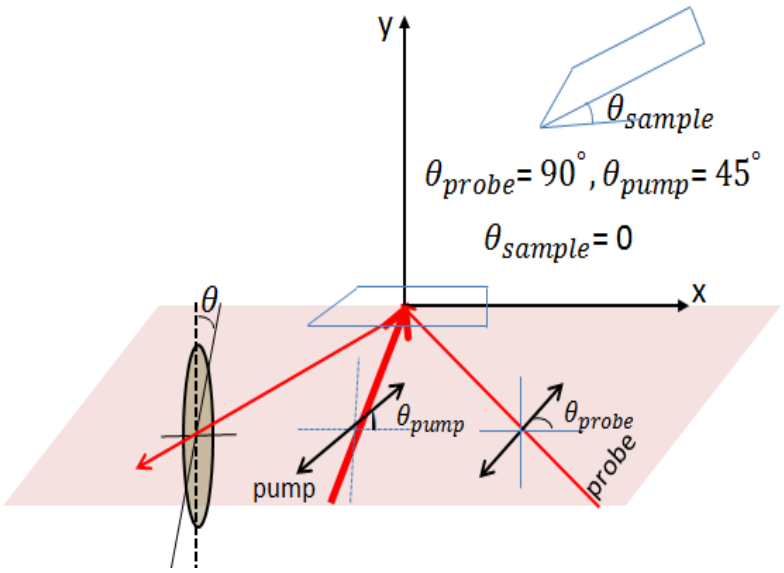

Figure 7.25.: Experimental configuration for studying sample response to changing pump fluence for the seccond GST/InAs(111) sample.

The measurements reveal that there is little change in the transient ellipticity and reflectivity signals due to exposure to elevated pump fluence. This investigation implies no structural change has occured within the material.

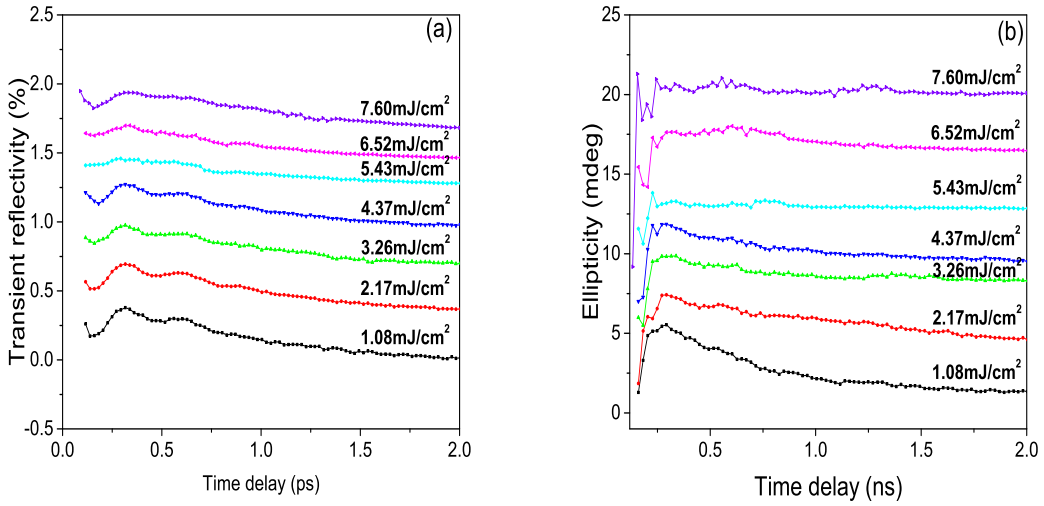

Figure 7.26.: Transient reflectivity (a) and ellipticity (b) signals after exposure to elevated pump fluence. The pump beam was incident normal to the sample while the probe beam was incident at 45° and s-polarised. Measurements were made at a fluence of 1.08 $\mathrm{mJ/cm^2}$.

7.2. Raman spectra of GST/InAs(111) samples

Raman spectra were acquired from the GST/InAs(111) samples using the same Raman spectroscopy system used to study the InAs(111) wafer. The Raman spectra of the first and the second GST/InAs(111) samples that were grown in the same lab are shown in figure 7.27. The Raman spectrum of the first GST/InAs(111) sample contains a broad band between 100 and 200 $\mathrm{cm^{-1}}$ with three different peaks about 122.3$\mathrm{cm^{-1}}$ (3.7 $\pm$ 0.001 THz), 139$\mathrm{cm^{-1}}$ (4.2 $\pm$ 0.003 THz) and 151.43$\mathrm{cm^{-1}}$ (4.6 $\pm$ 0.076 THz). The additional peak at 216.4$\mathrm{cm^{-1}}$ (6.5 THz) was observed previously for the InAs(111) sample and attributed to the InAs zone centre TO phonon. The Raman spectrum of the second GST/InAs(111) sample shows a broad band between 100 and 275 $\mathrm{cm^{-1}}$ again with three peaks at about 116.17$\mathrm{cm^{-1}}$ (3.4 $\pm$ 0.007 THz), 144.8$\mathrm{cm^{-1}}$ (4.3 $\pm$ 0.020 THz) and 185.57$\mathrm{cm^{-1}}$ (5.6 $\pm$ 0.26 THz). However the TO phonon of the InAs substrate is not observed. From the Raman spectra of the two GST/InAs (111) samples we can say that at least three peaks appear to be associated with the GST in each sample. The first two peaks are identical placed, while the third one appeared at different frequencies for both samples.

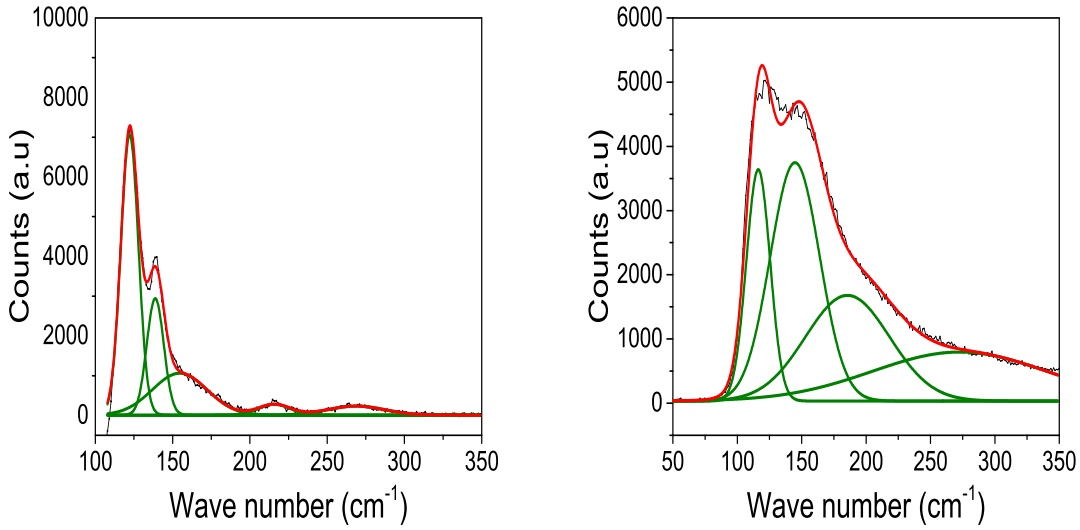

(a) Raman spectrum of first GST/InAs (111) (b) Raman spectrum of second GST/InAs (111)

Figure 7.27.: The multipeak fitting of the Raman spectra of the GST/InAs(111) samples

The Raman spectra of both GST/InAs(111) samples are similar to those found in the literature [111, 112, 113, 81, 114, 115, 106]. The results can be compared and contrasted with those obtained previously for GST films of (100) orientation [106]. In that study two optical phonons were observed, one at 3.4 THz and the other at 4.5 THz. One possibility of the appearance of the third peaks at 4.6 and 5.6 THz in the two GST/InAs(111) samples is due to orientational dependence of the epitaxial growth, and the difference in the frequency is possibly due to microscopic structural differences such as the temperature and growth conditions. The lowest frequency mode in each GST/InAs(111) sample was also observed in the pump-probe measurements as explained above, while the next two phonon modes, in terms of increasing frequency, did not appear, most likely because they are not observable on grounds of symmetry as discussed in the theory of TSRS that was presented previously. The first mode that observed in Raman measurements was attributed to the vibration of the heteropolar bond in the tetrahedral GeTe4 and/or pyramidal SbTe3 and the second mode was attributed to Sb-Sb vibrations [111, 112].

7.3. Discussion

As explained before, GST crystallizes into a metastable rock salt-like structure with Te atoms occupying the anion sites. The cation sites are occupied by Ge, Sb and vacancies. The ideal rock-salt structure has a centre of inversion symmetry and its point group is O_h with five irreducible representations denoted as $2A$, E and $2T$ [107]. Rocksalt structure only has T_2 optical phonon at the zone center but not Raman active [6, 107].

Table (7.1) compares the phonon frequencies extracted from the two GST/InAs(111) samples. These include the frequencies obtained from R and ellipticity signals as the pump polarisation, sample orientation and pump fluence were varied, as well as those obtained from Raman measurements. Furthermore the table shows the frequencies extracted from the pump-probe measurements by four different methods. The first frequency corresponds to the centre of the peak observed in the power spectrum obtained from the FFT of the time domain data. The second frequency was obtained by fitting the raw time domain data to equation 5.20 with the chirp parameter set equal to zero. This should yield the average frequency of oscillation and thus be comparable to the value obtained from the FFT. The third value is obtained by fitting to equation 5.20 with the chirp as a variable parameter. In light of the form of equation 5.20, this effectively reports the instantaneous frequency at the beginning of the scan, immediately after excitation by the pump. Finally, based upon the chirped fitting an extrapolated frequency value is stated that corresponds to the frequency at the end of the oscillation ω that is equal to adding the difference between the instantaneous frequency at the beginning of the scan that extracted from the time domain fitting ω_{TD} and the frequency extracted from the FFT $\omega_{ps}$to the value of the frequency extracted from the FFT ω_{ps} (i.e $\omega = (\omega_{ps} - \omega_{TD}) + \omega_{ps}$) which is approximately equal to 3.4THz.

Let us consider the differences that exist between the different frequencies shown in Table 7.1. For the first GST/InAs(111) sample the frequency values extracted from the ellipticity signals are somewhat lower in measurements in which the pump polarisation was varied as compared to those in which the sample orientation was varied. This difference in frequency may result from a difference in the accuracy with which the

pump and probe spots were focused and overlapped leading to a difference in the pump fluence at the position of the probe spot. The alignment is expected to be worse for the measurements in which the sample is rotated because it is difficult to guarantee that the spots are incident upon the centre of rotation and there is a small but finite wobble in the rotation of the sample stage. This would in turn lead to a difference in the maximum transient temperature experienced by the sample in each case. A higher temperature in the pump polarisation experiments would lead to greater softening of the lattice and hence a lower frequency as observed.

For the second sample, the frequencies obtained from simultaneous R and ellipticity measurements are different by more than the error values reported by the fitting algorithm. The most likely explanation is that the oscillations in the R and ellipticity measurements sit upon different backgrounds that vary rapidly with time at short time delays where the oscillation amplitude is largest and has greatest effect upon the fitted frequency. It is difficult to remove this background and so it is likely to skew the fitted values somewhat.

The chirp also appears to be smaller for ellipticity signals obtained from the second sample compared to those obtained from the first sample. This may be because the signal to noise ratio was inferior for the second sample. In fact the phonon frequencies extracted for the second sample are consistently higher by 0.1 -0.2 THz compared to those extracted for the first sample, and oscillations were observed in the R signal from the second sample but not the first . These facts point to structural differences between the two samples.

The frequencies of the lowest lying modes in the Raman measurements were 3.7 THz for the first sample and 3.4THz for the second sample. Both values are larger than those extracted from the pump-probe measurements. This is probably because the pump-probe measurements are made at a higher temperature due to the heating by the pump, which causes softening of the lattice and a reduction of phonon frequency. The pump-probe measurements also yielded a higher frequency for the second sample than for the first sample in contrast to the Raman measurements. We note that these modes lie close to the edge of a high-pass filter designed to block elastically scattered light within the Raman measurements. Therefore it is possible that the filter introduces some

asymmetry into the shape of the lowest lying mode and hence also a small shift in its apparent frequency. The fitting of the Raman data is also complicated by the presence of multiple modes and the need to subtract a background from the raw data. The Raman measurements reveal additional modes at around 4.2 and 4.6 THz for the first sample and around 4.3 and 5.6 THz for the second sample that were not observed in pump-probe measurements. This is not surprising since, as discussed previously, the selection rules for the pump-probe and Raman measurements are expected to be different .

Based on the (TSRS) theory the appearance of a mode with 3.4 THz frequency in both transient R and AR (ellipticity) signals for one of the samples suggests a three-dimensional T_2 -like mode of the GST/InAs (111) structure. The ordering of vacancies within the GST and the displacement of ions from their positions in the ideal rock-salt structure may remove the inversion symmetry, allowing first order Raman scattering and also excitation of COPs by TSRS. In this case the GST/InAs(111) structure is a rock-salt like structure and has a T_2 -like phonon mode.

A phonon with frequency of 3.4 THz has been observed in the R signal in previous studies of amorphous and polycrystalline GST [77, 116] and assigned A_{1g} character. The (TSRS) theory predicts that in pump-probe experiments performed on either the (111) and (001) surface of a cubic structure, A and E type phonons can be observed only in the R signal, but not in the AR signal, and without any dependence on pump or probe polarizations.

TSRS theory was successfully applied in a previous study of GST/GaSb(001) [12]. Two optical phonons were observed in the AR signal: a mode at 3.4 THz belonging to the GST layer and another mode at 6.7 THz belonging to the GaSb substrate. From table 3.1, the theory predicts that, for the (001) surface of zincblende or rocksalt, only the A and E modes should be observed in the R signal, with no dependence upon pump and probe polarization. Only the T_{2z} mode should be observed in the AR signal with amplitude proportional to $\sin(2\theta)\cos(2\phi)$, where θ and ϕ are defined relative to an in-plane cube edge. A long lived oscillation exhibiting this angular dependence was indeed observed and attributed to a T_{2z} – like mode of the defective GST structure. For InAs (111), where we always excite a superposition of T_{2x}, T_{2y}, and T_{2z} modes, long lived

oscillations are observed. However, for the GST/InAs(111) samples, the oscillations are heavily damped and strongly chirped, so that the frequency increases with time. The heavy damping may occur because GST has a defective structure in which the degeneracy of the T_{2x}, T_{2y}, and T_{2z} modes is lifted. Since the pump excites a superposition of these T_{2x}, T_{2y}, and T_{2z} phonons, any splitting of their frequencies will lead to dephasing within the measured signals i.e. after a few periods of oscillation the three modes will begin to interfere with each other destructively, giving the appearance of an enhanced damping.

The observation of a 3.4 THz mode in the R and AR signals for GST/InAs (111) samples points to a T_2-like character. The amplitude of the mode extracted from the R signal exhibits no dependence upon the pump polarisation, just as the TSRS predicts for a superposition of T_2– like modes. However the amplitude of the mode extracted from the AR signal has a strong dependence upon the pump and probe polarisation, which is similar to that expected for the SOKE, but which is again fully consistent with the predictions of the TSRS theory. The amplitude of the T_2 -like mode is almost zero when the polarisations of the pump and probe are parallel or perpendicular, suggesting that the SSC mechanism does not contribute to the mode excitation. The absorption coefficient for 800nm beam for metastable GST is around $10^8 m^{-1}$ as in figure 4.3. As a result, for GST sample with thickness of 20 and 22 nm the intensity of the incident light at the substrate (InAs) is less by approximately 90% to the intensity of the incident light at GST sample. That leads to low phonon amplitude for the InAs sample which is difficult to detect by low intensity probe beam.

Exposure of the first GST/InAs (111) to high pump fluence resulted in changes in the frequency and the amplitude of the observed phonon, suggesting that a structural change had appeared within the GST structure, particularly since similar changes were not observed for the InAs(111) sample .

Table 7.1.: Comparison between pump-probe and Raman frequencies (in THz) obtained from two GST/InAs(111) samples

Experiment	Measurement	Signal	Frequency of the first GST/InAs(111)				Frequency of the second GST/InAs(111)			
			The power spectrum (FFT)	Time domain (chirp = 0)	Time domain (varying chirp)	when the oscillation is damped	The power spectrum (FFT)	Time domain (chirp = 0)	Time domain (varying chirp)	when the oscillation is damped
Pump-probe	Pump polarisation	Ellipticity	2.897 ± 0.025	2.925 ± 0.017	2.380 ± 0.073	3.41	3.18 ± 0.03	3.03 ± 0.06	3.06 ± 0.17	3.3
		Reflectivity	—	—	—	—	3.37 ± 0.03	3.34 ± 0.03		
	Sample orientation	Ellipticity	3.12 ± 0.02	3.00 ± 0.02	2.76 ± 0.06	3.48	—	—	—	—
		Reflectivity	—	—	—	—	3.32 ± 0.02	3.37 ± 0.02		
	Pump fluence	Ellipticity	3.516 ± 0.004				—			
		Reflectivity	3.513 ± 0.001				—			
Raman spectra	Frequency		3.7 ± 0.001				3.4 ± 0.007			
			4.2 ± 0.003				4.3 ± 0.020			
			4.6 ± 0.076				5.6 ± 0.26			

7.4. Summary

Time resolved transient reflectivity and ellipticity response on pump, probe, and sample orientations are performed on two epitaxial GST/InAs(111) samples. Clear oscillations of frequency of 3.4 THz are observed in the ellipticity signals obtained from the first and the second samples and are observed only in the reflectivity signal of the second GST/InAs(111) sample. According to TSRS theory, the appearance of a mode with 3.4 THz in both reflectivity and ellipticity signals for one sample suggests a three-dimensional T_2-like mode of the GST/InAs (111) structure. The insensitivity of the phonon amplitude obtained from the reflectivity signal to the pump polarisation and sinusoidal dependence of the phonon amplitude obtained from the ellipticity signals upon the pump polarisation that similar to the SOKE dependence on pump and probe polarisation suggest the excitation of the T_2-like mode by ISRS mechanism without any contributions from SSC mechanism.

The oscillations observed in the GST/InAs (111) samples are heavily damped and strongly chirped. The reason behind that is due to excite a superposition of T_{2x}, T_{2y}, and T_{2z} phonons, and degeneracy of the three phonons due to some structural distortion, then the dephasing of modes of similar but different frequency may leads to decreasing in the phonon amplitude.

Raman spectra performed on GST/InAs (111) samples reveal the optical phonon that are observed in pump-probe measurements in addition two other optical phonon modes that were not observed in pump-probe measurements. The change in the phonon amplitude and the phase after exposure the first GST/InAs (111) to elevated pump fluence implies that a structural change took place.

8. Summary and Future Work

8.1. Summary

Phase change materials such as $Ge_2Sb_2Te_5$ (GST) possess interesting properties that make them ideally suited for technological applications such as optical storage and phase change random access memory. They switch between amorphous and crystalline phases rapidly when excited by light or electric current. Improved understanding of the microscopic dynamics of phase change materials is critical for the further development of applications. In this dissertation, I studied coherent optical phonons within epitaxial GST/InAs(111) samples and reference InAs(111) substrates, by ultrafast optical pump-probe measurements, paying particular attention to the mechanisms by which the coherent phonons are excited. The properties of the coherent optical phonons and their excitation mechanisms have been analysed by applying microscopic and macroscopic Raman theories as well as a theory of transient stimulated Raman scattering (TSRS) based upon use of the Raman tensor.

One way of investigating these optical phonons is to use an optical pump-probe technique designed to detect changes in the reflectivity and ellipticity of the reflected probe beam with femtosecond resolution. The dynamic response includes information about the sample structure and the phase transition process within the phase change materials.

Time resolved pump-probe measurements of an InAs(111) wafer and two GST/InAs(111) samples were presented in chapters 6 and 7 respectively. The ellipticity response of all three samples shows a clear peak due to the specular optical effect (SOKE) peak at zero time delay, with amplitude depending on the relative polarisation of pump and probe beams. The SOKE peak is observed to have maximum amplitude when the pump

and probe polarisation are set 45° apart; and zero amplitude when they are set parallel or perpendicular to each other. The SOKE peak provides information about the rate of relaxation of the electron momentum. The SOKE peak is accompanied by long lived oscillations for the InAs(111) wafer and heavily damped oscillations for the two GST/InAs(111) samples, in each case superimposed on a relaxation background. The long-lived oscillation for the InAs (111) wafer corresponds to a coherent optical phonon with frequency of 6.5 THz, while the heavily damped oscillations observed for the two GST/InAs(111) samples correspond to coherent optical phonons with frequencies in the range of 2.9-3.4 THz. The frequencies of the optical phonons extracted from the ellipticity response are insensitive to the pump polarisation and the sample orientation. On the other hand, the amplitudes show a SOKE-like dependence upon the pump polarisation but are found to be insensitive to the sample orientation. The transient reflectivity response was measured simultaneously with the ellipticity response and was found to give a clear oscillation with frequency of 3.4 THz for only the second GST/InAs (111) sample, and no clear oscillations for the first GST/InAs(111) and InAs(111) samples. The frequency and amplitude of the optical phonon mode of the second GST/InAs(111) sample extracted from the reflectivity signal were found to be insensitive to the relative polarisation of the pump and probe beams and to rotation of the sample about it is normal. The phonon frequency extracted from the ellipticity signals was slightly higher for the second GST/InAs(111) sample than for the first sample which may attributed to structural differences between the two GST/InAs(111) samples.

The behaviour of the optical phonons modes extracted from the ellipticity and reflectivity response was interpreted by understanding the Raman tensor and phonon representations of the zinc blend and rock-salt structures within the framework of TSRS theory. The point group of InAs is T_d while that of NaCl is O_h, and both have irreducible representations denoted as A_1, A_2, E, $T_1$and T_2 . Both structures have a three dimensional optical phonon mode denoted as T_2. This optical T_2 mode is Raman active in zinc blend and Raman inactive in rock-salt. TSRS theory based on the Raman tensor describes the observation of A, E, and T phonon modes and their dependence on pump and probe polarisation. The TSRS theory predicts that, for a (111) surface of a cubic

crystal, one dimensional A and two dimensional E phonon modes can be observed in the reflectivity signal without any dependence on pump and probe polarisation. However, a three dimensional T_2 phonon mode can be observed in both reflectivity and ellipticity signals with amplitude that has a $\sin(2(\theta-\phi))$ dependence upon the orientation of the pump electric field, θ and probe electric field, ϕ within the plane of the sample. The experiments show that the phonon amplitude, extracted from ellipticity signals of the InAs(111) wafer and both GST/InAs(111) samples, has a $\sin(2(\theta-\phi))$ dependence on the pump and probe polarisation. This behaviour is characteristic of the specular optical Kerr effect (SOKE) but in fact confirms that the coherent optical phonons in InAs(111) and GST/InAs (111) are excited by an impulsive stimulated Raman scattering mechanism (ISRS). The TSRS theory confirms that the 6.5 THz optical phonon mode in InAs(111) is a three dimensional T_2 phonon mode, and suggests that the 3.4 THz optical phonon observed in the transient ellipticity signals of the two epitaxial GST/InAs (111) samples, and only in the reflectivity signal of the second epitaxial GST/InAs(111) sample, is also a three dimensional T_2 -like phonon mode. GST has a rock-salt like structure with approximately 20% vacancies at the Ge and Sb sites. The existence of vacancies and the displacement of ions from their positions in the rock salt structure leads to a lack of inversion symmetry, causing the $\sim$3.4 THz coherent optical phonon to become Raman active with underlying three dimensional, T_2 –like character. The observation of the T_2 -like phonon mode confirms that the underlying crystallographic structure of GST is essentially cubic.

The oscillations observed in the GST/InAs (111) samples are heavily damped and strongly chirped, so that the frequency increases with time. The TSRS theory predicts that, for a (111) plane of a cubic system, the T_{2x}, T_{2y}, and T_{2z} modes can be observed in both reflectivity and anisotropic reflectivity signals. If we excite a superposition of T_{2x}, T_{2y}, and T_{2z} phonons, and if the degeneracy of the three phonons is lifted by some structural distortion, then the dephasing of modes of similar but different frequency may have the appearance of an enhanced damping.

Based on calculations of Raman selection rules for normal incidence backscattering from the (111) plane of the zinc blend structure, transverse and longitudinal optical phonons

should be observed in the InAs(111) sample. Raman measurements performed on InAs (111) agree with the calculations and reveal that it is the transverse optical phonon that is observed in pump-probe measurements. The Raman measurements also reveal other longitudinal and surface optical phonons that were not observed in pump-probe measurements. Raman spectra obtained from the GST/InAs (111) samples reveal the optical phonon that is observed in pump-probe measurements in addition to two other optical phonon modes that were not observed in pump-probe measurements. There is a small difference in the phonon frequency observed in Raman and pump-probe measurements that is attributed to the difference in the sample temperature during the measurements. The two additional phonon modes observed in the Raman measurement did not appear in the pump-probe measurements, most likely because of the different selection rules applying to each type of measurement.

The dependence of the ellipticity and reflectivity response upon elevated pump fluence was studied for both the InAs(111) wafer and the two epitaxial GST/InAs(111) samples. A measurement was made at high pump fluence then immediately repeated for the same sample position at lower pump fluence. The amplitude and phase of the 6.5 THz optical phonon of the InAs (111) wafer was found to be unaffected by increasing the pump fluence, which implies that no structural change took place. However the 3.4 THz optical phonon of the first epitaxial GST/InAs (111) sample was observed to shift to higher frequency. In addition, a variation in the phonon amplitude and phase took place with increasing pump fluence that suggests a change in the sample structure. For the second epitaxial GST/InAs (111) sample, the measurements revealed little change in the transient ellipticity and reflectivity signals due to exposure to elevated pump fluence. This suggests that no structural change occurred within the second sample. The differences observed between the first and second samples may be due to differences in the thermal conductance of the two sample structures.

8.2. Future Work

Time resolved ellipticity and reflectivity were measured for two epitaxial GST/InAs(111) samples. To the best of our knowledge, this is the first time that a three dimensional optical phonon mode of GST has been excited by the ISRS mechanism. A previous study of the coherent optical phonons of GST/GaSb(001) concluded that the phonon amplitude was insensitive to the pump polarisation, which suggested that the T_2-like phonon mode was excited by a surface space charge. To obtain a clearer picture of the phonon excitation mechanism, more experiments could be performed to study the coherent optical phonons of epitaxial GST grown with a different orientation e.g. (110).

We studied how the transient ellipticity of two GST/InAs(111) samples depends upon exposure to increased pump fluence. Only the first sample showed an irreversible change in phonon frequency and amplitude, which suggested that a structural change had taken place. At the same time, Raman measurements revealed a difference in the phonon frequencies exhibited by the two samples, and in particular we observed a phonon mode associated with the InAs substrate in the spectrum of the first GST/InAs(111) only. Taken together these observations suggest a strong sensitivity of the phonon spectra to the details of the sample stack, which might influence the observability of certain modes and also the thermal conductance that plays a key role in mediating pump-induced structural changes. It would therefore be very interesting to study more GST/InAs(111) structures in which the thicknesses of an InAs epilayer, the GST layer and an additional capping layer are varied in a systematic manner.

We also observed that there was a difference in the phonon frequencies extracted from Raman measurements relative to those extracted from pump-probe measurements for the GST/InAs(111) samples, presumably due to the different sample temperature during each type of measurement. It would therefore be useful to study the phonon frequency in pump-probe experiments at lower pump fluence (less than $1\mathrm{mJ/cm^2}$) so as to make more direct comparison with Raman measurements. In addition more observations of the phonon amplitude at smaller and larger pump fluence are needed to understand whether or not the phonon amplitude depends linearly upon the pump fluence, and whether larger

amplitudes can lead to a phase transition.

Raman spectra obtained from InAs(111) and GST/InAs(111) samples revealed three different optical phonons for each sample while the pump-probe measurements observed just one phonon mode for each sample. The reasons for the different selection rules for the two measurement techniques are not clear, and therefore a more detailed TSRS theory is needed that distinguishes between TO and LO modes.

In our pump-probe measurement, we suggested that the phonon oscillations were heavily damped due to structural distortion of the GST that lifted the degeneracy of the three T_{2x}, T_{2y}, and T_{2z} excited phonons. To obtain a clear understanding of this point, more measurements of the phonon properties of epitaxial GST grown with the same (111) orientation, but on different substrates with a different degree of lattice mis-match, are needed.

A. Appendix

Symmetry operations and Group theory:

Symmetry is when a shape looks exactly the same after being inverted, reflected or rotated.

Symmetry operations and symmetry elements:

A symmetry operation is an operation that leaves an object in a configuration that is indistinguishable from its original configuration.

Each symmetry operation has a corresponding symmetry element which is a point, axes, line or plane. The symmetry element contains all the points that do not change their position as the symmetry operation is carried out.

The molecular symmetry operations of molecules:

1- E- The identity: it means doing nothing, and every molecule has at least this operation.

2- C_n- an n fold axis of rotation: rotating the molecule by $\frac{2\pi}{n}$ radians leaves it unchanged, where n is an integer. Some molecules have more than one axis of rotational symmetry. The axis with the highest value of n is called the principle axis.

3- σ- a plane of symmetry: reflection in the plane leaves the molecule looking the same.

4- i- a centre of symmetry: inversion through the centre of symmetry leaves the molecule unchanged.

5- S_n- an n fold improper axis (rotary – reflection axis): it involves rotating the molecule through $\frac{2\pi}{n}$ radian about the axis, followed by reflection in a plane perpendicular to the axis.

Symmetry classification of molecular- point groups:

Point groups are a means of classifying molecules according to their symmetry elements. They are called point groups because there is at least on point in the space that remains unchanged under the applied symmetry operations.

Table (A) shows the molecular point groups:

Point groups	Characteristic symmetry elements
C_n	Involves the identity E and an n-fold of axis of rotation
C_i	Involves the identity and a centre of inversion i
C_s	Involves the identity E and a plane of reflection
C_{nv}	Involves the identity E, an n-fold axis of rotation and n vertical mirror planes σ_v
C_{nh}	Involves the identity E, an n-fold axis of rotation and n horizontal mirror planes σ_h
D_n	Involves the identity E, an n-fold axis of rotation and n 2-fold rotations about axes perpendicular to the principal axis.
D_{nh}	Involves the same symmetry elements as $D_n$with the addition of a horizontal mirror plane
D_{nd}	Involves the same symmetry elements as $D_n$with the addition of n dihedral mirror planes
S_n	Involves the identity and one S_n
T_d	Involves all the symmetry elements of a regular tetrahedron including the identity, $4C_3$ axes, $3C_2$ axes, 6 dihedral mirror planes and $3S_4$axes
T	Involves the same symmetry elements as T_d except planes of reflection
T_h	Involves the same symmetry elements as T and in addition to contains a centre of inversion
O_h	The group of the regular octahedron
O	As for O_h but with no planes of reflection

Table A.1.: Molecular point groups

The transformation matrix:

The transformation matrix is the matrix which used to map one set of coordinates or functions to another. Accordingly the transformation matrix can represent the effect of a symmetry operation such as a rotation on coordination system (x,y,z). For example the axes x,y and z are transformed to $x`$,$y`$ and $z`$ with $x` = x$, $y` = z$ and $z` = -y$ under four-fold rotation about the x axis. The transformation can be represented by the matrix M as

$$\mathrm{M} = \begin{bmatrix} 1 & 0 & 0 \\ 0 & 0 & 1 \\ 0 & -1 & 0 \end{bmatrix}.$$

In the group theory, the transformation matrix is used to perform the symmetry operations of the molecules. The transformation matrix that used to perform the identity, reflection and rotation operations on a vector (x,y) are:

1- The identity operation:

The identity operation leaves the vector unchanged, and the appropriate matrix is the identity matrix

$$(x, y) \begin{pmatrix} 1 & 0 \\ 0 & 1 \end{pmatrix} = (x, y)$$

2- Reflection operation:

For example a rotation of the (x, y) vector about the x axis, i.e y transforms $-y$.

$$(x, y) \begin{pmatrix} 1 & 0 \\ 0 & -1 \end{pmatrix} = (x, -y)$$

3- Rotation operation:

In two dimensions, the transformation matrix that represents a rotation by an angle θ about the origin is

$$R(\theta) = \begin{pmatrix} \cos\theta & -\sin\theta \\ \sin\theta & \cos\theta \end{pmatrix}$$

In three dimensions, the transformation matrices that represent a rotation around the x, y and z axes are:

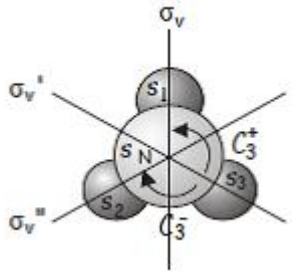

Figure A.1.: The basis set and the symmetry operations of the C_{3v} point group of the ammonia molecule

$$R_x(\theta) = \begin{pmatrix} 1 & 0 & 0 \\ 0 & \cos\theta & -\sin\theta \\ 0 & \sin\theta & \cos\theta \end{pmatrix} \quad R_y(\theta) = \begin{pmatrix} \cos\theta & 0 & -\sin\theta \\ 0 & 1 & 0 \\ \sin\theta & 0 & \cos\theta \end{pmatrix} \quad R_x(\theta) = \begin{pmatrix} \cos\theta & -\sin\theta & 0 \\ \sin\theta & \cos\theta & 0 \\ 0 & 0 & 1 \end{pmatrix}$$

Matrix representations of groups

All the symmetry operations in a point group can be represented by a set of transformation matrices Γ(g) with one matrix for each symmetry element of the group g. Each individual matrix is called a representative of the corresponding symmetry operation and the complete set of matrices is called a matrix representation of the group. The matrix representatives act on some chosen set of basis functions, and the actual matrices making up a given representation will depend on the basis that has been chosen. For more clarification we will give an example that shows how we can construct the matrix representation of a molecule.

Consider the matrix representation of the C_{3v} point group e.g for the molecule NH_3: First of all, we need to choose the basis (S_N,S_1,S_2,S_3) which comprise of the valance s orbitals on the nitrogen atom and three hydrogen atoms. Figure (A.1) shows the basis set and the symmetry operations of the C_{3v} point group.

The matrices that represent the symmetry operations performed on the chosen basis are:

$$\Gamma(E)\ (S_N, S_1, S_2, S_3) \begin{pmatrix} 1 & 0 & 0 & 0 \\ 0 & 1 & 0 & 0 \\ 0 & 0 & 1 & 0 \\ 0 & 0 & 0 & 1 \end{pmatrix} = (S_N, S_1, S_2, S_3)$$

$$\Gamma(C_3^+)\ (S_N, S_1, S_2, S_3) \begin{pmatrix} 1 & 0 & 0 & 0 \\ 0 & 0 & 0 & 1 \\ 0 & 1 & 0 & 0 \\ 0 & 0 & 1 & 0 \end{pmatrix} = (S_N, S_2, S_3, S_1)$$

$$\Gamma(C_3^-)\ (S_N, S_1, S_2, S_3) \begin{pmatrix} 1 & 0 & 0 & 0 \\ 0 & 0 & 1 & 0 \\ 0 & 0 & 0 & 1 \\ 0 & 1 & 0 & 0 \end{pmatrix} = (S_N, S_3, S_1, S_2)$$

$$\Gamma(\sigma_v)\ (S_N, S_1, S_2, S_3) \begin{pmatrix} 1 & 0 & 0 & 0 \\ 0 & 1 & 0 & 0 \\ 0 & 0 & 0 & 1 \\ 0 & 0 & 1 & 0 \end{pmatrix} = (S_N, S_1, S_3, S_2)$$

$$\Gamma(\sigma_{v'})\ (S_N, S_1, S_2, S_3) \begin{pmatrix} 1 & 0 & 0 & 0 \\ 0 & 0 & 1 & 0 \\ 0 & 1 & 0 & 0 \\ 0 & 0 & 0 & 1 \end{pmatrix} = (S_N, S_1, S_2, S_3)$$

$$\Gamma(\sigma_{v''})\ (S_N, S_1, S_2, S_3) \begin{pmatrix} 1 & 0 & 0 & 0 \\ 0 & 0 & 0 & 1 \\ 0 & 0 & 1 & 0 \\ 0 & 1 & 0 & 0 \end{pmatrix} (S_N, S_3, S_2, S_1)$$

Each matrix is representative and together they form the representation of the C_{3v} point group in the (S_N, S_1, S_2, S_3) basis.

Reducible and irreducible representations:

In the last example all the matrices took the same block diagonal form. A square matrix is said to be block diagonal when its diagonal elements contains square matrix and the off diagonal elements are zero.

$$\Gamma(E)\begin{pmatrix}1&0&0&0\\0&1&0&0\\0&0&1&0\\0&0&0&1\end{pmatrix}\quad \Gamma(C_3^+)\begin{pmatrix}1&0&0&0\\0&0&1&0\\0&0&0&1\\0&1&0&0\end{pmatrix}\quad \Gamma(C_3^-)\begin{pmatrix}1&0&0&0\\0&0&0&1\\0&1&0&0\\0&0&1&0\end{pmatrix}$$

$$\Gamma(\sigma_v)\begin{pmatrix}1&0&0&0\\0&1&0&0\\0&0&0&1\\0&0&1&0\end{pmatrix}\quad \Gamma(\sigma_v^{\nearrow})\begin{pmatrix}1&0&0&0\\0&0&1&0\\0&1&0&0\\0&0&0&1\end{pmatrix}\quad \Gamma(\sigma_v^{\searrow})\begin{pmatrix}1&0&0&0\\0&0&0&1\\0&0&1&0\\0&1&0&0\end{pmatrix}$$

Each matrix from these six matrices may be reduced to two matrices with different dimensions. The first matrix forms a one-dimensional representation $\Gamma^1(g)$ with (S_N) and the second one forms a three-dimensional representation $\Gamma^3(g)$ with the basis (S_1, S_2, S_3). Separation of the original representation into representations of lower dimensionality is called reduction of the representation.

To reduce the representation to a lower dimension, its representatives must all have the same block diagonal form. The three dimensional representation $\Gamma^3(g)$ is not in the block diagonal form, therefore the representation is not reducible and so is called an irreducible representation.

The irreducible representations of a point group are labeled according to their symmetry species as follows:

1- 1 dimensional representations are labeled A if they are symmetric (character +1) or$B$ if they are antisymmetric (character –1) under rotation about the principal axis.

2- 2 dimensional representations are labeled E

3- 3 dimensional representations are labelled T.

4- In groups containing a centre of inversion, g (garade, symmetric) and u (ungarade, antisymmetric) labels denote the character of the irreducible representation under inversion (+1 for g, -1 for u)

5- In groups with a horizontal mirror plane but no centre of inversion, the irreducible representation are given prime and double prime labels to denote whether they are symmetric (character +1) or antisymmetric (character –1) under reflection in the plane.

6- If further distinction between irreducible representation is required, subscripts 1 and 2 are used to denote the character with respect to a C_2 rotation perpendicular to the principal axis, or with respect to a vertical reflection if there are no C_2 rotations [117, 118, 119].

Bibliography

[1] T. H. Maiman. Stimulated optical in radiation in ruby. *Nature*, 187:493, 1960.

[2] I. S. Ruddock and D. J. Bradley. Bandwidth-limited subpicoseconds pulse generation in mode-lock cw dye laser. *Applied Physics Letters*, 29:296, 1976.

[3] U. Morgner, F .X. Kartner, S. H. Cho, Y. Chen, H. A. Haus, J. G. Fujimoto, E. P. Ippen, V. Scheuer, G. Angelow, and T. Tschudi. Sub-two-cycle pulses from a kerr-lens mode-locked Ti:sapphire laser. *Optic letter.*, 24:411, 1999.

[4] J. Hernandez-Rueda, S A. Avoia, W. Gawelda, J. Solis, B. Mansart, D. Boschetto, and J. Siegel. Coherent optical phonons in different phases of $\mathrm{Ge_2Sb_2Te_5}$ upon strong laser excitation. *Applied. Physics. Letters.*, 98:251906, 2011.

[5] S. M. Wiggins, J. Solis, and C. N. Afonso. Influence of pulse duration on the amorphization of GeSb thin films under ultrashort laser pulses. *Applied Physics Letters*, 84:4445, 2004.

[6] R. Loudon. The Raman effect in crystals. *Advanced in Physics*, 13:423, 1964.

[7] R. Merlin. Generation coherent THz phonons with light pulses. *Solid State Communications*, 102:207, 1997.

[8] P. Yu and M. Cardona. *Fundamental of semiconductors*. Springer-Verlag Berlin Heidelberg, 2010.

[9] G. P Srivastava. *The Physics of Phonons*. Taylor and Francis group, New york, 1990.

[10] C. Kittel. *Introduction to Solid State Physics*. John Wiley and Sons, 2005.

[11] G. Burns. *Solid State Physics*. Academic Press, Inc., 1985.

[12] A. Shalini, Y. Liu, U. A. S Al-Jarah, G.P. Srivastava, C.D. Wright, F. Katmis, W. Braun, and R. J. Hicken. Observation of T_2-like coherent optical phonons in epitaxial $Ge_2Sb_2Te_5/GaSb\,(001)$ films. *Scientific Reports*, 3:2965, 2013.

[13] G.F. Koster. *Space groups and their representations in solid state physics*. Academic, New York, 1957.

[14] J. C. Decius and R. M. Hexter. *Molecular vibrations in crystals*. McGraw-Hill, New York, 1977.

[15] D. S. Schonland. *Molecular Symmetry*. D. Van Nostrand Company, INC.,London, 1965.

[16] M. A. Omar. *Elementary Solid State Physics: Principles and Applications*. Addison-Wesley Publishing Company, Inc., 1975.

[17] J. S. Blakemore. *Solid state physics*. Cambridge University Press, 1985.

[18] L. Lou. *Introduction to phonons and electrons*. World scientific publishing Co. Pte. Ltd, 2003.

[19] W. G. Nilsen. Raman spectrum of ZnS. *Physical Review*, 182:838, 1969.

[20] M. S. Dresselhaus, G. Dresselhaus, and A. Jorio. *Group theory: application to the physics of condensed matter*. Springer-Verlag Berlin Heidelberg, 2008.

[21] G.P. Srivastava un puplished.

[22] H. Bilz and W. Kress. *Phonon dispersion relation in insulators*. Springer-Verlag Berlin Heidelberg, 1979.

[23] G. Ravnio, L. Almqvist, and R. Stedman. Phonon dispersion relation in NaCl. *Physical Review*, 178:1496, 1969.

[24] N. W. Ashcroft and N. D. Mermin. *Solid state physics*. Saunders, Philadelphia, 1976.

[25] R.H Lydden, R. G Sachs, and E Teller. On the polar vibrations of alkali halides. *Physical Review*, 59:673, 1941.

[26] T. Garl. *Ultrafast dynamics of coherent optical phonons in Bismuth*. PhD thesis, ENSTA - Ecole Polytechniqu, 2008.

[27] J. X. Cheng and X. S. Xie. *Coherent Raman scattering Microscopy*. Taylor and Francis group, 2013.

[28] F. El-Diasty. Coherent anti-stokes Raman scattering: spectroscopy and microscopy. *Vibrational Spectroscopy*, 55:1, 2011.

[29] P. Kukura, D. McCamant, and R. Mathies. Femtosecond stimulated Ramam spectroscopy. *Annual review of physical chemistry*, 58:461, 2007.

[30] D. A. Long. *The Raman effect*. John Wiley and Sons, Ltd, England, 2002.

[31] R. Loudon. Theory of stimulated raman scattering from lattice vibrations. *Proceding of the Physical Society*, 82:393, 1963.

[32] M. Balkanski. *Light scattering in solid*. Flammarion, Paris, 1971.

[33] C. Hamaguchi. *Basic semiconductor physics*. Springer-Verlag Berlin Heidelberg, 2001.

[34] T. C. Damen, S. P. S. Porto, and B. Tell. Raman effect in zinc oxide. *Physical Review*, 142:570, 1966.

[35] G. Martinez. *Optical properties of semiconductors*. Springer Science + Business Media Dordrecht, 1993.

[36] I. Zardo, S. Conesa-Boj, F. Peiro, J. R. Morante, J. Arbiol, E. Uccelli, G. Abstreiter, and A. Fontcuberta i Morral. Raman spectroscopy of wurtzite and zinc-blende GaAs nanowires: Polarization dependence, selection rules, and strain effects. *Physical Review B*, 80:245324, Dec 2009.

[37] J. Combe. *Phonon dispersion in zinc blend semiconductors*. PhD thesis, Simon France University, 1971.

[38] P. S. Pizani and R. G. Jasinevicius. The effect of high non-hydrostatic pressure on III-V semeiconductors: zinc blende to wurtzite structural phase transition and multiphase generation. *Journal of physics: conference series*, 500:182032, 2014.

[39] F. Bechstedt. *Principles of surface physics*. Springer-Verlag Berlin Heidelberg, 2003.

[40] V. Heine. *Group theory in quantum mechanics*. Pergamon Press, England, 1960.

[41] M.I Tinkham. *Group theory and quantum mechanics*. McGraw-Hill, New York, 1964.

[42] G. Herzberg. *Molecular spectra and molecular spectrum*. D. Van Nostrand Company, Inc, 1966.

[43] T. Dekorsy, G. C. Cho, and H. Kurz. Coherent phonons in condensed media. *Light Scattering in Solid*, 8:169, 2000.

[44] H. Goldstein, C. Poole, and J. Safko. *Classical Mechanics*. Addison-Wesley, Francisco, 2002.

[45] R. D. Gregory. *Classical mechanics*. Cambridge University Press, 2006.

[46] L. Dhar, J. A. Rogers., and K. A. Nelson. Time-resolved vibrational and spectroscopy in the impulsive limit. *Chemical Reviews.*, 94:157, 1994.

[47] G. A. Garrett, T. F. Albrecht, J. F. Whitaker, and R. Merlin. Coherent THz phonons driven by light pluses and the Sb problem: What is the mechanism? *Physical Review letters*, 77:3661, 1996.

[48] Y. X. Yan, J. Edward B. Gamble, and K.A Nelson. Impulsive stimulated scattering: general importance in femtosecond laser pulse interactions with matter and spectroscopic applicaions. *The Journal of Chemical Physics*, 83:5391, 1985.

[49] T. K. Cheng, J. Vidal, H. J. Zeiger, G. Dresselhaus, M. S. Dresselhaus, and E. P. Ippen. Mechanism for displacive excitation of coherent phsnons in Sb, Bi, Te, and $\mathrm{Ti_2O_3}$. *Applied Physics Letters*, 59:1923, 1991.

[50] M. Bargheer, N. Zhavoronkov, Y. Gritsai, J. C. Woo, D. S. Kim, M. Woerner, and T. Elsaesser. Coherent atomic motions in a nanostructure studied by femtosecond x-ray diffraction. *Science*, 306:1771, 2004.

[51] H. J. Zeiger, J. Vidalm, T. K. Cheng, E. P. Ippen, G. Dresselhaus, and M. S. Dresselhaus. Theory for displacive excitation of coherent phonons. *Physical Review B*, 45:768, 1992.

[52] T. E. Stevens, J. Kuhl, and R. Merlin. Coherent phonon generation and the two stimulated Raman tensors. *Physical Review B*, 65:144304, 2002.

[53] T. Pfeifer, T. Dekorsy, and H. Kurz. Generation mechanism for coherent LO phonons in surface-space-charge fields of III-V-compounds. *Applied physics A*, 55:482, 1992.

[54] S. Lou. *Ultrafast spectroscopy of semiconducting and multiferroic materials*. PhD thesis, The State University of New Jersey, 2007.

[55] X. C. Zhang, B. B. Hu, J. T. Darrow, and D. H. Auston. Generation of femtosecond electromagnetic pulses from semeiconductor surface. *Applied Physics Letters*, 56:1011, 1990.

[56] L. Min and R. J. Dwayne Miller. Subpicosecond reflective electro-optic sampling of electron-hole vertical transport in surface-space-charge fields. *Applied Physics Letters.*, 56:524, 1990.

[57] G. C. Cho, W. Kutt, and H. Kurz. Subpicosecond time-resolved coherent-phonon oscillations. *Physical Review Letters*, 65:764, 1990.

[58] L.W. Qu, X.S. Miao, J.J. Sheng, Z. Li, J.J. Sun, P. An, J. Huang, D. Yang, and C. Liu. Set/reset properties dependence of phase-change memory cell on thickness of phase-change layer. *Solid-State Electronics*, 56:191, 2011.

[59] S. R. Ovshinsky. Symmetrical current controlling device. *U.S. Patent*, 271:591, 1966.

[60] S. R. Ovshinsky. Reversible electric switching phenomena in disordered structures. *Physical Review Letters*, 22:1450, 1968.

[61] J. Feinleib, J. DeNeufvil, S. C. Moss, and S. R. Ovshinsky. Rapid reversible light-induced crystallization of amorphous semiconductors. *Applied Physics Letters*, 18:245, 1971.

[62] R. G. Neale, D. L. Nelson, and G. E. Moore. Nostructure and reprogrammable, the read mostly memory is here. *Electronics*, 30:56, 1970.

[63] N. Yamada, E. Ohno, N. Akahira, K. Nishiuchi, K. Nagata, and M. Tako. High speed overwritable phase change optical disc material. *Japanese Journal of Applied Physics*, 26:61, 1987.

[64] S. Raoux. Phase change materials. *Annual Review of Materials Research*, 39:25, 2009.

[65] V.Von. *Combinatorial material synthesis applied to Ge-Sb-Te based phase change materials*. PhD thesis, Rheinisch-Westfalischen Technischen Hochschule Aachen, 2003.

[66] D. Lencer, M. Salinga, and M. Wuttig. Design rules for phase-chang materials in data storage applications. *Advanced Materials*, 23:2030, 2011.

[67] M. Wuttig and C. Steimer. Phase change materials: From material science to novel storage devices. *Applied Physics A*, 87:411, 2007.

[68] A.V. Kolobov, P. Fons, and J. Tominaga. Phase-change optical recording: Past, present, future. *Thin Solid Films*, 515:7534, 2007.

[69] A. Kolobov, P. Fons, A. Frenkel, A. Ankudinov, J. Tominaga, and T. Uruga. Understanding the phase-change mechanism of rewritable optical media. *Nature Materials*, 3:703, 2004.

[70] T. Nonka, G. Ohbayashi, Y. Toriumi, Y. Mori, and H. Hashimoto. Crystal structure of GeTe and $\mathrm{Ge_2Sb_2Te_5}$ meta-stable phase. *Thin Solid Films*, 370:258, 2000.

[71] Z. Sun, J. Zhou, and R. Ahuja. Structure of phase change materials for data storage. *Physical Review Letters*, 96:055507, 2006.

[72] N. Yamada and T. Matsunaga. Structure of laser-crystallized $\mathrm{Ge_2Sb_{2+x}Te_5}$ sputtered thin films for use in optical memory. *Journal of Applied Physics*, 88:7020, 2000.

[73] M. Wuttig and N. Yamada. Phase change materials for rewritable data storage. *Nature Materials*, 6:824, 2007.

[74] M. Upadhyay, S. Murugavel, M. Anbarasu, and T. R. Ravindran. Structural study on amorphous and crystalline state of phase change material. *Journal of Applied Physics*, 110:083711, 2011.

[75] S. Caravati, M. Bernasconi, T.D. Kuhne, M. Krack, and M. Parrinello. Coexistence of tetrahedral- and octahedral-like sites in aamorphous phase change material. *Applied Physics Letters*, 91:71906, 2007.

[76] B. Huang and J. Robertson. Bonding origin of optical contrast in phase-change memory materials. *Physical Review B*, 81:081204, 2010.

[77] M. Forst, T. Dekorsy, C. Trappe, M. Laurenzis, H. Kurz, and B. Bechevet. Phase change in $Ge_2Sb_2Te_5$ films investigated by coherent phonon spectroscopy. *Applied Physics Letters*, 77:1964, 2000.

[78] Y. Li, V. Stoica, L. Endicott, G. Wang, and C. Uher et al. Coherent optical phonon spectroscopy studies of femtosecond-laser modified Sb_2Te_3 films. *Applied Physics Letters*, 97:171908, 2010.

[79] K. Makino, J. Tominaga, A. Kolobov, P. Fons, and M. Hase. Polarization dependent optical control of atomic arrangement in multilayer Ge-Sb-Te phase change materials. *Applied Physcs Letter.*, 101:232101, 2012.

[80] M. Hase, Y. Miyamoto, and J.Tominaga. Ultrafast dephasing of coherent optical phonons in atomically controlled $GeTe/Sb_2Te_3$ superlattice. *Physical Review B*, 79:174112, 2009.

[81] G. C. Sosso, S. Caravati, R. Mazzarello, and M. Bernasconi. Raman spectra of cubic and amorphous $Ge_2Sb_2Te_5$ from first principles. *Physical Review B*, 83, 2011.

[82] N. Yamada, R. Kojima, M. Uno, T. Akiyama, H. Kitaura, K. Narumi, and K. Nishiuchi. Phase change material for use in rewritable dual-layer optical disk. *Proc. SPIE*, 4342:55, 2002.

[83] X.S. Miao, T.C. Chong, Y. M Huang, K. G. Lim, and P. K. Tan. Dependence of optical constants on film thickness of phase change media. *Japanese Journal of Applied Physics*, 38:1638, 1999.

[84] B. S. Lee, J. R. Abelson, S. G. Bishop, D. H. Kang, B. K. Cheong, and K. B. Kim. Investigation of the optical and electronic properties of $Ge_2Sb_2Te_5$ phase change material in its amorphous, cubic, and hexagonal phases. *Journal of Applied Physics*, 97:093509, 2005.

[85] S. Raoux and M. Wuttig. *Phase change materials: science and applications*. Springer Science + Business Media, New York, 2009.

[86] T. Tsafack, E. Piccinini, B. Lee, E. pop, and M. Rudan. Electronic, optical and thermal properities of the hexagonal and rocksalt-like $Ge_2Sb_2Te_5$ chalcogenide from first-principle calculations. *Journal of Applied Physics*, 110:063716, 2011.

[87] A. V. Kolobov, P. Fons, J. Tominaga, A. I. Frenkel, A. L. Ankudinov, S. N. Yannopoulos, K. S. Andrikopoulos, and T. Uruga. Why phase-change media are fast and stable: A new approach to an old problem. *Japanese Journal of Applied Physics*, 44:3345, 2005.

[88] R. E. Simpson, P. FP. Fons . V. Kolobov, T. Fukaya, M. Krbal, T. Yagi, and J. Tominaga. Interfacial phase-change memory. *Nature Nanotechnology*, 6:501, 2011.

[89] L. Frank and S. Leno. *Introduction to Optics*. Prentice-Hall Inc., 1987.

[90] P. Franken, A. Hill, C. Peters, and G. Weinreich. Generation of optical harmonics. *Physical Review Letters*, 7:118, 1961.

[91] D. Kleinman. Nonlinear dielectric polarization in optical media. *Physical Review*, 126:1977, 1962.

[92] A. Shalini. *Ultrafast optical studies of Phonons and phase transition in* $Ge_2Sb_2Te_5$ *thin films*. PhD thesis, University of Exeter, 2013.

[93] U. Al-Jarah. *Modification and monitoring of magnetic properties with ultrafast laser pulses*. PhD thesis, University of Exeter, 2013.

[94] R. Wilks. Investigation of ultrafast demagnetization and cubic optical nonlinearity of Ni in the polar geometry. *Journal of Applied Physics*, 95:7441, 2004.

[95] R. Wilks and R. J. Hicken. Transient optical polarization response of aluminium at an interband transition. *Journal of Physics: Condens. Matter*, 16:4607, 2004.

[96] S. V. Popov, Y. P. Svirko, and N.I. Zheludev. Pump-probe reflective polarization-sensitive nonlinear optics. *Journal of the Optical Society of American*, 13:2729, 1996.

[97] F. D. Longa, J.T. Kohlhepp, W.J.M. de Jonge, and B. Koopmans. Influence of photon angular momentum on ultrafast demagnetization in nickel. *Physical Review B*, 75:224431, 2007.

[98] M. Born and E. Wolf. *Principles of Optics: electromagnetic theory of propagation, interference and diffraction of light*. Cambridge University Press, 1999.

[99] L. Shelford. *Ultrafast nonlinear optical studies of multilayered thin films and interfsces*. PhD thesis, University of Exeter, 2009.

[100] A. V. Kimel, F. Bentivegna, V. N. Gridnev, V. V. Pavlov, R. V. Pisarev, and T. Rasing. Room-temperature ultrafast carrier and spin dynamics in gaas probed by the photoinduced magneto-optical kerr effect. *Physical Review B*, 63(235201), 2001.

[101] R. Fuchs and K. L. Kliewer. Optical modes of vibration in an ionic crystal slab. *Physical Review*, 140:A2076, 1965.

[102] G. P Srivastava. Theory of semiconductor surface reconstruction. *Reports on Progress in Physics*, 66:561, 1997.

[103] L. Tianfeng, G. Lizhen, L. Wen, G. Lijun, Y. Tao, C. Yonghai, and W.Zhanguo. Raman study on zinc blende single InAs nanowire grown on Si (111) substrate. *Nanoscale Research Letters*, 8:27, 2013.

[104] L. Tianfeng, C. Yonghai, L. Wen, Z. Xiaolong, L. Shuai, H. Yongzheng, W. Lijun, Y. Tao, and W.Zhanguo. Effect of growth temperature on the morphology and phonon properities of InAs nanowires on Si substrates. *Nanoscale Research Letters*, 6:463, 2011.

[105] N. G. Hormann, I. Zardo, S. Hertenberger, S. Funk, S. Bolte, M. Doblinger, G. Koblmuller, and G. Abstreiter. Effect of stacking variations on the lattice dynamics of InAs nanowires. *Physical Reviews B*, 84:155301, 2011.

[106] A. Shalini, Y. Liu, F. Katmis, W. Braun, G.P. Srivastava, and R. J. Hicken. Coherent phonon modes of crystalline and amorphous $\mathrm{Ge_2Sb_2Te_5}$ thin films: A fingerprint of structure and bonding. *Journal of Applied Physics*, 117:025306, 2015.

[107] W. Hayes and R. Loudon. *Scattering of light by crystals*. Dover, 2004.

[108] Y. Liu, M. M. Aziz, A.Shalini, C. D. wright, and R. J. Hicken. Crystallization

of $Ge_2Sb_2Te_5$ films by amplified femtosecond optical pulses. *Journal of Applied Physics*, 112:123526, 2012.

[109] J. Siegel, W. Gawelda, D. Puerto, C. Dorronsoro, J. Solis, C. N. Afonso, J. C. G. de Sande, R. Bez, A. Pirovano, and C. Wiemer. Amorphization dynamic of $Ge_2Sb_2Te_5$ films upon nano- and femtosecond laser pulse irradiation. *Journal of Applied Physics*, 103:023516, 2008.

[110] R. L. Cotton and J. Siegel. Stimulated crystallization of melt-quenched $Ge_2Sb_2Te_5$ films employing femtosecond laser double pulses. *Journal of Applied Physics*, 112:123520, 2012.

[111] B. Liu, Z. Song, T. Zhang, S. Feng, and B. Chen. Raman spectra and xps studies of phase changes in $Ge_2Sb_2Te_5$ films. *Chinese Physics*, 13:1947, 2004.

[112] E. Cho, S. Yoon, H. R.Yoon, and W.Jo. Micro-raman scattering studies of Ge-Sb-Te bulk crystals and nanoparticles. *Journal of the Korean Physical Society*, 48:1616, 2006.

[113] P. Nemec, V.Nazabal, A. Moreac, J. Gutwirth, L. Benes, and M. Frumar. Amorphous and crystallized Ge-Sb-Te thin films deposited by pulsed laser: Local structure using raman scattering spectroscopy. *Materials Chemistry and Physics*, 136:935, 2012.

[114] W. Braun, R. Shayduk, T. Flissikowski, M. Ramsteiner, H. Grahn, H. Riechert, P. Fons, and A. Kolobov. Epitaxy of $Ge_2Sb_2Te_5$ phase-change memory alloys. *Applied Physics Letters*, 94:041902, 2009.

[115] J. Akola and R. Jones. Density functional study of amorphous, liquid and crystalline $Ge_2Sb_2Te_5$: homopolar bonds and/or ab alternation. *Journal of Physics: Condensed Matter*, 20:465103, 2008.

[116] K. Makino, J. Tominaga, and M. Hase. Ultrafast optical manipulation of atomic arrangement in chalcogenide alloy memory materials. *Opt. Express*, 19:1260, 2011.

[117] F. A. Cotton. *Chemical applications of group theory*. Wiley, India, 1990.

[118] C. E. Housecroft and A. G. Sharpe. *Inorganic chemistry*. Pearson Education Limited, 2005.

[119] T. Inui, Y. Tanabe, and Y. Onodera. *Group theory and its applications in physics*. Springer-Verlag Berlin Heidelberg, 1990.